Cleanroom in an SEM

Jeevanandam, G.

DOI
10.4233/uuid:a324902b-a157-4244-9cf3-1ca627ef641b

Publication date
2024

Document Version
Final published version

Citation (APA)
Jeevanandam, G. (2024). *Cleanroom in an SEM*. [Dissertation (TU Delft), Delft University of Technology]. https://doi.org/10.4233/uuid:a324902b-a157-4244-9cf3-1ca627ef641b

CLEANROOM IN AN SEM

CLEANROOM IN AN SEM

Dissertation

for the purpose of obtaining the degree of doctor
at Delft University of Technology
by the authority of the Rector Magnificus Prof.dr.ir. T.H.J.J. van der Hagen,
chair of the board of Doctorates
to be defended publicly on
Friday 22, March 2024 at 12:30 o'clock

by

Gaudhaman JEEVANANDAM

Master of Science in Advanced Optical Technologies
Friedrich-Alexander-Universität Erlangen-Nürnberg, Germany
born in Chingleput, India

This dissertation has been approved by the promotors.

promotor: Dr. C.W. Hagen
promotor: Em. Prof. dr. ir. P. Kruit

Composition of the doctoral committee:

Rector Magnificus,	chairperson
Dr. C.W. Hagen	Delft University of Technology, promotor
em. Prof. dr. ir. P. Kruit	Delft University of Technology, promotor

Independent members:

Dr. F. Nouvertné,	Raith, USA
Prof. dr. ing. A.J.H.M. Rijnders	University of Twente, Netherlands
Prof. dr. ir. J.R. van Ommen	Delft University of Technology
Prof. dr. ir. H.S.J. van der Zant	Delft University of Technology
Prof. dr. ir. P.M. Sarro	Delft University of Technology

The work in this dissertation was conducted at the department of Imaging Physics, Faculty of Applied Sciences, Delft University of Technology.

Printed by: Ridderprint, www.ridderprint.nl

Front & Back: Sketch illustration of the cleanroom process in an SEM.

ISBN 978-94-6384-541-0

An electronic version of this dissertation is available at
http://repository.tudelft.nl/.

CONTENTS

SUMMARY

The aim of this thesis, *Cleanroom in an SEM*, was to enhance an existing SEM to function as a multi-purpose tool by incorporating miniaturized versions of cleanroom tools used in microfabrication. Thereby, reducing the cost and time for rapid prototyping of proof of concept devices in a single tool.

Chapter 1 provides the introduction of this thesis, briefly explaining the idea behind the thesis. In chapter 2, a detailed discussion of various cleanroom processes, including their process parameters, and the reasoning behind integrating them into the SEM, is given. In this chapter, also the limitations involved in introducing materials or processes into the SEM are examined and the selection of the cleanroom processes suitable for integration in the SEM are explained in detail. Specifically, this chapter outlines the development of four tools within the SEM: a substrate heater, an in-situ thermal atomic layer deposition (ALD), a miniature plasma source for sputtering, and a miniature thermal evaporator. Furthermore, a proposed process flow for the in-SEM fabrication of a bow-tie antenna using the integrated tools is presented.

Chapter 3 focuses on the requirements, design, fabrication and demonstration of two substrate heaters, V1 (designed for 150 ^{o}C) and V2 (capable of heating up to 300 ^{o}C). V1 was developed for partially cleaning the substrate, to remove adsorbed water and for purification of FEBID structures. The design and fabrication of V1 were discussed in the first part of this chapter. V1 is capable of heating up to 150 ^{o}C and is designed to accommodate samples of size 1 x 1 cm^2. The temperature limit of V1 is determined by the choice of material (PEEK) used in its construction. The heater was designed to minimize temperature drift as we increase the temperature to 150 ^{o}C. We measured a ramp-up rate of 8.2 ^{o}C/min and a ramp-down rate of 16 ^{o}C/min. The second half of chapter 3 focuses on the design, fabrication, and demonstration of V2, which can reach a temperature of 300 ^{o}C. V2 is designed for in-situ thermal ALD and to accommodate samples of size 1 x 1 cm^2. And was also designed with relaxed requirement of minimizing thermal drift during temperature ramp-up. Glass was used in the construction of V2 instead of PEEK to achieve the higher temperature limit. We measured a ramp-up rate of 18.4 ^{o}C/min to heat the substrate to 300 ^{o}C from room temperature and a ramp-down rate of 25 ^{o}C/min to bring the substrate from 300 ^{o}C to 40 ^{o}C.

Chapter 4 of this thesis presents the development of an in-situ thermal atomic

layer deposition (ALD) process inside the SEM. We utilized the V1 substrate heater to reach a temperature of 241 ^{o}C for initial ALD experiments. The Pt precursor dosing and pump down time were chosen based on existing literature data and pump down experiments. The ALD layer was grown on Pt FEBID seed layers. With 17 cycles of ALD, an ALD growth of 0.7 nm was observed. Each ALD cycle took approximately 3 minutes in the system. The long ALD cycle time was primarily due to the extended purge time after precursor dosing, which was a result of the standard gas injection system (GIS) design. To address this issue, a new GIS needle was developed that positioned the valve closer to the needle tip, resulting in a purge time reduction of an order of magnitude. Using the new GIS needle, we demonstrated 25 ALD cycles on Pt FEBID seed layers with an improved ALD cycle time of 55 seconds. A further reduction in the ALD cycle is possible by replacing the manual valves by computer controlled valves.

Chapter 5 of this thesis presents the design, fabrication, and demonstration of a miniature plasma source used as a sputtering tool. An initial prototype was developed in a high vacuum system, such that we were able to operate the plasma source at SEM operating pressures (10^{-6} mbar). The Paschen curve and the current-voltage characteristic curve were measured for the plasma source using Ar as the gas source. We were able to successfully etch a 20 nm thick Au film with an etch diameter of 200 μm using the plasma source. EOD simulations were carried out to explain the focussing by the plasma source. Based on this initial prototype plasma source, we designed and fabricated a miniature plasma source for use in the SEM. A housing assembly was designed to house the plasma source and also a thermal evaporator in the SEM. Utilizing the miniature plasma source, we successfully demonstrated sputter etching of a 20 nm thick Au film with an etch diameter of 35 μm. In future, the gas source could be replaced by dry air, thereby enabling an oxygen plasma to clean substrates and to improve the quality of FEBID deposits.

In chapter 6 of this thesis, we focused on the design, fabrication, and demonstration of a miniature thermal evaporator inside the SEM. Initially, we developed a prototype in a high vacuum system using a Philips I-cathode source. Using this prototype thermal evaporator, we successfully deposited a thin film of Au with an area of 1 mm in diameter. Building on this initial prototype, we designed and fabricated a miniature thermal evaporator for the SEM. However, during testing, the supply leads of the Philips I-cathode supply were disconnected due to stress applied during the mounting process. To avoid this issue, a stress relief structure should be added to the existing evaporator to make it functional. Unfortunately, time constraints prevented us from modifying the evaporator assembly.

In conclusion, we believe that the integration of the substrate heater, in-situ thermal ALD, sputtering tool, and evaporator inside the SEM will enable the

faster realization of proof-of-concept devices with significant reductions in time and cost. Such a versatile tool will serve researchers in academia and research institutes in rapidly fabricating prototype devices in a single tool, eliminating the need for a cleanroom. In this work, we have developed prototype add-on tools, but unfortunately we could not extensively test nor use in combination to realize an actual in-situ device. This remains to be done, and when successful, the concept of *Cleanroom in an SEM* is ready for commericialisation. The *Cleanroom in an SEM* tool will be invaluable for universities and research institutes to carry out research.

SAMENVATTING

Het doel van dit proefschrift, getiteld *Cleanroom in een SEM*, was om een bestaande SEM zodanig te verbeteren dat deze functioneert als een multifunctioneel instrument, door het integreren van geminiaturiseerde versies van cleanroomgereedschappen die gebruikt worden bij microfabricage. Dit leidt tot een tijd- en kostenbesparing bij het maken van prototypes van 'proof-of-concept' componenten in één enkel instrument.

Hoofdstuk 1 biedt de inleiding van dit proefschrift en geeft kort uitleg over het idee achter het proefschrift. In hoofdstuk 2 wordt een gedetailleerd overzicht gegeven van verschillende cleanroomprocessen, inclusief hun procesparameters, en de argumentatie achter hun integratie in de SEM. In dit hoofdstuk worden ook de beperkingen die gepaard gaan met het introduceren van materialen of processen in de SEM onderzocht en wordt de selectie van de cleanroomprocessen, geschikt voor integratie in de SEM, in detail uitgelegd. Specifiek schetst dit hoofdstuk de ontwikkeling van vier processen binnen de SEM: substraatverwarming, in-situ thermische atoomlaagdepositie (ALD), sputteren met een miniatuurplasmabron en depositie met een miniatuur thermische verdamper. Bovendien wordt er een proces voorgesteld voor de fabricage van een 'bow-tie' antenne in de SEM met behulp van de geïntegreerde gereedschappen.

Hoofdstuk 3 richt zich op de eisen aan, het ontwerp, de fabricage en de demonstratie van twee substraatverwarmers, V1 (ontworpen voor 150 ^{o}C) en V2 (in staat om op te warmen tot 300 ^{o}C). V1 is ontwikkeld voor het reinigen van het substraat, het verwijderen van geadsorbeerd water en voor zuivering van FEBID-structuren. Het ontwerp en de fabricage van V1 worden besproken in het eerste deel van dit hoofdstuk. V1 kan opwarmen tot 150 ^{o}C en is ontworpen om monsters van 1 x 1 cm^2 formaat te kunnen herbergen. De temperatuurlimiet van V1 wordt bepaald door de keuze van het materiaal (PEEK) dat wordt gebruikt in de constructie ervan. De verwarmer is ontworpen om de thermische beweging te minimaliseren wanneer de temperatuur wordt verhoogd tot 150 ^{o}C. We hebben een opwarmingssnelheid gemeten van 8.2 ^{o}C /min en een afkoelsnelheid van 16 ^{o}C /min. Het tweede deel van hoofdstuk 3 richt zich op het ontwerp, de fabricage en de demonstratie van V2, die een temperatuur van 300 ^{o}C kan bereiken. V2 is ontworpen voor in-situ thermische ALD en is bedoeld voor monsters van 1 x 1 cm^2 formaat. Er is ook een minder strikte eis gesteld aan het minimaliseren van de thermische beweging tijdens het opwarmen. In de constructie van V2 is glas

gebruikt in plaats van PEEK om de hogere temperatuurlimiet te bereiken. We hebben een opwarmingssnelheid gemeten van 18.4 ^{o}C /min om het substraat op te warmen van kamertemperatuur tot 300 ^{o}C, en een afkoelsnelheid van 25 ^{o}C /min om het substraat van 300 ^{o}C naar 40 ^{o}C te brengen.

In hoofdstuk 4 van dit proefschrift wordt de ontwikkeling van een in-situ thermisch atomaire-laagdepositie (ALD) proces binnen de SEM gepresenteerd. We hebben gebruik gemaakt van de V1 substraatverwarmer om een temperatuur van 241 ^{o}C te bereiken voor de eerste ALD-experimenten. De dosering van de Pt precursor en de afpomptijd zijn gekozen op basis van bestaande literatuurgegevens en afpompexperimenten. De ALD-laag werd gegroeid op Pt FEBID zaailagen. Met 17 cycli van ALD werd een ALD-groei van 0.7 nm waargenomen. Elke ALD-cyclus in het systeem nam ongeveer 3 minuten tijd in beslag. De lange ALD-cyclusduur was voornamelijk te wijten aan de lange schoonmaaktijd na de dosering van de precursor, die het gevolg was van het standaard gasinjectiesysteem (GIS)-ontwerp. Om dit probleem aan te pakken, is een nieuwe GIS-naald ontwikkeld waarin het ventiel dichter bij de punt van de naald geplaatst is, resulterend in een orde van grootte kortere schoonmaaktijd. Met behulp van de nieuwe GIS-naald hebben we 25 ALD-cycli gedemonstreerd op Pt FEBID zaailagen met een veel kortere ALD-cyclusduur van 55 seconden. Een verdere verkorting van de ALD-cyclusduur is mogelijk door de handbediende kleppen te vervangen door kleppen die door een computer worden aangestuurd.

Hoofdstuk 5 van dit proefschrift behandelt het ontwerp, de fabricage en de demonstratie van een miniatuur plasma-bron die wordt gebruikt voor sputtering. Een eerste prototype werd ontwikkeld voor een hoogvacuümsysteem, zodat we de plasma-bron konden bedienen bij SEM-werkdrukken (10^{-6} mbar). De Paschen-kromme en de stroom-spanningskarakteristiek werden gemeten voor de plasma-bron met Ar als gasbron. We slaagden erin om met de plasma-bron succesvol een 20 nm dikke Au-film te etsen over een klein oppervlak met een diameter van 200 μm. EOD-simulaties werden uitgevoerd om de focussering door de plasma-bron te verklaren. Op basis van dit prototype hebben we een miniatuur plasma-bron ontworpen en vervaardigd voor gebruik in de SEM. Een behuizing is ontworpen om zowel de plasma-bron als een thermische verdamper onder te brengen in de SEM. Met deze miniatuur plasma-bron hebben we met succes het sputteretsen gedemonstreerd van een 20 nm dikke Au-film over een etsdiameter van 35 μm. In de toekomst kan de gasbron worden vervangen door droge lucht, waardoor een zuurstofplasma mogelijk wordt om substraten schoon te maken of om de kwaliteit van FEBID-deposities te verbeteren.

In hoofdstuk 6 van dit proefschrift lag de focus op het ontwerp, de fabricage en de demonstratie van een miniatuur thermische verdamper in de SEM. In eerste instantie ontwikkelden we een prototype voor een hoogvacuümsysteem ge-

baseerd op een Philips I-kathode bron. Met het prototype van deze thermische verdamper hebben we succesvol een dunne goud film afgezet over een diameter van 1 mm. Voortbouwend op dit prototype hebben we een miniatuur thermische verdamper ontworpen en vervaardigd voor gebruik in de SEM. Tijdens de tests, echter, hebben de toevoerleidingen van de Philips I-kathode bron het begeven als gevolg van mechanische spanning aangebracht tijdens het montageproces. Om dit probleem te voorkomen, moeten er trekontlastingingen worden aangebracht aan de bestaande verdamper om deze functioneel te maken. Helaas belemmerden tijdsbeperkingen ons bij het aanpassen van de verdamper.

Concluderend, zijn wij van mening dat de integratie van de substraatverwarmer, in-situ thermische ALD, sputtergereedschap en verdamper in de SEM zal leiden tot een snellere realisatie van 'proof-of-concept' componenten met aanzienlijke tijds- en kostenbesparingen. Zo'n veelzijdig gereedschap zal onderzoekers in academische en onderzoeksinstellingen van dienst zijn bij het snel fabriceren van prototype componenten, met behulp van slechts één enkel gereedschap, waarbij de behoefte aan een cleanroom wordt geëlimineerd. In dit werk hebben we prototype 'add-on' gereedschappen ontwikkeld, maar helaas konden we deze niet uitgebreid testen of in combinatie gebruiken om daadwerkelijk insitu een component te realiseren. Dit moet nog worden gedaan en wanneer dit succesvol is, is het concept van *Cleanroom in een SEM* klaar voor commercialisering. Het *Cleanroom in een SEM* gereedschap zal van onschatbare waarde zijn bij het onderzoek aan universiteiten en onderzoeksinstellingen.

1

INTRODUCTION

1.1. INTRODUCTION

Gordon Moore's observation of the doubling, roughly every two years of the number of transistors in an integrated circuit (IC) in 1965, drove the downscaling of the transistor [1]. To this day, Moore's law has continued this scaling trend of IC's. This has led to an increase in the size of tools used in the manufacturing process. The research and development costs have also steadily increased with it. A cleanroom is a necessity to manufacture IC chips. It maintains the environment of the tools in a clean environment through the use of air filters, to avoid defects due to particles and any contamination of the wafers between different processes in manufacturing.

Let's say we walk into a cleanroom, for example the Kavli Nanolab at TU Delft. We come across different tools required for micro- or nanofabrication. Some of the tools we come across are a wet bench (cleaning, spin coater), deposition tools (evaporation, sputter deposition and atomic layer deposition), etching tools (sputter etching, reactive ion etching, plasma etching), lithography tools (electron beam lithography, photolithography, laser writer) and inspection tools (atomic force microscopy, optical microscope, profilometer, scanning electron microscope, energy dispersive X-ray analysis). A cleanroom is a necessity for nanofabrication to prevent the substrate to be exposed to ambient air in between processes. Ambient air has a lot of particles, these particles can deposit on the substrate. Contaminants deposited on the substrate in between the processes will affect the quality (eg.,particles in the dielectric layer) of the fabricated device. The substrate is generally a slice of crystalline silicon (c-Si), a wafer. The diameter of a wafer can range from 25.4 mm to 300 mm. 300 mm c-Si wafers are generally used in high volume manufacturing of integrated circuits. However,

many researchers in academia do not need full wafers with devices, but often only a few to demonstrate proof of concept. The total device area is probably a few μm^2 only, this is shown in figure 1.1a for a single electron transistor and figure 1.1b for an array of bow-tie antenna's. The substrates that are mounted in scientific measurement setups are of the order of 1 cm^2 in size.

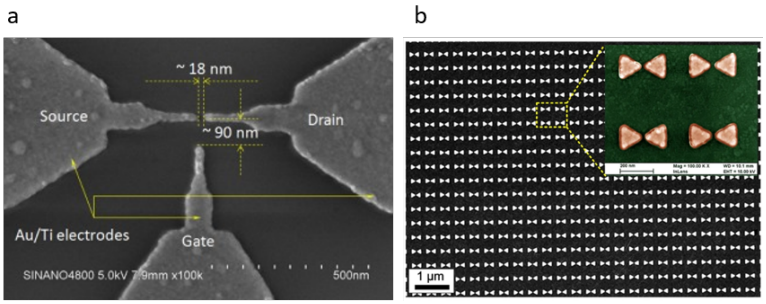

Figure 1.1: a) Secondary electron image of a Single electron transistor [2]. Reprinted from [2] Copyright ©(2016) with permission from Elsevier. b) Secondary electron image of a bow-tie antenna [3]. Reprinted from [3] Copyright ©(2015) Springer Nature.

In this thesis, we propose the idea of having a master tool, which contains miniaturized versions of the different cleanroom tools used in the fabrication process. We chose the SEM as the master tool, hence the thesis is titled *Cleanroom in an SEM*. This thesis provides a solution to reduce the cost and time for the fast prototyping of proof of concept devices in a single tool instead of in a standard cleanroom. A cleanroom requires a high investment, expensive high efficiency particulate air (HEPA) filters, and expensive instruments for each manufacturing processes. The goal of this thesis is to develop the instrumentation for a selection of cleanroom techniques for application in an SEM, and present proof of concepts for these miniaturized instruments.

The thesis is structured as follows.

In chapter 2, the different cleanroom techniques are explained, and following that a scanning electron microscope (SEM) is explained detailing the capabilities of the tool. Next, we discuss the restrictions of integrating different tools in an SEM. Followed by that, we list the key parameters for integrating add-on tools in an SEM and the reason behind choosing an SEM for the integration. Finally, we present the selection of the tools which we will integrate into an SEM, the selection is based on the ability of the tool to be integrated into an SEM and fabrication of an actual device inside an SEM.

In chapter 3, we describe the requirements for the implementation of a miniature substrate heater in an SEM. Next, the design, fabrication and assembly of

the miniature substrate heater is explained in detail followed by the performance test of the substrate heater. We also develop a version 2 of the substrate heater for implementing an atomic layer deposition tool in an SEM.

In chapter 4, the requirements for the implementation of area selective thermal atomic layer deposition (ALD) in an SEM is described. Next, we discuss the design, fabrication and assembly of the ALD setup in SEM. Here, we improve the existing gas injection system (GIS) available in an SEM, and modify it to be usable for area selective ALD. Finally, we demonstrate the working of an area selective ALD tool inside an SEM.

In chapter 5, the requirements for the implementation of an in-situ sputter etching tool is described. The design, fabrication and assembly of such a sputter source in a high vacuum setup is detailed. Based on the performance tests in the vacuum setup, we design, fabricate and assemble an in-situ sputter etch tool in an SEM. And we demonstrate a working sputter etch tool in an SEM.

In chapter 6, the requirements for the implementation of a miniature evaporator is described. Similar to the previous chapter, we discuss the initial design, fabrication and assembly in a high vacuum setup. Based on the results from the high vacuum setup, we design, fabricate and assemble a miniature evaporator inside an SEM.

Finally in chapter 7, we present the conclusions of the thesis.

REFERENCES

[1] G. Moore, *Cramming More Components onto Integrated Circuits* , Electronics Magazine **38** (1965).

[2] F. Wang, J. Fang, S. Chang, S. Qin, X. Zhang, and H. Xu, *Room temperature coulomb blockade mediated field emission via self-assembled gold nanoparticles,* Physics Letters A **381**, 476 (2017).

[3] Q. Wang, L. Liu, Y. Wang, P. Liu, H. Jiang, Z. Xu, Z. Ma, S. Oren, E. K. C. Chow, M. Lu, and L. Dong, *Tunable Optical Nanoantennas Incorporating Bowtie Nanoantenna Arrays with Stimuli-Responsive Polymer,* Scientific Reports **5** (2016).

2

MOTIVATION

2.1. INTRODUCTION

In this chapter, we will discuss the commonly used nanofabrication techniques used to fabricate devices. We will specifically look at the requirements for each of these techniques. This chapter answers the following questions. What are the requirements for each tool? Why we chose to integrate the tools in an SEM? What are the restrictions in an SEM? Why we chose specific tools for integration in the SEM?

2.2. CLEANROOM TECHNIQUES

A cleanroom is a controlled environment with a low amount of particles achieved through the use of air filters. Let's say we walk into a cleanroom, for example the Kavli Nanolab at TU Delft. We come across different tools required for micro- or nanofabrication. Some of the tools we come across are a wet bench (cleaning, spin coater), deposition tools (evaporation, sputter deposition, atomic layer deposition), etching tools (sputter etching, reactive ion etching, plasma etching), lithography tools (electron beam lithography, photolithography, laser writer) and inspection tools(atomic force microscopy, optical microscope, profilometer, scanning electron microscope, energy dispersive X-ray analysis). Why are the tools present inside a cleanroom not in ambient air? Why do we need an expensive cleanroom to fabricate devices? A cleanroom is a necessity for nanofabrication because in between different processes, the substrate is exposed to ambient air. Ambient air has a lot of particles, these particles can deposit on the substrate. Contaminants deposited on the substrate in between the processes will affect the quality (eg.,particles in the dielectric layer) of the fabricated

device. This is the reason why a cleanroom is needed to fabricate devices. The substrate is generally a slice of crystalline silicon (c-Si), a wafer. The diameter of a wafer can range from 25.4 mm to 300 mm. 300 mm c-Si wafer is generally used in high volume manufacturing of integrated circuits. For research purposes, we generally use c-Si wafers in the dimensions of a few mm (eg, 1x1 cm) but the area of interest (device area)is often much smaller.

2.2.1. FABRICATION PROCESSES

Now we will investigate the different fabrication techniques typically available in a cleanroom. We will look at this from the perspective of how they work, what they are used for and at what conditions (eg. temperature, pressure, gases, etc.) they work.

CLEANING

It is the first step in any nanofabrication process. Cleaning is done to remove contaminants from the surface of the wafer. The contaminants can either be particles or organic contaminants. This process can be done in two ways: wet cleaning and dry cleaning. One of the common wet cleaning methods used to clean a silicon wafer is RCA (Radio Corporation of America) cleaning. It is used to remove native oxide, particles, organic and ionic contaminants [1]. The first step involves immersing the wafer in a solution of ammonium hydroxide (NH_4OH), hydrogen peroxide (H_2O_2) and deionized water (DI H_2O) with a ratio of 1:1:5 at 70^oC to remove organic and particle contamination. The second step involves immersing the wafer in a solution of hydrochloric acid (HCl), H_2O_2 and DI H_2O with a ratio of 1:1:6 to remove metal contaminants. The wafer is dipped in a hydrofluoric acid (HF) for a short duration after each step to remove the oxide layer formed in the step.

Solvent clean is an another type of wet cleaning method. It is used to remove organic contaminants and oil from the surface of the wafer. It is a two-step process, first the wafer is immersed in an acetone solution and kept in an ultrasonic bath for 15 minutes. Next, the wafer is immersed in a solution of isopropyl alcohol (IPA) and kept in an ultrasonic bath for 15 minutes. This is followed by blow drying the wafer using N_2.

Dry cleaning is achieved by the following methods. UV radiation with oxygen or ozone gas to oxidize and volatilize the adsorbed carbon contaminants from the surface [2] [3]. Ar sputtering has been shown to remove native oxides and adsorbed contaminants by milling the surface. But, it will require annealing the substrate to 800^o C to remove surface damage from Ar milling [4] [5] [6] [7]. Using an O_2 plasma has been shown to remove organic contaminants [8]. The substrate can also be heated (from 300^o C to 800^o C) to remove adsorbed contaminants

from its surface [9] [10].

OXIDATION

Oxidation is a process which is used to grow an oxide layer. Thermal oxidation involves growing an oxide layer over a silicon substrate at high temperatures (between 700^o C to 1200^o C) [11]. It is classified into wet and dry oxidation. Wet oxidation uses H_2O vapour whereas dry oxidation uses oxygen gas for the oxide growth. It takes place under high vacuum conditions and operates at atmospheric pressures [12], to get an oxide layer free of contaminations. It is used to grow gate oxides [12], dielectrics for capacitors[13], field oxides (electrically isolate metal films from the bulk)[14], masking layers [15][16] and as passivation layers [17] [18].

DOPING

Doping is the process of introducing an impurity atom into an existing semiconductor to change its electrical properties. By doping a pentavalent (5 valence electrons) impurity like phosphorus into an intrinsic crystalline lattice of silicon we change the silicon into a n-type semiconductor. Similarly by doping the silicon with a trivalent (3 valence electrons) impurity like boron, we can change the silicon into a p-type semiconductor. This is achieved either by diffusion or ion implantation. Diffusion involves the movement of the impurity atom into the silicon crystal by heat (900 ^{o}C to 1100 ^{o}C)[19]. It generally takes place in a furnace, the impurity atoms are delivered to the silicon wafer either in gaseous form (eg. PH_3, B_2H_6) or from a solid source of the impurity atoms placed in the same boat as the silicon wafer. Ion implantation involves accelerating the impurity atoms into the silicon wafer. Ion implantation takes place at room temperature, but it requires a high temperature (900 ^{o}C to 1100 ^{o}C) activation step following implantation [19].

DEPOSITION

Deposition is a process which is used to deposit a thin film on top of a wafer. Deposition processes can be classified into physical vapor deposition (PVD) and chemical vapor deposition (CVD). PVD is a process by which the material is deposited by physical means i.e., through the transfer of material from target to substrate. CVD is a process by which the material is deposited by chemical means, i.e., by using chemical reactions. The most common PVD methods are evaporation and sputter deposition. Evaporation involves heating the target material (i.e., material to be deposited) to a temperature such that it starts to evaporate. The evaporated material condenses on a substrate normally kept at room temperature, in the case of epitaxial film the substrate is kept at a higher temperature. It is performed under high vacuum conditions (typically $10^{-6} mbar$) [20], so the

evaporated material can travel from the target to the substrate without collisions. The target material can be heated in two ways: resistively and by electron beam heating. One way is to directly heat the target material by placing the target in a metallic boat and passing a high current through the boat. This method is called thermal evaporation. Since the whole target is heated, the metallic boat has to have a lower vapour pressure to avoid contamination. Another way is to use an electron beam to focus onto the target material. This method is called electron beam evaporation. Here, the electrons are emitted from a heated filament and are accelerated towards the target material which gets hot. The temperature required to evaporate the material is material dependent [20]. A schematic of a thermal evaporation system is shown in Figure 2.1. It is directional, so there will not be any deposition on side walls of structures. It is limited to depositing metals like Al,Pt,Au,Ti,Cr,Co, Nb and Pd [21][22]. It is not possible to deposit alloys or compounds of materials from a single source, since each component will have a different vapour pressure.

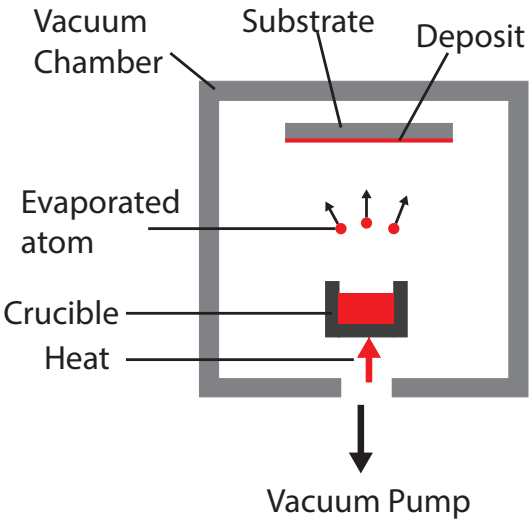

Figure 2.1: Schematic of a thermal evaporation source.

Sputter deposition involves the target material being bombarded by energetic ions, resulting in sputtering of the target atoms. The sputtered atoms travel from the target to the substrate [20]. In this method, a plasma is ignited and the energetic ions are accelerated towards the target. The bombardment of ions on the target causes the atoms to eject due to momentum transfer. The sputtered target atoms get deposited onto the wafer and the surroundings. The target is

kept at room temperature. The plasma could be ignited either by a DC or radiofrequency (RF) source. Generally RF power supply is used as it can be used for both conducting and insulating materials. So, it can be used to deposit insulating materials such as SiO_2, Al_2O_3, Si_3N_4, ITO, etc. [23][24][25]. It can also be used to deposit materials such as Au, Al, Cr, Ti, etc. It operates at pressures of 10^{-2} mbar to 10^{-1} mbar [20].

The most common CVD methods are low pressure CVD (LPCVD), plasma enhanced CVD (PECVD) and atomic layer deposition (ALD). LPCVD involves deposition due to thermal decomposition of the precursor gases containing the desired material. It operates at low pressures of (10^{-1} to 1 mbar) and at temperatures between 700^o C to 1100^o C. The substrate is kept in a quartz boat and is placed inside a hot reactor tube. The whole tube is covered by the desired material. It is used to deposit silicon nitride, silicon dioxide (SiO_2), silicon carbide and polysilicon [26][27][28]. Another type of CVD process is PECVD. In PECVD, a plasma is used to dissociate the precursor gases instead of thermal heating. This results in lower substrate temperatures ($100^o - 400^o$C). It operates at pressures of 10^{-2} mbar. An RF power supply or a microwave is used for the generation of the plasma. It is used to deposit oxides, micro-crystalline Si, a-Si, Si_3N_4, SiO_2, etc [29] [30][31][32].

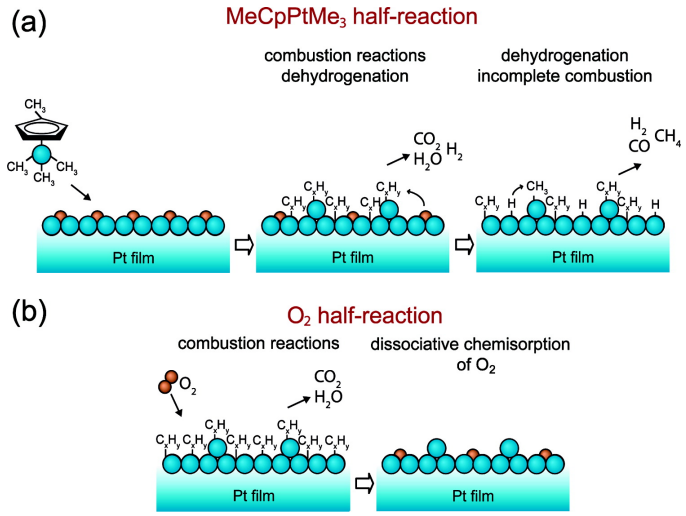

Figure 2.2: A schematic of an ALD cycle showing the four steps involves in a single cycle. a) Precursor dosing step and the purge step for the Pt deposition using the $MeCpPtMe_3$ c) Co-reactant dosing of O_2 gas and purge step. These four steps are repeated to obtain the desired thickness. Reprinted with permission from [33]. Copyright (2012) American Chemical Society.

ALD is a special type of CVD technique where a thin film is deposited, atomic

layer by layer. Here, the precursor gases are introduced in a sequential manner with a purge step in between them. The precursor gas is usually thermally dissociated by a high substrate temperature. An ALD cycle consists of precursor dosing, purge, co-reactant dosing and purge. Initially, the precursor gas is introduced into the chamber. It adsorbs onto the surface of the substrate. The precursor gas flow is stopped and the chamber is purged to remove any leftover precursor gas. Then, the reactant gas is introduced into the chamber. This reacts with the already adsorbed precursor gas molecules to grow the desired film [34][35][36][37]. A schematic of an ALD cycle is shown in figure 2.2. It is a self limiting process, there is no further growth after a sub-monolayer is formed. This results in a well defined growth per cycle (sub monolayer). A film of desired thickness could be grown based on the growth per cycle times the number of cycles. The substrate temperature is dependent on the precursor and co-reactant gas. The chamber walls and precursor gas feed lines are heated to prevent precursor condensation. This type of ALD is termed as thermal ALD. Plasma ALD utilizes a plasma for the dissociation of the precursor gas. This allows for a reduction of the substrate temperature (RT to 100^{o} C). An RF power supply is used to generate the plasma.

Area selective ALD is a technique which allows ALD growth to a predefined area. This is implemented by covering the surface by a pattern such that it either impedes the ALD growth or activates it. This can be implemented in several ways. The most common method is to coat the surface with a self assembled monolayer (SAM). SAM's are organic monolayer films, which get adsorbed onto the substrate by drop casting [38][39]. A SAM passivates the surface against ALD growth. By patterning the SAM, selective ALD growth is achieved. This passivation is achieved only for a few nanometers of growth, after which nucleation starts over the SAM as well. Another method of achieving area selective deposition for Pt and Ru ALD is to use a Pt seed layer [40][41][42][43][44], and then implementing the ALD cycle. This results in ALD growth only on the seed layer, and one can achieve a high resolution patterned ALD structure.

ALD processes take place at a base pressure of 10^{-5} mbar , operating at pressures of $1-25$ mbar and at substrate temperatures between $150-300^{0}$C. ALD is used to deposit thin uniform layers of pure metals (Pt, Pd, etc.)[35][45], dielectrics (Al_2O_3, TiO_2, HfO_2, SiO_2) [46][47][48][49] and nitrides (AlN, TiN) [50][36].

RESIST COATING

Resists are polymers which are sensitive to radiation, either photons or electrons. When a resist is exposed to radiation, its solubility to a solvent changes. Resists are classified as either positive or negative resist, if the exposed resist region becomes soluble to a solvent then it is a positive resist and vice versa for a negative

resist. This is shown in figure 2.3. The resist is generally spin coated onto the substrate. There are also new types of resists which are sensitive to temperature in addition to photons and electrons. These type of resists are termed as thermosensitive resists. One such resist is poly (phthalaldehyde) (PPA)[51]. Resists are generally applied to the substrate either by spin coating or spray coating. Spin coating involves dropping the resist solution on to the wafer and spinning the wafer at 3000 - 6000 rpm. Based on the spin speed and the dilution, a desired thickness of resist is achieved on the substrate. It takes place at ambient conditions in a wet bench to avoid any toxic fumes. After spin coating the resist, the wafer is baked at around 90 - 100 ^{o}C to improve adhesion of the resist to the wafer and to remove excess solvent [19].

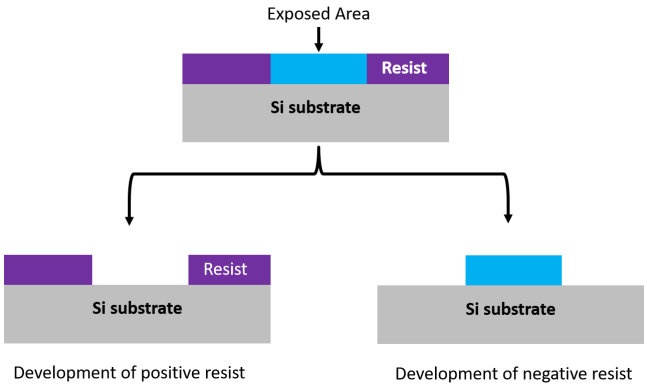

Figure 2.3: A schematic showing positive and negative resist.

EXPOSURE

Exposure is a process which is implemented after resist coating. It is used to write the desired pattern on the resist layer. This is done by photolithography or electron beam lithography (EBL). Photolithography uses photons to modify the resist. Photolithography requires the use of a mask which has the desired pattern to expose resist. It has a resolution limit which depends on the wavelength of the source used. EBL uses an electron beam to modify the resist. In EBL, there is no mask required as the beam of electrons is scanned across the substrate to create the desired pattern onto the resist [52][53][54][55][56]. As a single beam is scanned over the sample, it takes a long time to write large patterns. EBL takes place at high vacuum conditions of 10^{-6} mbar pressure at room temperature. Patterns with sub 10 nm resolution are possible with EBL. For chemically amplified resists (CARs) exposure leads to the generation of photo acid. After exposure,

the wafer is baked, changing the solubility of the resist by the catalytic reaction of the resist by the photo acid.

DEVELOPMENT

After exposure of the resist, the desired pattern is transferred into the resist. This is done by immersing the substrate in a solvent which dissolves the modified resist (positive resist). It is typically done in a wet bench at ambient conditions, so toxic fumes from the developer solutions are sucked away [19][57]. For thermosentive resists like PPA, instead of immersing the wafer in a solvent, exposing it to electrons, photons or heat will result in cross linking of the polymers to form volatile compounds. The volatile compounds are pumped away from the chamber when used in an EBL instrument [51].

ETCHING

Etching is the process of removing material from the surface of the wafer. It can be classified into wet and dry etching. Wet etching involves the use of liquid chemicals to remove material whereas dry etching involves the use of a plasma. Wet etching involves three steps: diffusion of the liquid etchant to the surface of the material, reaction between the material and the etchant and diffusion of by-products from the surface. The etch profile can either be isotropic (etch in all directions) or anisotropic (etch specific to a particular orientation). In dry etching, the mechanism that removes the material can be either be the kinetic energy of ions or a chemical reaction or a combination of both. Dry etching is classified into physical etching (sputtering), plasma etching and reactive ion etching (RIE). Figure 2.4 shows the different types of dry etching mechanisms.

Physical etching, also known as sputter etching, is the process of bombarding the surface with energetic ions, resulting in a sputter etch. It takes place at high vacuum conditions with operating pressure of 1 to 10^{-3} mbar, with usually Ar gas as the ion species. It results in an anisotropic etch, achieved by having the incident ions bombarding the surface perpendicularly and at room temperature [58][59]. An RF or DC power supply is used to create the plasma. Plasma etching is the process by which the material is removed by a chemical reaction at the surface due to the reactive ions created in the plasma. The entire surface is exposed to the plasma. It operates at high pressures of 0.1 to 1 mbar and at room temperature. It results in an isotropic etch. The gases generally used are O_2-, Cl_2- based [60][61][62][63][59][64][65]. An RF power supply is used to create the plasma. Reactive ion etching (RIE) is a combination of sputter etching and plasma etching. The etch takes place due to both physical sputtering and chemical reaction with the substrate. It takes place in a high vacuum chamber and operates at pressures of 10 to 10^{-1} mbar. It results in an anisotropic etch. The process is dependent on substrate temperature, the temperature can vary between

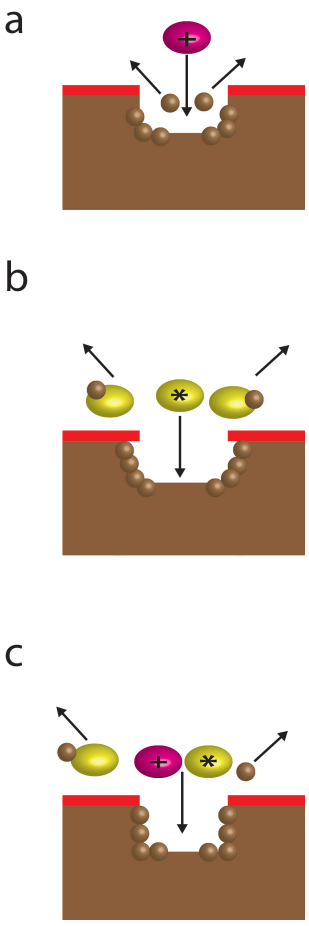

Figure 2.4: Different types of dry etching mechanisms. a) Sputter etching. b)Plasma etching. c)Reactive ion etching.

-150^o C to 30^o C. It also uses reactive gases such as BCl_3, Cl_2,SF_6, CHF_3,O_2, Ar, etc [63][62][61][65][66]. An RF power supply is used to create the plasma.

RESIST STRIP

It involves removing the unexposed resist (positive resist) from the substrate. It is done either by immersing the wafer in a solvent or an oxygen plasma. The solvent dissolves the remaining resist, resulting in a clean surface. The solvent method takes place in a wet bench at atmospheric conditions. Since the resist is made of polymers, exposing the wafer to an oxygen plasma results in combustion of the resist layer. This results in a substrate free of the resist layer. This process is also called plasma ashing [67]. It takes place in a vacuum chamber and operates at a pressure of 1 mbar. The plasma is generally powered by an RF power source with O_2 as the gas and at substrate temperatures between 150-300^o C.

INSPECTION TOOLS

Immediately after fabrication or in between different processes, the substrate is inspected to check for the surface topography and cross-section (etch depth or deposited height). This is done typically using the following tools.

PROFILOMETER

A profilometer is an inspection tool, which is used to measure step height and roughness of a substrate. This is implemented by bringing a needle (diamond tip) in contact with the substrate and scanning it across the substrate. Any change in height of the needle as it is swept across the substrate is measured and displayed. It can typically measure heights larger than 1 nm across a distance of hundreds of microns [68].

ATOMIC FORCE MICROSCOPY

Atomic force microscopy (AFM) is an inspection tool similar to a profilometer but with a very high resolution. It is used to image the surface at very high resolution, measure step height and roughness of the surface. It consists of a cantilever with a sharp tip. It operates in two modes: contact and non contact (tapping). In contact mode, the AFM tip is brought near the surface and scanned over the surface. The AFM tip and the surface are kept at a constant force or constant height. In the case of constant force, any change in the force is measured as the topography of the surface. In tapping mode, the tip is again brought close to the surface, and the tip is oscillated at or near the resonant frequency of the cantilever. As the tip is scanned across the surface, any change in the amplitude of oscillation is measured as the topography of the surface. It generally operates at ambient air but it can also be used in vacuum.

SCANNING ELECTRON MICROSCOPY

A scanning electron microscope (SEM) is a powerful inspection instrument. It is generally used to inspect the topography of a surface and cross-sections. Topographic details can be determined at a high resolution (sub 10 nm) using an SEM. It is used generally in between steps or after the entire fabrication process.

Our goal is to integrate some of the above techniques in an SEM. Why do we want to integrate the techniques into an SEM? Why not into a high vacuum chamber? What makes the SEM an ideal tool for the integration of other tools? Before we can answer these questions, lets learn how an SEM works and appreciate its versatility as an inspection instrument.

2.3. SCANNING ELECTRON MICROSCOPE

An SEM can be split up into the following parts: The electron column, a vacuum chamber housing the substrate, detectors and electronics. The electron column consists of an electron gun, condenser lenses, apertures and an objective lens. Electrons are generated by the electron gun. An electron gun consists of an electron emitter, extractor and a gun lens. A stream of electrons are emitted from the emitter. The emitter can be either a tungsten hairpin source or a Schottky source or a cold field emitter. If the emitter is kept at a high temperature, it is a tungsten hairpin. Due to the high temperature, electrons overcome the work function and leave the metal. If the emitter is kept cold and electrons are emitted by tunnelling due to a high electric field, it is a cold field emitter source. A Schottky source combines heating and a high electric field and ZrO_2 to lower the work function, causing the electrons to leave the metal. The emitted electrons are accelerated by the extractor. The emitted electrons are accelerated (1 kV to 30 kV) and focussed by the condenser and objective lenses. Fig 2.5 shows a schematic of an SEM column. The current of the electron beam is limited by a variable aperture.

After the electrons emerge from the aperture, the beam is focussed onto the specimen by the objective lens. The specimen is housed in a vacuum chamber directly below the objective lens. The specimen or the substrate is mounted to a 5 axis stage (X,Y,Z,rotation and tilt). The beam of electrons (primary electrons) is scanned over the surface of the sample by scan coils present in the objective lens. The electron beam penetrates and scatters inside the substrate. The scattering can either be elastic, if the electron is scattered without any loss of energy, or inelastic, if the electron loses kinetic energy and transfer that energy to the substrate. Due to scattering, the electron beam spreads laterally and into the substrate, forming an interaction volume larger than the beam diameter. Elastic scattering occurs when the electron beam is deflected by the nuclei. These

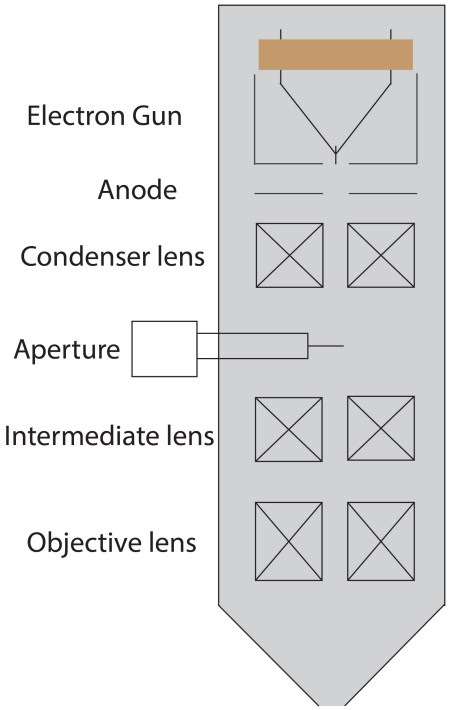

Figure 2.5: Schematic of an SEM column.

deflected electrons when they scatter back up are called backscattered electrons (BSE) which can be detected by a detector to form a backscattered electron image. Inelastic scattering causes electrons in a substrate to eject from the surface, these electrons are called secondary electrons (SE). These SE's are detected by a detector to form a secondary electron image of the substrate. Electrons emitted from the substrate with energy less than 50 eV are classified as SE and electrons with higher kinetic energy than 50 eV are classified as BSE. The SE and BSE emitted from the substrate are collected by dedicated detectors housed within the vacuum chamber.

The SE emitted from the substrate possess low energy and are attracted towards the detector by applying a positive potential to a grid (Faraday cage). The electrons collected by the Faraday cage hit a scintillator surface. A scintillator converts the electrons into photons. The emitted photons are multiplied by a photomultiplier tube (PMT). In the PMT, the photons are converted to electrons. The electrons are amplified and converted into an image and displayed in a monitor. Energy dispersive X-ray spectroscopy (EDX) is a material analysis technique

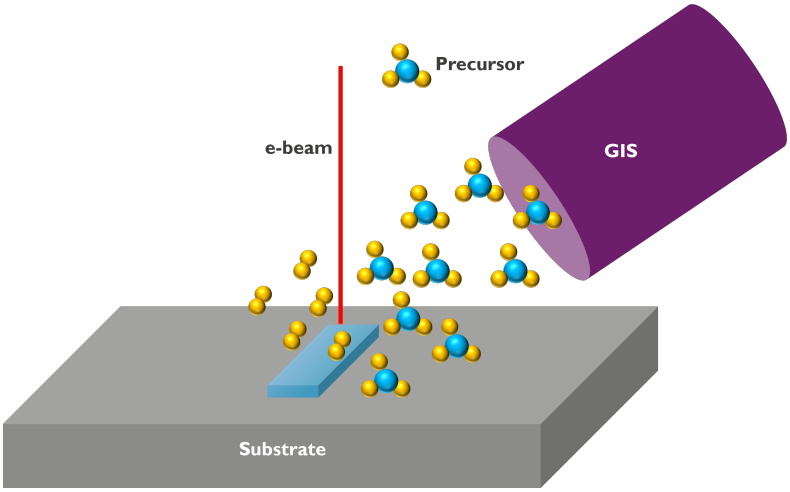

Figure 2.6: Illustration of a FEBID process.

that is available in an SEM with an EDX detector. When an electron beam is incident on a substrate, it may excite an inner shell electron ejecting it from the atom. This results in a vacant inner shell, an outer shell electron can fill this vacancy resulting in the emission of X-ray radiation. The EDX detector detects the energy of these X-rays. The energy of the emitted X-rays is equal to the difference in energy between the inner and outer shells.

A dual beam instrument has a focussed ion beam (FIB) column in addition to an SEM column. A FIB is very similar to an SEM: instead of a beam of electrons, a beam of ions (typically Ga) is focussed on to the substrate. The ion column is generally mounted at an angle of 52^o with respect to the electron column (for a ThermoFisher Scientific dual beam instrument). Unlike electrons, when heavy Ga ions are scanned over the substrate, the substrate atoms are sputtered away due to momentum transfer. This is the unique feature of a FIB column, it can be used to mill precise patterns on a substrate.

Focussed electron beam induced processing (FEBIP) is a technique which is available in an SEM. FEBIP is a high resolution direct write technique, it can be used either to deposit material, focussed electron beam induced deposition (FEBID) or etch the material, focussed electron beam induced etching (FEBIE) [69] [70]. In FEBID precursor gas containing the material to be deposited is directed and injected towards the substrate by a nozzle assembly called the gas injection system (GIS). The injected gas molecules get adsorbed on the surface of the substrate. When an electron beam is scanned over the substrate, the electron beam dissociates the adsorbed precursor molecules. The volatile fragments

get pumped out and the non-volatile fragments get deposited onto the substrate [71][72][73] [70]. An illustration of FEBID is shown in figure 2.6. Similarly, in the case of FEBIE the non-volatile fragments of the adsorbed precursor molecules react with the substrate to produce volatile fragments resulting in an etch [69]. FEBID has been shown to deposit a variety of materials like Pt, Au, SiO_x, Co, Fe, etc. [74]. FEBIE has been shown to etch silicon, carbon nanotubes, graphene, boron nitride, etc. [69][75][76][77][78][79]. Similar to FEBID and FEBIE, we can deposit and etch materials using the ion beam, focussed ion beam induced deposition (FIBID) and focussed ion beam induced etching (FIBIE)[80][81].

The main disadvantage of FEBID is its low purity deposits. For example, Pt deposited by the methylcyclopentadienyl trimethyl platinum ($MeCpPtMe_3$) precursor results in a deposit with ~15 at% of Pt and the rest of the deposit being carbon [82]. The resistivity of the deposit is six orders higher than the resistivity of bulk Pt. Post purification strategies have been employed to get pure Pt deposits by annealing the substrate in an oxygen or air environment [83][84][85][86][87][88][89]. Using the ion beam for deposition has resulted in purer deposits than using electrons. One disadvantage of using an ion beam to deposit material is that the Ga ions are also implanted into the deposit and simultaneous milling.

In addition to being used as an inspection tool, resist-based lithography can also be done inside an SEM. With the addition of a fast beam blanker and pattern generator, electron beam lithography has been demonstrated in an SEM. An SEM is generally used as an EBL tool for research purposes. Oxidation in an SEM using the electron beam has also been demonstrated. FEBID deposits has been shown as etch masks for transferring pattern onto the underlying substrate [90][91]. Silicon cantilever tips have been manufactured using FEBIE [92]. FEBIP has been demonstrated for the use of mask repair [93].

2.3.1. DESCRIPTION OF THE NOVA NANO SEM

All work in this thesis was performed in a Thermo Fisher Scientific (formerly FEI) Nova nano SEM. It is a dual beam instrument, the electron column is placed perpendicular to the substrate and the ion column is placed at 52^o with respect to the substrate. It is equipped with a 5 axis stage (X, Y, Z, rotation and tilt). The working pressure of the SEM is 10^{-6} to 10^{-5} mbar. It is also equipped with a GIS for Pt FEBID and H_2O FEBIE. EDX is also possible within the SEM by means of an EDX detector. We use an Oxford instruments X-max 80 mm^2 Solid State EDX detector. We also have the possibility of using an AFM inside the SEM (NanoAnalytik GmbH). Figure 2.7 shows the photograph of the AFM mounted onto the stage of the SEM. The Si cantilever AFM tips contain a thermo-mechanical actuator and a piezoresistive sensor consisting of a Wheatstone bridge is used as the detector to measure the deflection of the Si cantilever. The SEM is also equipped

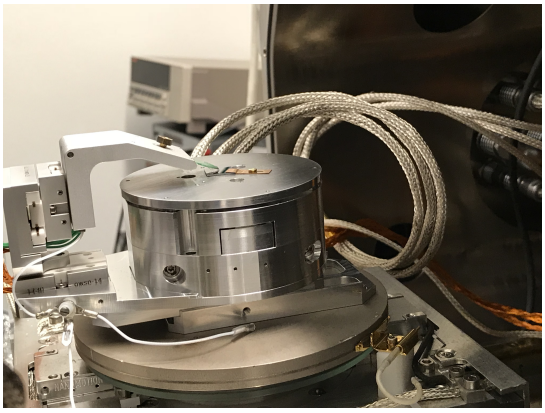

Figure 2.7: Photograph showing the in-situ AFM mounted onto the SEM stage.

with a load lock for quick sample exchange and maintaining a clean chamber. It is also equipped with a commercial plasma cleaning tool to clean the chamber. The various components of the SEM are shown in Figure 2.8. Figure 2.8 also shows the various add-ons available in the system like EDX, GIS, AFM, plasma clean and a multi beam unit. The multi beam unit converts a single beam into 25 beams, it is designed to fit in the aperture port[94]. Even though we have the capability for a multi beam, we won't be using this in the rest of the thesis.

2.3.2. RESTRICTIONS

There are several restrictions on bringing materials or processes into the SEM. an SEM normally operates between a chamber pressure of 10^{-6} and 9.10^{-5} mbar. Even though the chamber pressure is in the high vacuum range, the electron gun is kept at ultra high vacuum (10^{-9} to 10^{-10}mbar). The source area and the vacuum chamber are separated by differential pumping. An increase of the chamber pressure beyond 9.10^{-5} mbar will trigger closing off the valves between the source area and the chamber column.

Any material brought inside the SEM chamber shouldn't outgas into the chamber. Outgassing will lead to an increase in chamber pressure and will also contaminate the chamber. Any contamination in the chamber can travel to the aperture where it can be deposited, leading to charging which may affect the beam quality. Also contamination will lead to deposition on to the substrate whenever we scan over the substrate. This is typically observed as the darkening of the SEM image after parking or scanning the beam. To prevent contamination of the chamber and other components, each element brought inside the SEM should

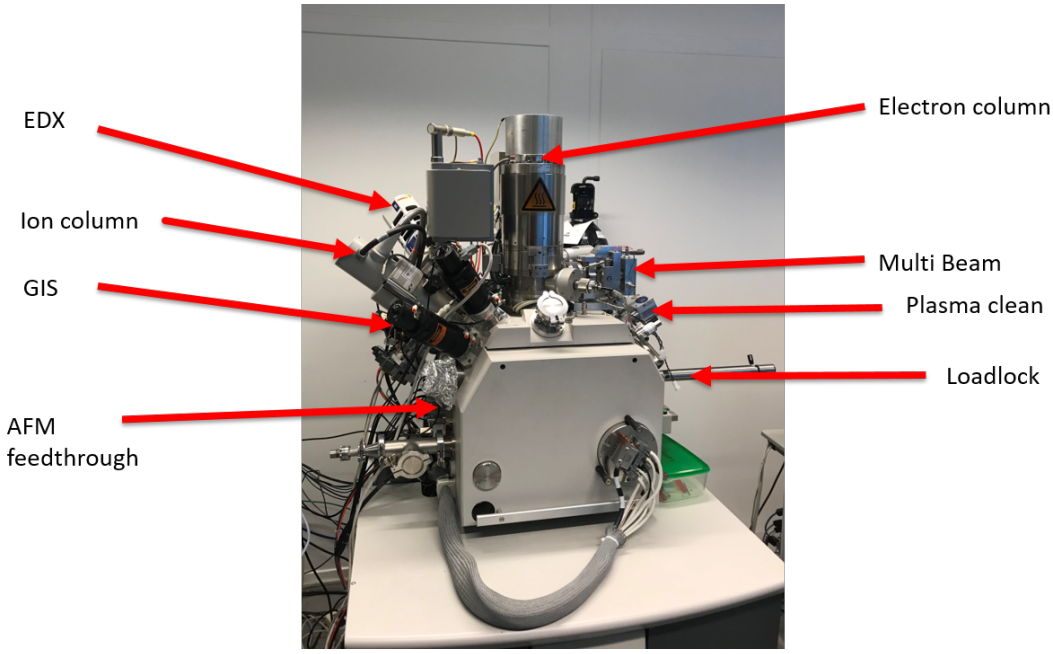

Figure 2.8: Photograph of the Thermo Fisher Scientific Nova nano 600i dual beam system with all the add-ons.

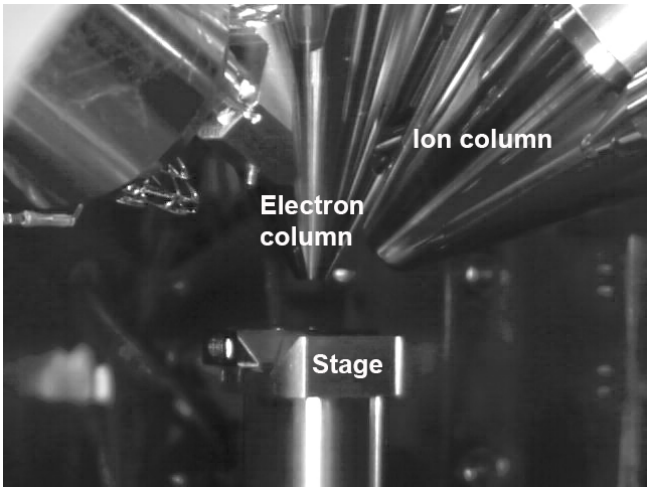

Figure 2.9: Photograph showing the space available in the SEM.

be cleaned in acetone followed by ethanol or IPA.

Insulating materials in direct line of sight of the beam will result in charging. Similarly, magnetic fields inside the chamber will distort the beam. So, all components for tools inside the SEM should be non magnetic. In addition, the available space under the beam is limited. This is shown in Figure 2.9. Any addition to the chamber should stay clear of the objective lens (pole piece). Any gas chemistry introduced into the SEM chamber shouldn't damage any of the detectors nor the pole piece. The piezoelectric stage and the detectors have delicate components so they should be kept at room temperature.

WHY INTEGRATE CLEANROOM TOOLS IN AN SEM ?

Why do we want to integrate different cleanroom techniques in an SEM ? An SEM already operates at high vacuum pressure, so it has already in place a vacuum chamber with pumps. It is already an integral part of a device fabrication process as an inspection tool. With the addition of an EDX detector, we can use it as a material analysis tool. A dual beam instrument will give us, in addition to inspection, high resolution milling capabilities. With the Nova nano lab SEM we have the capability to add an AFM in SEM to measure the height of patterned structures. Thus, we have the capability to use it as inspection tool (imaging, AFM and EDX), lithography tool (FEBID masks and resists), deposition tool (FEBID and FIBID) and etching tool (FEBIE, FIB and FIBID). Moreover for research purposes the region of interest is a few square microns. All the cleanroom fabrication tools we discussed before are designed to handle 2" or 4" wafers. Cleanrooms are expensive, for example at the Kavli nanolab, TU Delft, it costs about 150 Euro per hour for the maintenance of the cleanroom in addition to the cost of operating the instruments. An SEM is already a versatile instrument for nanofabrication. Moreover, an SEM is available in almost all labs. By complementing it with other fabrication techniques, we are able to achieve a cleanroom inside an SEM.

2.4. TECHNIQUES TO INTEGRATE IN AN SEM

Now, we will choose appropriate techniques needed to fabricate a complete device inside the SEM. An SEM operates under high vacuum (10^{-6} to 10^{-5} mbar) conditions. So, the first requirement is to choose techniques that can operate under high vacuum conditions, such that the normal operation of the SEM is not affected. The operating conditions of the various fabrication techniques discussed before are shown in table 2.1. From the table, we can see that evaporation and exposure satisfy the requirement. Exposure is already possible using the SEM. Also, we already use precursors for FEBID, FEBIE, FIBID and FIBIE. We could modify the GIS for delivering other gases into the SEM for purification

Table 2.1: Process parameters of different fabrication tools

Cleanroom techniques	Operating Conditions					Integrate in SEM			Considerations
	Base pressure	Operating Pressure (mbar)	Temperature (^{o} C)	Gases used	Control units	Pressure	Temperature	Material	
Cleaning									
Wet clean	No	ambient	RT to 70	Liquid chemicals	hot plate	×	×	×	
Dry clean	HV	0.1 to 10	300 - 800	O_2, Ozone	RF, UV light, heater	✓	×	✓[1]	
Oxidation	HV	1000	700 - 1200	H_2O, O_2	Substrate heater	×	×	✓[1]	
Local Oxidation	HV	10^{-5}	RT	H_2O, O_2	e-beam	✓	✓	✓	
Deposition									
Evaporation	HV	10^{-6} to 10^{-8}	RT	None	resistive or e-beam	✓	✓	✓	
Sputter Deposition	HV	10^{-1} to 10^{-2}	RT	Ar	RF or DC	×	✓	✓[1]	
LPCVD	LV	1 to 10^{-1}	700 - 1100	N_2, precursor gases	furnace	×	×	✓[1]	[2]
PECVD	HV	10^{-2}	100- 400	Ar, CH_4,SiH_4	RF or Microwave	×	×	✓[1]	[2]
ALD	HV	1 to 25	100-300	Precursors and Co-reactants	RF, substrate heater	×	×	✓[1]	[2]
Resist Coating	ambient	1000	50- 200	resist	spinner	×	×	×	
E-beam Exposure	HV	10^{-6}	RT	-	e-beam	✓	✓	✓	
Etching									
Sputter Etching	HV	1 to 10^{-3}	RT	Ar		×	✓	✓[1]	
Plasma Etching	HV	0.1 to 1	RT	O_2, Cl_2	RF	×	✓	✓[1]	[2]
RIE	HV	0.1 to 10	-150^o C to 30^o C	BCl_3, Cl_2,SF_6, CHF_3,O_2, Ar	RF	×	×	✓[1]	[2]
Resist stripping	LV	1	150^o C to 300^o C	O_2	RF	×	×	✓[1]	
Inspection									
EDX	HV	10^{-6} to 10^{-5}	RT	None	e-beam	✓	✓	✓	
SEM	HV	10^{-6} to 10^{-5}	RT	None	e-beam	✓	✓	✓	
AFM	ambient to HV	1000 to 10^{-6}	RT	None	AFM unit	✓	✓	✓	
FIB	HV	10^{-6} to 10^{-5}	RT	None	I-beam	✓	✓	✓	

1 Modify GIS for gas delivery

2 precursor should not react with other components in the SEM

of FEBID deposits [85]. A typical process flow in the cleanroom looks like this: cleaning, deposition, lithography (spin coat resist, exposure and development), etching, resist strip and inspection. Based on this process flow for the fabrication of an entire device within the SEM, we would need the miniaturisation and integration of the following tools: a cleaning procedure, a deposition tool and an etching tool. Even though we have FEBID as a deposition tool, it does not produce high purity deposits. Therefore we need another deposition tool. In the case of FIB, there is the unwanted deposition of Ga ions, therefore we need another etching tool as well. We can use FEBID structures as hard masks for pattern transfer.

2.4.1. CLEANING

The first step in any process flow is the cleaning step. Wet chemical based cleaning is not vacuum compatible and would require a lot of modifications (chemical inlet, outlet, reactive chemicals, etc.) to an already existing SEM. So, the next option is the dry cleaning method. The Nova nano lab SEM is equipped with a commercial plasma cleaner for the cleaning of the chamber. The other method in dry cleaning is to heat the substrate. With a heater, we would be able remove adsorbed contaminants from the surface of the substrate by heating the substrate to a high temperature of about 300^o C [9][10]. We can also use it for FEBID purification strategies as well as for other processes like ALD. The maximum temperature will need to be selected such that it is within the thermal limits of the stage and detectors. The stage is very sensitive to temperature. So, we need to develop a dedicated heater.

2.4.2. DEPOSITION

Next, we need to have a deposition tool inside the SEM. As discussed before deposition can be implemented by either PVD or CVD. In PVD techniques, we have sputter deposition and evaporation both operate in vacuum. Sputter deposition requires a plasma for operation, and as seen from table 2.1, it also operates at a higher chamber pressure. It deposits everywhere, which can become a problem with dielectrics. Evaporation operates at ultra high vacuum, it satisfies the pressure requirement. The substrate is typically kept at room temperatures. It is directional, so we would be able to limit the area of deposition to the substrate. We will be able to choose the deposition area based on the distance between the evaporation source and the substrate. So, it is feasible to integrate this into an SEM. In CVD techniques, we have LPCVD, PECVD and ALD. We can eliminate LPCVD as it operates at high pressures which conflicts with normal SEM operation. Also LPCVD requires a substrate temperature above 600^o C. PECVD

operates at even higher pressures and it would require a substrate temperature of 300^o C along with a plasma. It's working pressure conflicts with the normal operation of SEM. So we can eliminate this too. ALD operates at high pressure with substrate temperatures around 300^o C. On first glance, this technique also conflicts with the SEM. But, we know from FEBID, the GIS creates a local high pressure at the surface of the substrate. Also, both Pt FEBID and Pt ALD use the same precursor, $MeCpPtMe_3$. Area selective ALD using Pt FEBID as a seed layer is a direct write technique which combines the high resolution of FEBID with the high purity of ALD. The requirements for implementing this technique are O_2 gas injection as a co-reactant and a substrate temperature of 300^o C. This also seems feasible to integrate in an SEM by utilizing the GIS to deliver a local gas pressure near the substrate.

2.4.3. ETCHING

An important step in the cleanroom process flow is etching. Here we have reactive ion etching, plasma etching and sputter etching. RIE operates at pressures of 10 to 10^{-1} mbar and substrate temperatures (-150 to 30^o C) and a plasma to create the reactive ions. It requires the use of reactive gases such as SF_6, $SiCl_4$, etc., which can be reactive with the pole piece, stage or the detectors. So, we can eliminate RIE. Plasma etching operates at pressures of 0.1 to 1 mbar and requires a plasma. It also requires the use of reactive gases. Hence, we can eliminate this too. We are left with sputter etching, which is the basic type of an etching tool. It operates at 1 to 10^{-3} mbar pressure. It requires a working plasma for the generation of ions. With a working plasma inside the SEM, we would be able to implement sputter etching inside the SEM. The main challenge here is to bridge the gap in pressure. This will also open up possibilities for other techniques (Plasma etching and RIE) which would require a plasma for operation. This seems feasible to develop inside an SEM.

2.5. CONCLUSION

We decided to concentrate on implementing the following techniques inside the SEM. i) A substrate heater, which can be used for removing adsorbed contaminants and water vapour from the substrate. It can also be used for FEBID purifications as well as for ALD. The development of the substrate heater will be discussed in detail in chapter 3. ii) In-situ area selective ALD using the GIS, with this technique we will be able to combine the high resolution feature of FEBID with the high purity aspect of ALD. The development of the in-situ area selective ALD is described in chapter 4. iii) A thermal evaporator, which will enable to locally deposit a pure material inside the SEM. The development of the miniature

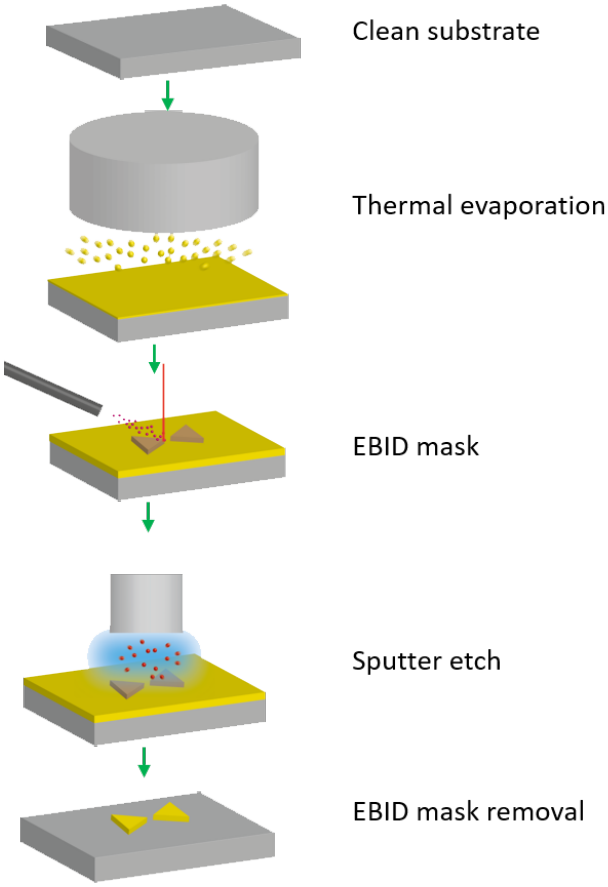

Figure 2.10: Proposed process flow inside the SEM with the feasible techniques which can be integrated inside the SEM.

thermal evaporator is described in chapter 5. iv) A sputter etching tool, which will enables local etching of material inside the SEM. The development of the sputter etching tool is described in chapter 6.

With the above techniques, we will already be able to completely fabricate a device inside the SEM, without breaking the vacuum between the different process steps. A proposed process flow for fabricating a bow tie antenna inside the SEM based on the above techniques is shown in figure 2.10. We begin the process by loading a clean substrate inside the SEM. We locally deposit the target material by using the miniature thermal evaporator. We use FEBID (for instance carbon) to deposit the desired pattern, here a bow tie structure. This FEBID structure is used as a hard mask. After the FEBID mask step, we transfer the pattern onto

the underlying material by using the miniature sputter etching tool. Finally, we remove the left over FEBID mask by using FEBIE (H_2O). Now, we are left with the desired pattern, a bow tie antenna on the deposited material.

We could develop the techniques listed in this chapter, and integrate them in an SEM. But there are limitations in fabricating a active device like a transistor. Techniques like resist coating, LPCVD and oxidation which are essential in the fabrication of an active device like a transistor are not feasible to integrate in an SEM. But, local oxidation by electron beam irradiation has been demonstrated [95][96]. Thus, local oxidation could be carried out in the SEM. Currently transistors utilize a high-k dielectric material as the insulator rather than SiO_2. One of the methods of growing high-k dielectrics is by ALD. So, by choosing an appropriate precursor and co-reactant which can be compatible in the SEM, we would be able to grow a high-k dielectric material by using the in-situ ALD in SEM. With a working sputter etching tool, we would overcome the pressure requirement. Thus, plasma etching can be implemented by replacing the Ar gas used for sputter etching with O_2. Similarly, RIE could be implemented for processes which operate at room temperature.

REFERENCES

[1] W. Kern, *Handbook of Silicon Wafer Cleaning Technology*, 2nd ed. (Elsevier Inc., 2008) pp. 3–92.

[2] J. R. Vig, *UV/Ozone Cleaning of Surfaces,* Journal of Vacuum Science and Technology A **3**, 1027 (1985).

[3] S. R. Kasi and M. Liehr, *Preoxidation Si cleaning and its impact on metal oxide semiconductor characteristics,* Journal of Vacuum Science and Technology A **10**, 795 (1992).

[4] J. C. Bean, G. E. Becker, P. M. Petroff, and T. E. Seidel, *Dependence of residual damage on temperature during Ar + sputter cleaning of silicon,* Journal of Applied Physics **48**, 907 (1977).

[5] G. Margaritondo, J. E. Rowe, and S. B. Christman, *Surface spectroscopy of Schottky-barrier formation on Si(111) 7 × 7: Photoemission studies of filled surface states and band bending,* Physical Review B **14**, 5396 (1976).

[6] J. H. Comfort, L. M. Garverick, and R. Reif, *Silicon surface cleaning by low dose argon-ion bombardment for low-temperature (750 °C) epitaxial silicon deposition. I. Process considerations,* Journal of Applied Physics **62**, 3388 (1987).

[7] S. Salimian and M. Delfino, *Removal of native silicon oxide with low-energy argon ions,* Journal of Applied Physics **70**, 3970 (1991).

[8] R. E. Robinson, R. L. Sandberg, D. D. Allred, A. L. Jackson, J. E. Johnson, W. Evans, T. Doughty, A. E. Baker, K. Adamson, and A. Jacquier, *Removing Surface Contaminants from Silicon Wafers to Facilitate EUV Optical Characterization,* in *47th Annual Technical Conference Proceedings of the Society of Vacuum Coaters, Dallas TX, (Society of Vacuum Coaters, Albuquerque, NM, 24)*, Vol. 47 (2004) pp. 368–376.

[9] K. Saga and T. Hattori, *Characterization of trace organic contamination on silicon surfaces in semiconductor manufacturing,* in *Analytical and Diagnostic Techniques for Semiconductor Materials, Devices, and Processes*, Vol. 03 (2003) pp. 136–149.

[10] P. J. Smith and P. M. Lindley, *Analysis of organic contamination in semiconductor processing,* AIP Conference Proceedings **449**, 133 (1998).

[11] B. E. Deal and A. S. Grove, *General relationship for the thermal oxidation of silicon,* Journal of Applied Physics **36**, 3770 (1965).

[12] K. I. Lundström, M. S. Shivaraman, and C. M. Svensson, *A hydrogen-sensitive Pd-gate MOS transistor,* Journal of Applied Physics **46**, 3876 (1975).

[13] J. L. Sprague, J. A. Minahan, and O. J. Wied, *Physical and Dielectric Properties of the Metal-Silicon Dioxide-Silicon System,* Journal of The Electrochemical Society **109**, 94 (1962).

[14] S. C. Arney and N. C. MacDonald, *Formation of submicron silicon-on-insulator structures by lateral oxidation of substrate-silicon islands,* Journal of Vacuum Science & Technology B: Microelectronics Processing and Phenomena **6**, 341 (1988).

[15] R. N. Ghoshtagore, *Silicon dioxide masking of phosphorus diffusion in silicon,* Solid State Electronics **18**, 399 (1975).

[16] Z. Liu, A. Shah, T. Alasaarela, N. Chekurov, H. Savin, and I. Tittonen, *Silicon dioxide mask by plasma enhanced atomic layer deposition in focused ion beam lithography,* Nanotechnology **28** (2017), 10.1088/1361-6528/aa5650.

[17] T. Ohmi, M. Morita, A. Teramoto, K. Makihara, and K. S. Tseng, *Very thin oxide film on a silicon surface by ultraclean oxidation,* Applied Physics Letters **60**, 2126 (1992).

[18] A. Moldovan, F. Feldmann, M. Zimmer, J. Rentsch, J. Benick, and M. Hermle, *Tunnel oxide passivated carrier-selective contacts based on ultra-thin SiO2 layers,* Solar Energy Materials and Solar Cells **142**, 123 (2015), proceedings of the 5th International Conference on Crystalline Silicon Photovoltaics (SiliconPV 2015).

[19] M. Plummer, J.D. amd Deal and P. Griffin, *Silicon VLSI Technology: Fundamentals, Practice and Modelling* (Prentice Hall, 2001).

[20] H. H. Gatzen, V. Saile, and J. Leuthold, *Deposition Technologies,* in *Micro and Nano Fabrication: Tools and Processes* (Springer, Berlin, Heidelberg, 2015) pp. 65–203.

[21] H. Frey, *Handbook of Thin-Film Technology*, edited by H. Frey and H. R. Khan (Springer, Berlin, Heidelberg, 2015) pp. 13–71.

[22] M. Ohring, *Materials Science of Thin Films* , 2nd ed., edited by M. Ohring (Academic Press, San Diego, 2002) pp. 95 – 144.

[23] C. A. Ross and J. J. Barrese, *Mechanical Properties of Alumina Films Sputtered Over Steps,* MRS Proceedings **356**, 201 (1994).

[24] W. J. Coleman, *Evolution of Optical Thin Films by Sputtering,* Appl. Opt. **13**, 946 (1974).

[25] M. Gross, S. Kong, C. Horwitz, and C. Kwok, *Hollow cathode deposition of silicon dioxide films,* Thin Solid Films **193-194**, 138 (1990).

[26] J. M. Olson, *Analysis of LPCVD process conditions for the deposition of low stress silicon nitride. Part I: preliminary LPCVD experiments,* Materials Science in Semiconductor Processing **5**, 51 (2002).

[27] K. Jhansirani, R. S. Dubey, M. A. More, and S. Singh, *Deposition of silicon nitride films using chemical vapor deposition for photovoltaic applications,* Results in Physics **6**, 1059 (2016).

[28] G. Harbeke, *Growth and Physical Properties of LPCVD Polycrystalline Silicon Films,* Journal of The Electrochemical Society **131**, 675 (1984).

[29] E. Ermakova, Y. Rumyantsev, A. Shugurov, A. Panin, and M. Kosinova, *PECVD synthesis, optical and mechanical properties of silicon carbonnitride films,* Applied Surface Science **339**, 102 (2015).

[30] J. Schmidt and M. Kerr, *Highest-quality surface passivation of low-resistivity p-type silicon using stoichiometric PECVD silicon nitride,* Solar Energy Materials and Solar Cells **65**, 585 (2001).

[31] L. Guo, M. Kondo, M. Fukawa, K. Saitoh, and A. Matsuda, *High Rate Deposition of Microcrystalline Silicon Using Conventional Plasma-Enhanced Chemical Vapor Deposition,* Japanese Journal of Applied Physics **37**, L1116 (1998).

[32] W. Soppe, H. Rieffe, and A. Weeber, *Bulk and surface passivation of silicon solar cells accomplished by silicon nitride deposited on industrial scale by microwave PECVD,* Progress in Photovoltaics: Research and Applications **13**, 551 (2005).

[33] A. J. M. Mackus, N. Leick, L. Baker, and W. M. M. Kessels, *Catalytic Combustion and Dehydrogenation Reactions during Atomic Layer Deposition of Platinum,* Chemistry of Materials **24**, 1752 (2012).

[34] T. Aaltonen, A. Rahtu, M. Ritala, and M. Leskelä, *Reaction Mechanism Studies on Atomic Layer Deposition of Ruthenium and Platinum,* Electrochemical and Solid-State Letters **6**, C130 (2003).

[35] T. Aaltonen, M. Ritala, T. Sajavaara, J. Keinonen, and M. Leskelä, *Atomic layer deposition of platinum thin films,* Chemistry of Materials **15**, 1924 (2003).

[36] H. Knoops, S. Potts, A. Bol, and W. Kessels, *Handbook of Crystal Growth*, 2nd ed., edited by T. F. Kuech (North-Holland, Boston, 2015) pp. 1101 – 1134.

[37] M. Fang and J. C. Ho, *Area-Selective Atomic Layer Deposition: Conformal Coating, Subnanometer Thickness Control, and Smart Positioning,* ACS Nano **9**, 8651 (2015).

[38] E. Farm, *Selective-Area Atomic Layer Deposition*, Ph.D. thesis, Department of Chemistry Faculty, University of Helsinki, Finland (2011).

[39] R. Chen, H. Kim, P. C. McIntyre, D. W. Porter, and S. F. Bent, *Achieving area-selective atomic layer deposition on patterned substrates by selective surface modification,* Applied Physics Letters **86**, 191910 (2005).

[40] A. Mackus, W. Kessels, and J. Mulders, *Selective in-situ atomic layer deposition on structures created with EBID,* Microscopy and Analysis **25(4)**, 5 (2011).

[41] A. J. M. Mackus, J. J. L. Mulders, M. C. M. van de Sanden, and W. M. M. Kessels, *Local deposition of high-purity Pt nanostructures by combining electron beam induced deposition and atomic layer deposition,* Journal of Applied Physics **107**, 116102 (2010).

[42] A. J. M. Mackus, S. A. F. Dielissen, J. J. L. Mulders, and W. M. M. Kessels, *Nanopatterning by direct-write atomic layer deposition,* Nanoscale **4**, 4477 (2012).

[43] A. J. M. Mackus, *Atomic layer deposition of Pt and its combination with electron beam induced deposition for the fabrication of nanostructures,* Master's thesis, Eindhoven University of Technology, Department of Applied Physics Plasma (2009).

[44] M. Junige, M. Löffler, M. Geidel, M. Albert, J. W. Bartha, E. Sschech, B. Rellinghaus, and W. F. van Dorp, *Area-selective atomic layer deposition of Ru on electron-beam-written Pt (C) patterns versus SiO2 substratum,* Nanotechnology **28**, 395301 (2017).

[45] A. M. Molenbroek, S. Haukka, and B. S. Clausen, *Alloying in Cu/Pd Nanoparticle Catalysts,* The Journal of Physical Chemistry B **102**, 10680 (1998).

[46] L. Hiltunen, H. Kattelus, M. Leskelä, M. Mäkelä, L. Niinistö, E. Nykänen, P. Soininen, and M. Tiittad, *Growth and characterization of aluminium oxide thin films deposited from various source materials by atomic layer epitaxy and chemical vapor deposition processes,* Materials Chemistry and Physics **28**, 379 (1991).

[47] M. Rose, J. Niinistö, P. Michalowski, L. Gerlich, L. Wilde, I. Endler, and J. W. Bartha, *Atomic Layer Deposition of Titanium Dioxide Thin Films from Cp*Ti(OMe)3 and Ozone,* The Journal of Physical Chemistry C **113**, 21825 (2009).

[48] K. Black, H. C. Aspinall, A. C. Jones, K. Przybylak, J. Bacsa, P. R. Chalker, S. Taylor, C. Z. Zhao, S. D. Elliott, A. Zydor, and P. N. Heys, *Deposition of ZrO2 and HfO2 thin films by liquid injection MOCVD and ALD using ansa-metallocene zirconium and hafnium precursors,* J. Mater. Chem. **18**, 4561 (2008).

[49] S. W. King, *Plasma enhanced atomic layer deposition of SiNx:H and SiO2,* Journal of Vacuum Science & Technology A **29**, 041501 (2011).

[50] J. Y. Kim, G. H. Choi, Y. D. Kim, Y. Kim, and H. Jeon, *Comparison of TiN Films Deposited Using Tetrakisdimethylaminotitanium and Tetrakisdiethylaminotitanium by the Atomic Layer Deposition Method,* Japanese Journal of Applied Physics **42**, 4245 (2003).

[51] *http://www.allresist.com/patterning-of-polyphthalaldehydes-with-photolithography/,* (accessed February 14, 2020).

[52] L. Couraud, A. Lebib, C. Vieu, H. Launois, L. Manin-Ferlazzo, Y. Chen, M. Mejias, a. Pépin, and F. Carcenac, *Electron beam lithography: resolution limits and applications,* Applied Surface Science **164**, 111 (2000).

[53] W. W. Hu, K. Sarveswaran, M. Lieberman, and G. H. Bernstein, *Sub-10 nm electron beam lithography using cold development of poly(methylmethacrylate),* Journal of Vacuum Science & Technology B: Microelectronics and Nanometer Structures Processing **22**, 1711 (2004).

[54] A. A. Tseng, K. Chen, C. D. Chen, and K. J. Ma, *Electron beam lithography in nanoscale fabrication: Recent development,* IEEE Transactions on Electronics Packaging Manufacturing **26**, 141 (2003).

[55] M. Altissimo, *E-beam lithography for micro-/nanofabrication,* Biomicrofluidics **4**, 026503 (2010).

[56] B. Bilenberg, S. Jacobsen, M. S. Schmidt, L. H. Skjolding, P. Shi, P. Bøggild, J. O. Tegenfeldt, and A. Kristensen, *High resolution 100 kV electron beam lithography in SU-8,* Microelectronic Engineering **83**, 1609 (2006).

[57] M. Madou, *Fundamentals of Microfabrication: The Science of Miniaturization, Second Edition* (CRC Press, Boca Raton, 2002).

[58] K. Wasa, M. Kitabatake, and H. Adachi, *3 - sputtering phenomena,* in *Thin Film Materials Technology*, edited by K. Wasa, M. Kitabatake, and H. Adachi (William Andrew Publishing, Norwich, NY, 2004) pp. 71 – 114.

[59] S. Somekh, *Introduction to ion and plasma etching,* Journal of Vacuum Science and Technology **13**, 1003 (1976).

[60] C. J. Mogab, A. C. Adams, and D. L. Flamm, *Plasma etching of Si and SiO2-The effect of oxygen additions to CF4 plasmas,* Journal of Applied Physics **49**, 3796 (1978).

[61] J. W. Coburn and H. F. Winters, *Plasma etching — a discussion of mechanisms,* Journal of Vacuum Science and Technology **16**, 391 (1979).

[62] J. W. Coburn and H. F. Winters, *Ion- and electron-assisted gas-surface chemistry - An important effect in plasma etching,* Journal of Applied Physics **50**, 3189 (1979).

[63] J. W. Coburn, H. F. Winters, and T. Chuang, *Ion- surface interactions in plasma etching,* Journal of Applied Physics **48**, 3532 (1977).

[64] D. L. Flamm, *Basic chemistry and mechanisms of plasma etching,* Journal of Vacuum Science & Technology B: Microelectronics and Nanometer Structures **1**, 23 (1983).

[65] S. Tachi, K. Tsujimoto, and S. Okudaira, *Low-temperature reactive ion etching and microwave plasma etching of silicon,* Applied Physics Letters **52**, 616 (1988).

[66] V. M. Donnelly and A. Kornblit, *Plasma etching: Yesterday, today, and tomorrow,* Journal of Vacuum Science & Technology A: Vacuum, Surfaces, and Films **31**, 050825 (2013).

[67] H. Akiya, K. Saito, and K. Kobayashi, *Sodium Contamination in SiO2 Films Induced by Plasma Ashing,* Japanese Journal of Applied Physics **20**, 647 (1981).

[68] *https://www.bruker.com/products/surface-and-dimensional-analysis/stylus-profilometers/dektak-xt/overview.html,* (accessed February 14, 2020).

[69] S. J. Randolph, J. D. Fowlkes, and P. D. Rack, *Focused electron-beam-induced etching of silicon dioxide,* Journal of Applied Physics **98**, 034902 (2005).

[70] C. W. Hagen, *The future of focused electron beam-induced processing,* Applied Physics A: Materials Science and Processing **117**, 1599 (2014).

[71] H. W. P. Koops, R. Weiel, and D. P. Kern, *High-resolution electron-beam-induced deposition,* Journal of Vacuum Science & Technology B: Microelectronics Processing and Phenomena **6**, 477 (1988).

[72] P. A. Crozier and C. W. Hagen, *High-Resolution Electron-Beam-Induced Deposition,* in *Nanofabrication* (World Scientific, 2008) pp. 399–430.

[73] W. F. Van Dorp, B. Van Someren, C. W. Hagen, P. Kruit, and P. A. Crozier, *Approaching the resolution limit of nanometer-scale electron beam-induced deposition,* Nano Letters **5**, 1303 (2005).

[74] I. Utke, P. Hoffmann, and J. Melngailis, *Gas-assisted focused electron beam and ion beam processing and fabrication,* Journal of Vacuum Science & Technology B: Microelectronics and Nanometer Structures Processing, Measurement, and Phenomena **26**, 1197 (2008).

[75] S. Goler, V. Piazza, S. Roddaro, V. Pellegrini, F. Beltram, and P. Pingue, *Self-assembly and electron-beam-induced direct etching of suspended graphene nanostructures,* Journal of Applied Physics **110**, 064308 (2011).

[76] C. Elbadawi, T. T. Tran, M. Kolibal, T. Nikola, J. Scott, Q. Cai, L. Li, T. Taniguchi, K. Watanabe, M. Toth, I. Aharonovich, and C. Lobo, *Electron beam directed etching of hexagonal boron nitride,* Nanoscale **8**, 16182 (2016).

[77] A. A. Martin and M. Toth, *Cryogenic Electron Beam Induced Chemical Etching,* ACS Applied Materials and Interfaces **6**, 18457 (2014).

[78] A. A. Martin, G. McCredie, and M. Toth, *Electron beam induced etching of carbon,* Applied Physics Letters **107**, 041603 (2015).

[79] C. J. Lobo, A. Martin, M. R. Phillips, and M. Toth, *Electron beam induced chemical dry etching and imaging in gaseous NH3 environments.* Nanotechnology **23**, 375302 (2012).

[80] T. Tao, J. Ro, J. Melngailis, Z. Xue, and H. D. Kaesz, *Focused ion beam induced deposition of platinum,* Journal of Vacuum Science & Technology B: Microelectronics Processing and Phenomena **8**, 1826 (1990).

[81] S. Lipp, L. Frey, G. Franz, E. Demm, S. Petersen, and H. Ryssel, *Local material removal by focused ion beam milling and etching,* Nuclear Instruments and Methods in Physics Research Section B: Beam Interactions with Materials and Atoms **106**, 630 (1995), ion Beam Modification of Materials.

[82] A. Botman, J. J. L. Mulders, R. Weemaes, and S. Mentink, *Purification of platinum and gold structures after electron-beam-induced deposition,* Nanotechnology **17**, 3779 (2006).

[83] C. Elbadawi, M. Toth, and C. J. Lobo, *Pure platinum nanostructures grown by electron beam induced deposition,* ACS Applied Materials and Interfaces **5**, 9372 (2013).

[84] H. Plank, J. H. Noh, J. D. Fowlkes, K. Lester, B. B. Lewis, and P. D. Rack, *Electron-Beam-Assisted Oxygen Purification at Low Temperatures for Electron-Beam-Induced Pt Deposits: Towards Pure and High-Fidelity*

Nanostructures, ACS Applied Materials & Interfaces **6**, 1018 (2014), pMID: 24377304.

[85] S. Mehendale, J. J. L. Mulders, and P. H. F. Trompenaars, *A new sequential EBID process for the creation of pure Pt structures from MeCpPtMe3.* Nanotechnology **24**, 145303 (2013).

[86] J. J. L. Mulders, *Purity and resistivity improvements for electron-beam-induced deposition of Pt,* Applied Physics A: Materials Science and Processing **117**, 1697 (2014).

[87] M. G. Stanford, B. B. Lewis, J. H. Noh, J. D. Fowlkes, and P. D. Rack, *Inert Gas Enhanced Laser-Assisted Purification of Platinum Electron-Beam-Induced Deposits,* ACS APPLIED MATERIALS & INTERFACES **7**, 19579 (2015).

[88] E. Villamor, F. Casanova, P. H. F. Trompenaars, and J. J. L. Mulders, *Embedded purification for electron beam induced Pt deposition using MeCpPtMe 3,* Nanotechnology **26**, 095303 (2015).

[89] A. Botman, *Towards high purity nanostructures from electron beam induced deposition of Platinum,* Ph.D. thesis, Delft University of Technology (2009).

[90] C. T. H. Heerkens, M. J. Kamerbeek, W. F. van Dorp, C. W. Hagen, and J. Hoekstra, *Electron beam induced deposited etch masks,* Microelectronic Engineering **86**, 961 (2009).

[91] I. G. C. Weppelman, P. C. Post, C. T. H. Heerkens, C. W. Hagen, and J. P. Hoogenboom, *Fabrication of narrow-gap nanostructures using electron-beam induced deposition etch masks,* Microelectronic Engineering **153**, 77 (2016).

[92] J. Hyon Noh, M. Nikiforov, S. V. Kalinin, A. A. Vertegel, and P. D. Rack, *Nanofabrication of insulated scanning probes for electromechanical imaging in liquid solutions,* Nanotechnology **21**, 365302 (2010).

[93] T. Liang, E. Frendberg, B. Lieberman, and A. Stivers, *Advanced photolithographic mask repair using electron beams,* Journal of Vacuum Science & Technology B: Microelectronics and Nanometer Structures **23**, 3101 (2005).

[94] M. Scotuzzi, *Electron Beam Technology for Single Nanometer Fabrication,* Ph.D. thesis, Delft University of Technology, Delft (2019).

[95] D. Klyachko, P. Rowntree, and L. Sanche, *Oxidation of hydrogen-passivated silicon surfaces induced by dissociative electron attachment to physisorbed H2O,* Surface Science **346**, L49 (1996).

[96] B. Carriére, A. Chouiyakh, and B. Lang, *AES study of the low-pressure oxidation of Si(100): Electron beam effects,* Surface Science **126**, 495 (1983).

3

IN-SITU HEATER IN SEM

3.1. INTRODUCTION

In this chapter, we will concentrate on the design, development and demonstration of an in-situ substrate heater in an SEM. As discussed in chapter 1, it may be used for partially cleaning the substrate, to remove adsorbed water, for purification of FEBID-fabricated structures and for thermal ALD. The heater was actually developed in two stages. In the first stage the focus was rather on compatibility with the electron microscope and on thermal stability than on its use for in-situ thermal ALD. A first prototype was built, and the lessons learned were used in the second development stage in which a new heater was constructed that can also be used for thermal ALD. Both heaters will be described in this chapter. The in-situ substrate heater needs to be used right under the pole piece and it should be placed on the SEM sample stage. This leads to several requirements and restrictions for the design, which will first be discussed.

3.2. REQUIREMENTS FOR IN-SITU SUBSTRATE HEATER

When we add the in-situ substrate heater to the SEM, it shouldn't affect the operation of the SEM. We should be able to use the SEM for FEBID depositions, imaging and dehydration baking of the substrate. This leads to several requirements for the design of the substrate heater. The requirements are,

1 The substrate heater should be easy to mount on the stage and adaptable to any SEM stage.

2 The stage should be thermally insulated from the substrate heater, to protect the delicate stage as well as to prevent heat loss from the substrate.

3 The pole piece and the detectors should be kept at their operating temperature (room temperature).

4 Keep the substrate position stable while varying the temperature.

5 Substrate size of 1 x 1 cm^2 wafer with a maximum thickness of 0.5 mm.

6 Temperature up to 150 ^oC, to carry out dehydration bake of substrates and for FEBID depositions.

7 The ramp-up time for the heater should be kept low, 15 minutes to reach the desired temperature.

8 The ramp-down time for the heater should be kept low, 15 minutes to reach room temperature.

9 No insulating materials should be visible near the substrate, to prevent charging while operating the SEM and imaging the substrate.

10 All materials used should be non-magnetic.

11 All materials used should be vacuum compatible and have a low outgassing rate.

12 The materials used should maintain their mechanical properties at the desired temperature (150^oC).

From the first requirement, we need to mount our heater on the stage. Typical SEM stages have an SEM stub which can be mounted on them. Consequently, the base of the heater should be similar to an SEM stub to mount it on the stage. Next, we need to make sure the substrate heater and the stage are thermally insulated to prevent damage of the stage. Also, we need to have an electrical contact between the substrate and the stage to avoid charging of the substrate. A Si chip has a coefficient of thermal expansion of 2.6 $10^{-6}/^oC$, so for 1 cm Si chip with a change of 100 ^oC, we would have a thermal expansion of 26 nm [1]. We do not want the feature we are imaging to move when we change the temperature. We normally use 10 x 10 mm^2 pieces of a 4 inch Si wafer for our experiments with a thickness of 0.5 mm. Hence, the heater should be able to accommodate such pieces. The distance between the substrate and the pole piece is normally kept at 5 mm, a photograph of the SEM chamber is shown in figure 3.1. In our Nova nanolab 650 SEM, the SEM stubs are mounted on an Al block, which is in turn mounted on the stage. A photograph of the Al block mounted on the stage is shown in figure 3.2. We use a custom built SEM stub with a thickness of 1 cm, which is mounted on the Al block. Our substrate heater should replace

this custom built SEM stub, so we need to keep the thickness of the substrate heater at 1 cm to keep the substrate - pole piece distance at 5 mm. The materials used should not lose their mechanical properties while using the substrate heater constantly at 150 ^{o}C. If the material is heated well above it's maximum allowable temperature, it may result in loss of stiffness of the material. The material will become soft and not be able to maintain it's shape during heating and cooling down of the heater. Hence we need to choose a suitable material housing the heater and the substrate, to withstand a temperature of 150 ^{o}C.

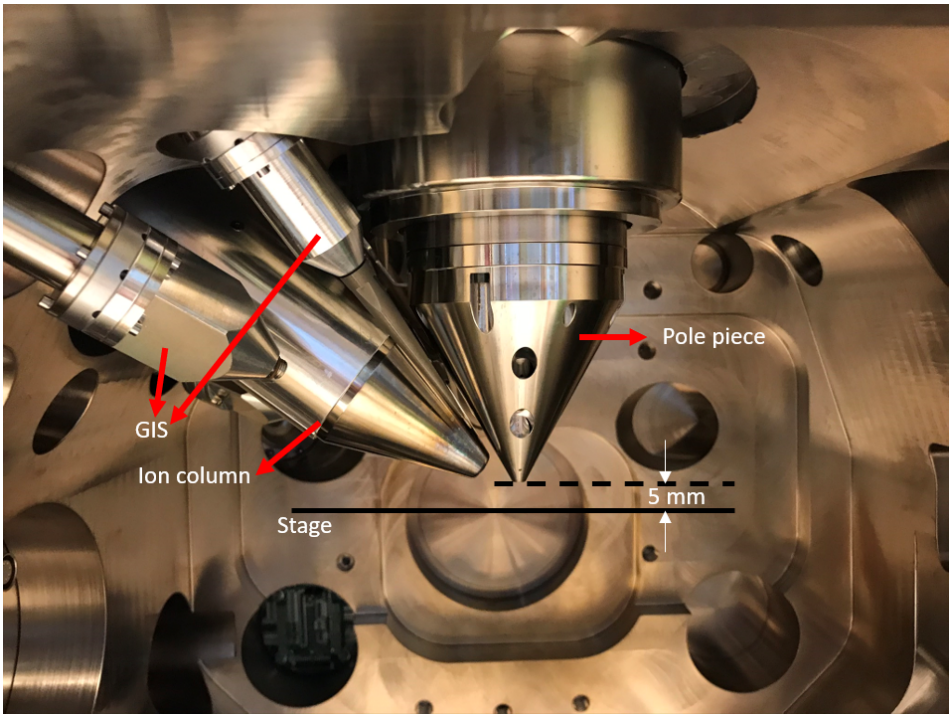

Figure 3.1: Photograph of the interior of the Nova nano SEM from the point of view of the chamber door.

3.3. DESIGN

First we need to decide on a heater which can heat the substrate to the required temperature of 150 ^{o}C. The power required to bring the substrate to a certain temperature is a combination of warm-up power and process power plus their associated losses [2][3]. Warm-up power is the power required to bring the substrate from room temperature to the desired temperature, plus the heat loss due to conduction and radiation. There is no loss due to convection as we operate in

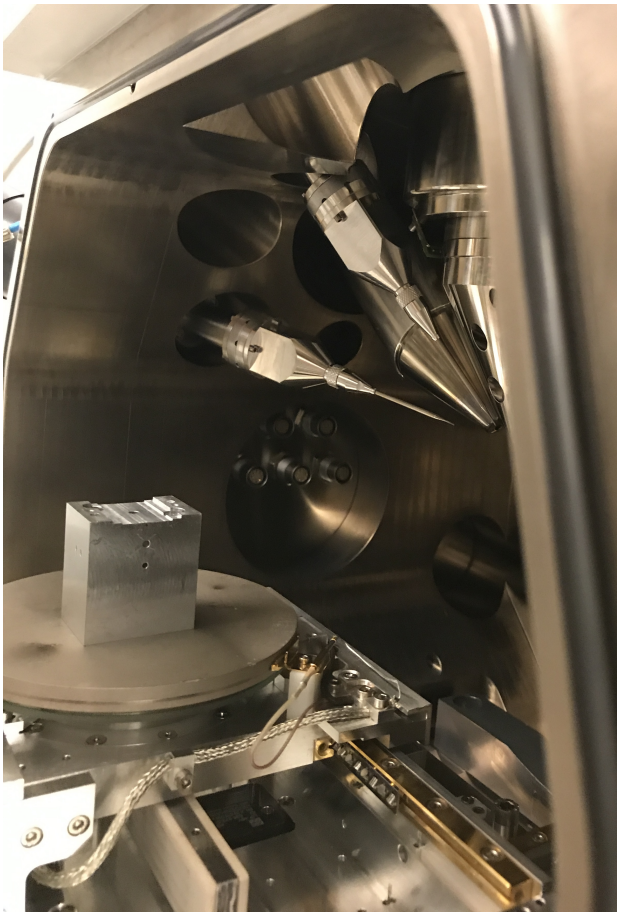

Figure 3.2: Photograph of the Al block which is mounted on the stage in the Nova nano SEM. chamber door.

vacuum. Process power is the power required to keep the substrate at a constant temperature plus the heat loss due to conduction and radiation. We can estimate the power required to heat a Si chip to 150 ^{o}C, using the following equation.

$$P = \frac{mc(T_f - T_i)}{t} \tag{3.1}$$

where P is the power required to bring the substrate to the desired temperature in W, m is the mass of the material in kg, c is the specific heat of the material in J/kg/K, T_f is the final temperature of the material in K, T_i is the initial temperature of the material in K and t is the time in seconds. The power loss due to conduction can be estimated by the following equation,

$$P_{cond} = \frac{\kappa.A(T_f - T_a)}{L} \tag{3.2}$$

where P_{cond} is the power loss due to conduction in W, κ is the thermal conductivity of the material in W/m.K, A is the area of the material in contact with an insulator or other material, T_a is the ambient temperature in K, T_f is the final temperature of the material in K and L is the thickness of material or the length of the conductive path in m. The power loss due to radiation can be estimated by the following equation,

$$P_{rad} = \sigma\epsilon A(T_f^4 - T_a^4) \tag{3.3}$$

where P_{rad} is the power loss due to radiation in W, ϵ is the emissivity of the material, σ = 5.6710^{-8} W/m^{2}K^4 is the Stefan-Boltzmann constant and A is the surface area of the material in m^2.

For a Si chip of 10 x 10 mm^2 with a thickness of 0.5 mm, a heating time of 600 s and material parameters found in table 3.1, we can estimate from equation 3.1 the power required to heat the chip to 150 ^{o}C to be 0.02 W. Similarly from equation 3.2 we can estimate the power loss due to conduction to be 6.5 W (assuming a contact area of 100 mm^2 and in contact with PEEK), if we assume the whole chip to be in contact with the insulating material (eg., PEEK) with an ambient temperature of 20 ^{o}C. From equation 3.3, the power loss due to radiation is 0.1 W. So, the total power required is 6.62 watts. Hence, we need to look for a heater which can meet the power requirement of 6.62 W. We found a commercially available Pt based heater which is compatible for use in vacuum, small in size (2 x 10 mm^2) and with a maximum power of 27 W [15]. This Pt heater, shown in figure 3.3 can be mounted underneath the Si chip.

The Pt heater should be fixed onto a metal block (heater block) on top of which the substrate should be mounted. Aluminum has a high specific heat and thermal conductivity compared to Stainless steel, as seen in table 3.1 and can be used as the material for the metal block. Hence, it will require a lower power to heat the heater block to the desired temperature and have a better thermal conduction to the substrate resulting in a faster heater time. The heater block should be isolated from the stage to prevent loss of heat to the stage. If we assume a heater block made of Al with a dimension of 14 x 14 mm^2 and a thickness of 2.5 mm, the power required to heat up the heater block is 0.25 W, the power loss due to conduction is 2.12 W and the power loss due to radiation is 0.04. The total power required for heating the heater block to 150 ^{o}C is 2.41 W, which is well within the limits of the Pt heater. Also, the maximum serviceable temperature of Al is within the maximum temperature requirement of the substrate heater. If

Table 3.1: Material properties of some commonly used materials in high vacuum

Material	Density (g/cm^3)	Specific heat, c(J/g^{o}C)	Thermal conductivity, κ (W/m.K)	Co-efficient of Thermal expansion (10^{-6}/^{o}C)	Maximum service temperature (^{o}C)	emissivity
Si [1]	2.32	0.71	152	2.6	1350	0.71
Aluminum (6082 - T6) [4] [5]	2.7	0.88	250	23	170	0.08-0.16 [1]
Stainless steel (316 1.4401)[6]	8	0.5	16.3	16.2	870	0.17
Titanium (Ti6Al4V Grade 5) [7][8]	4.43	0.565	6.6	9.5	400	0.7
Titanium (Grade 2) [7]	4.51	0.52	20.8	9.2	400	0.3
PEEK	1.3 - 1.5	1.34	0.25	0.5	260	0.95
PTFE [9][10]	2.13 - 2.23	1	0.25	100	260	0.92
AlOx [11] [10]	3.9	0.88	30	7.6	1700	0.8
Macor [12] [13]	2.52	0.79	1.46	9	800	0.87
Glass [14]	2.5	0.72	1	9	514	0.84

1 The emissivity value depends on the way the material was machined[5]

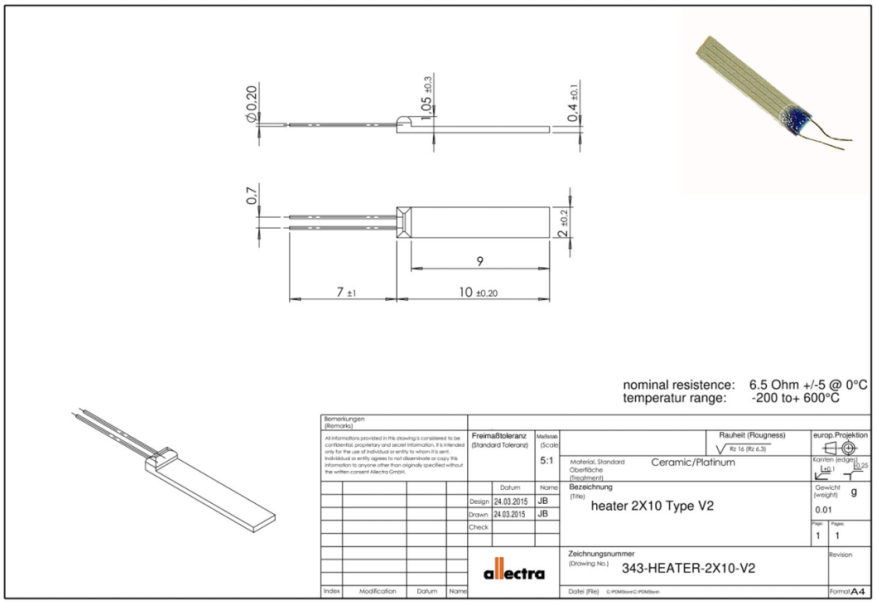

Figure 3.3: Drawings of the Pt heater from Allectra (Units in mm). Photograph of the Pt heater is shown in the inset picture.

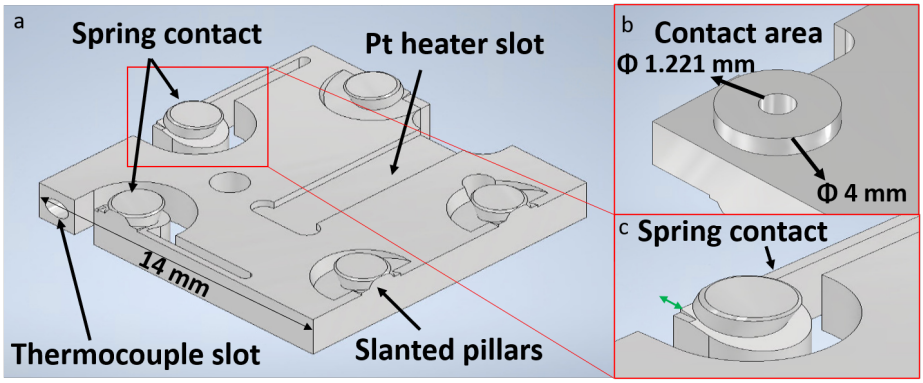

Figure 3.4: a) CAD drawing of the heater block made of Al (6082 - T6) showing the different parts of the block along with two spring contacts which allow for the thermal expansion of the substrate. b) CAD drawing showing the bottom of the heater block with the single contact area, which makes a contact with the isolator block providing thermal isolation. c) Zoom-in of the spring contact, which can be moved as indicated by the green arrow is used to mount the Si chip of 10 x 10 mm^2.

we reduce the surface area of the heater block in contact with the thermal isolator, which has not been discussed yet, to a size of 5 x 5 mm^2, we can reduce

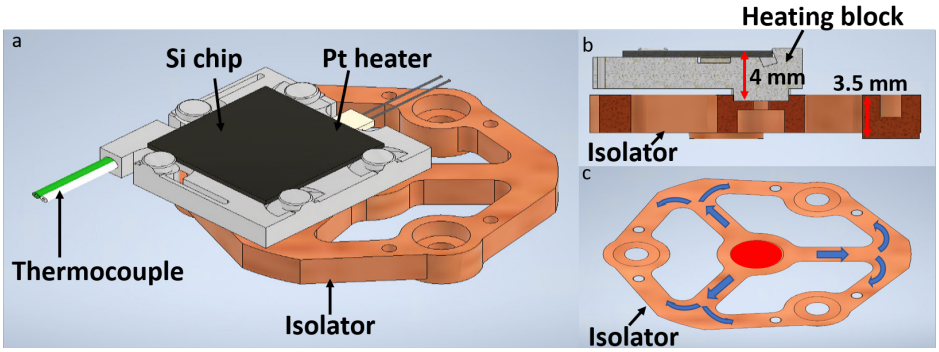

Figure 3.5: a) CAD drawing depicting the Si chip sitting on top of the heater block which is mounted on top of the isolator block providing thermal insulation. b) Cross-section image of the heater block and the isolator block. c) Top down view of the isolator block, the blue arrows depict the heat flow direction from the heater block element. Red circle depicts the region where the heater block element makes contact with the isolator block.

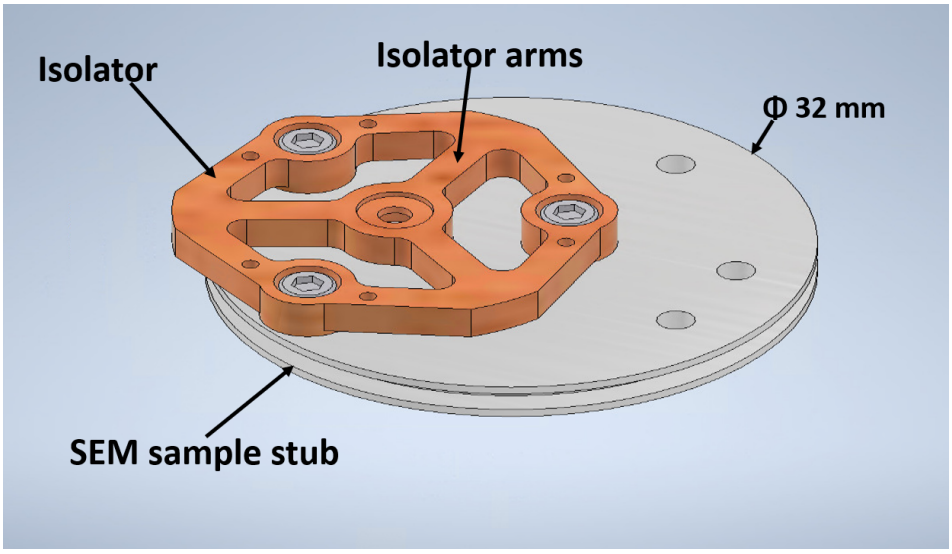

Figure 3.6: CAD drawing showing the isolator block mounted (using 3 M1.6 screws) on top of a standard SEM stub with a diameter of 32 mm and a pin diameter of 3.2 mm which fits on Thermo Fisher Scientific (formerly FEI), ZEISS and TESCAN SEM instruments.

the conduction loss to 0.27 W. This brings the total power required to heat up the heater block to 0.56 W, hence we should try to reduce the contact surface area to limit the power loss due to conduction. Figure 3.4 shows the CAD drawing of the heater block. It has a slot to accommodate the Pt heater as well as a slot to mea-

sure the temperature of the heater block directly using a thermocouple. Figure 3.4 b, shows the contact area (from the bottom side of the heater block) which makes contact with the isolator block. It has a surface area of 23.96 mm^2 and a height of 4 mm from the contact point to the Si chip. This results in a conduction loss of 0.19 W. The heater block is mounted on the isolator block by means of a push fit connection. The heater block has 5 slanted pillars which are used to hold the Si chip (size of 10 x 10 mm) in place. Two of the slanted pillars are flexible spring contacts which are used to mount the Si chip, shown in figure 3.5 c. The slanted pillars allow the Si chip to be tilted during operation of the heater. Figure 3.5 a, shows the heater block mounted on the isolator block with the various components. The cross-section of the heater block and the isolator block with the push fit connection is shown in figure 3.5 b. The isolator block is designed to minimize displacement due to thermal expansion. The isolator block is made out of PEEK as the specific heat capacity, thermal conductivity and the thermal expansion coefficient are low. Moreover, it is easy to machine it to the desired shape and the maximum serviceable temperature is 260 ^oC, which is well above the temperature requirement.

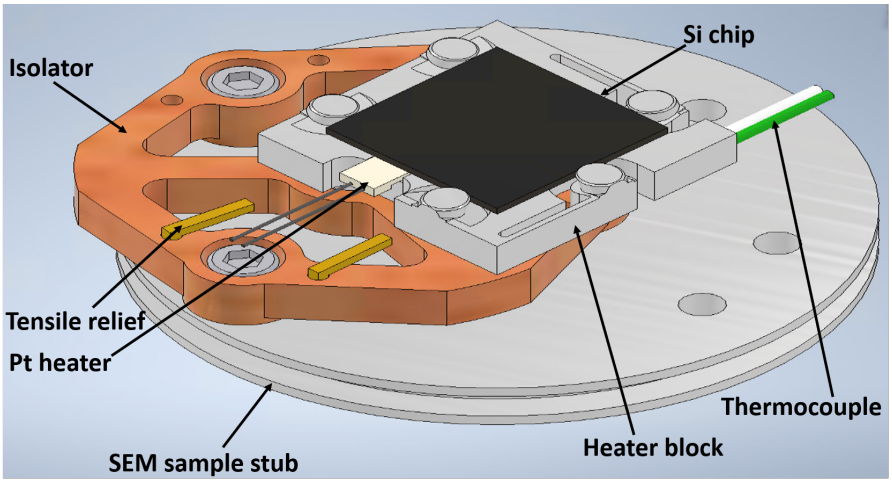

Figure 3.7: CAD drawing of the in-situ substrate heater showing the various components.

The isolator block is mounted on to an SEM stub (diameter of 32 mm and a pin diameter of 3.2 mm) as shown in Figure 3.6 by using 3 M1.6 screws. The SEM stub can be mounted in most of the commercially available SEM instruments from Thermo Fisher Scientific (formerly FEI), ZEISS and TESCAN. Figure 3.7 shows the complete in-situ substrate heater assembly. It includes two tensile relief connectors which are used to electrically connect the Pt heater. The two

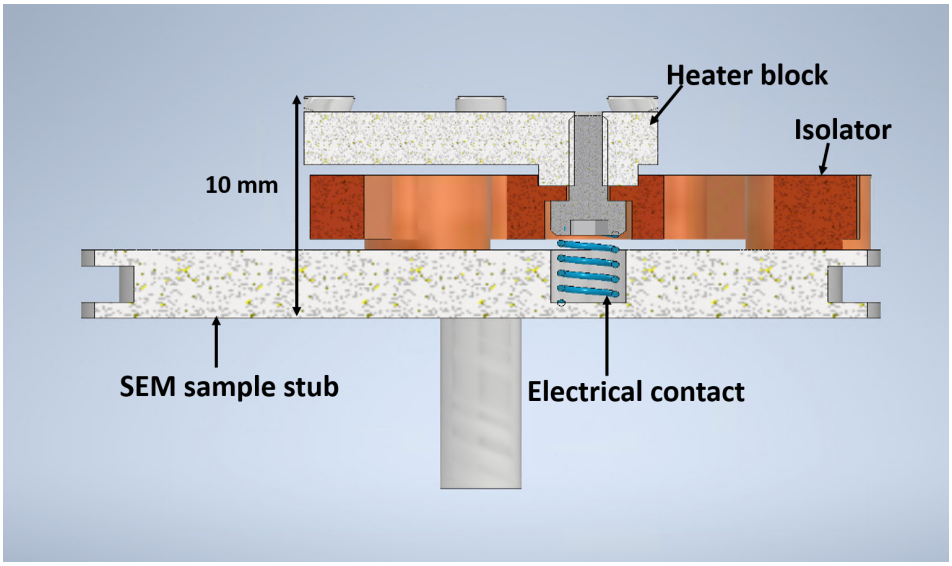

Figure 3.8: Cross-sectional CAD drawing of the in-situ substrate heater, showing the electrical contact (using a spring) between the SEM stub and the heater block.

tensile relief connectors are mounted on the isolator block by means of a push fit. A cross-section image of the whole in-situ substrate heater assembly is shown in figure 3.8. The heater block containing the Si chip needs to be electrically connected to the stage through the SEM stage to avoid charging of the substrate. This is done by using a spring made out of Phosphor Bronze, as it is non-magnetic and vacuum compatible. The spring is in contact with a M1.6 screw which is fixed to the bottom of the heater block. The total height of the in-situ substrate heater is 10 mm (shown in figure 3.8). Figure 3.9 shows an ANSYS directional deformation simulation of the material while heating the heater block to 150 ^{o}C, in the center of the Si chip there is a displacement of 2 μm. Maximum deformation is observed in two of the corners of the heater block with a value of 17.7 μm and -34.4 μm. Also maximum deformation is observed in the isolator block arms (red coloured region in figure 3.9). Along the Y-axis (shown in figure 3.10), we observe a deformation of 13.5 μm, this mainly arises from the different thermal conductivity of Al and the Si chip. Figure 3.11 shows the ANSYS steady state thermal simulation of the in-situ substrate heater, when the heater block is heated to 150 ^{o}C. In a steady state thermal simulation, the thermal loads do not vary with time. The SEM stub remains at room temperature, while the isolator block thermally insulates the heater block and the SEM stub. The temperature variation in the isolator block can also be seen in figure 3.11, with a higher temperature in the arms of the isolator block.

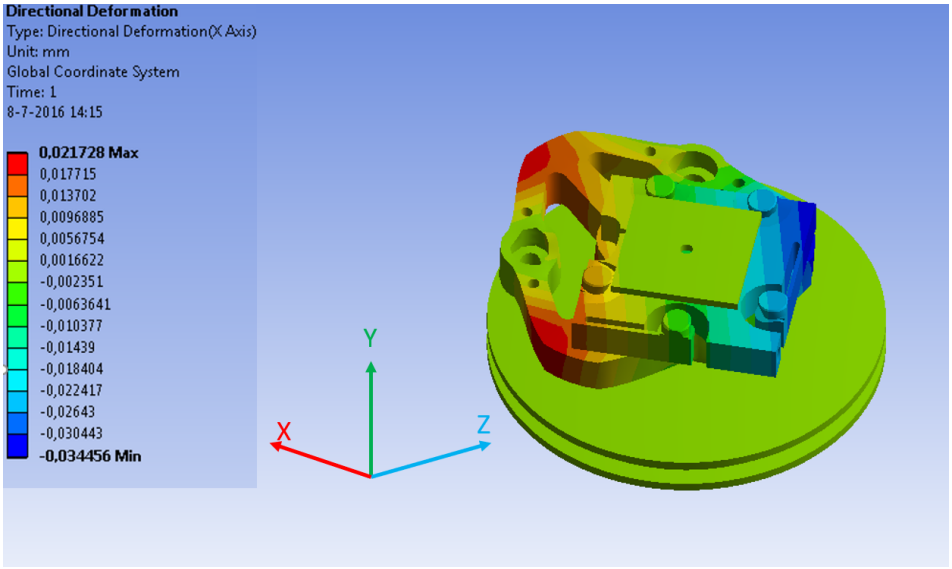

Figure 3.9: ANSYS simulation of the in-situ substrate heater assembly to estimate the deformation in X-axis while heating the heater block to 150 ^{o}C. The corners of the heater block experience a maximum deformation of 17.7 μm and -34.4 μm. Image courtesy of Ruud van Tol.

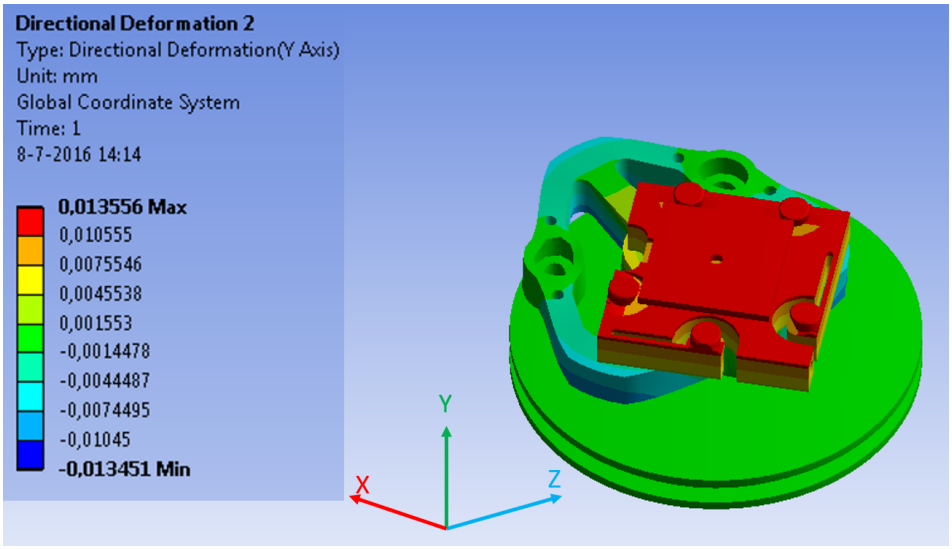

Figure 3.10: ANSYS simulation of the in-situ substrate heater assembly to estimate the deformation in Y-axis while heating the heater block to 150 ^{o}C. The height of the Si chip changes by 13.5 μm. Image courtesy of Ruud van Tol.

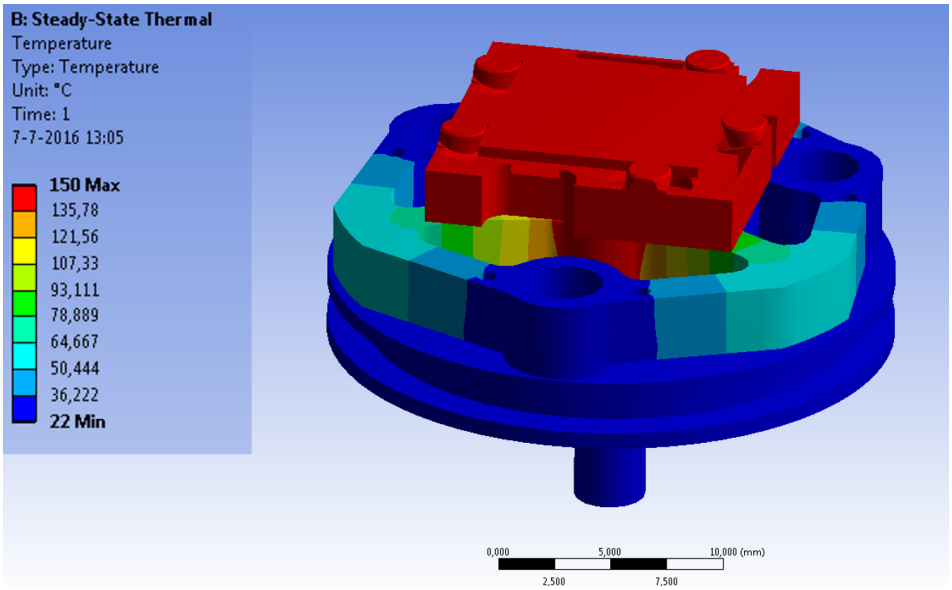

Figure 3.11: ANSYS steady state thermal simulation of the in-situ substrate heater assembly. The heater block along with the Si chip is kept at a temperature of 150 ^{o}C (depicted in red), the heat flow in the isolator block section can also be seen, while the SEM stub is kept at 22 ^{o}C. Image courtesy of Ruud van Tol.

Finally, we need to check whether a heat shield is required to block the power radiated to the stage and other parts present in the SEM chamber. From the CAD drawing, the side of the heater block facing the SEM stub has a surface area of 157.69 mm^2. The power loss due to radiation as calculated from equation 3.3 is 0.035 W, so little power is radiated towards the SEM stub. Moreover, the isolator block covers a part of the heater block, so the actual radiated power would be lower. Hence, we don't require a heat shield to protect the SEM stub. The total surface area of the heater block element facing the pole piece is 44.24 mm^2. The power loss due to radiation as determined from equation 3.3 is 0.01 W, choosing an emissivity of 0.16, which is the highest value from table 3.1. We also have the Si chip (10 x 10 mm^2) which radiates power to the surroundings, the power radiated from the Si chip is 0.099 W resulting in a total power of 0.1 W being radiated to the surroundings. We can estimate the temperature increase of the pole piece made of mu metal (c = 490 J/kg.^{o}C, density of 8.747.10^{-3} kg/cm^3) and from the CAD drawing of the pole piece we can estimate the mass to be 0.73 kg [16]. Using equation 3.1 with a power of 0.1 W, we obtain a temperature of 21 ^{o}C after 1 hour. Hence, we don't need any heat shield on top of the heater to protect the pole piece and the detectors.

3.4. FABRICATION AND ASSEMBLY

We chose a Pt heater as discussed in the previous section to meet the power requirements. The heater block is made out of Al (6082 T6) and is machined to the desired dimensions. We used a commercially available K-type thermocouple to accurately measure the temperature of the heater block [17]. The isolator block is made out of PEEK as previously discussed and machined to the desired dimensions. We bought a standard SEM stub from Agar scientific with a diameter of 32 mm and a pin diameter of 3.2 mm [18]. Afterwards, the SEM stub was machined to make the threaded M1.6 screw holes to mount the isolator block onto the stub. For the tensile relief, we used 2 individual pins from commercially available L-shaped pin headers made out of a copper alloy and gold plated [19]. For the electrical connection to supply power to the Pt heater we used a PTFE coated wire. The metallic components (heater block, SEM stub, tensile relief pin connectors, spring and the various screws) were cleaned ultrasonically in a beaker containing acetone for 2 hours followed by cleaning ultrasonically in a beaker containing ethanol for 2 hours. Finally, the components were blown dry by using Nitrogen gas. The non-metallic parts (isolator block, Pt heater, K-type thermocouple and the connecting wires were cleaned ultrasonically in a beaker containing ethanol for 2 hours followed by blow drying them in Nitrogen gas.

We used a commercially available PELCO high temperature carbon paste to glue the the Pt heater to the heater block [20]. We decided to use this glue as it can withstand a temperature upto 2000 ^{o}C, which is well above our temperature requirements. Moreover, the glue is soluble in water making it easy to remove the Pt heater in case of breakage. We first applied the carbon paste on the Pt heater slot in the heater block component. The Pt heater was then gently pressed on to the heater block and left in air for 2 hours to cure it. Then, the heater block was baked in a vacuum oven at 90 ^{o}C for 2 hours followed by a further curing of the carbon paste in the vacuum oven at 180 ^{o}C for 2 more hours. The in-situ substrate heater was assembled according to the CAD drawings. The Pt heater leads were soldered (by a vacuum compatible solder) to the PTFE wires. The Pt heater is supplied by a power supply from Delta Elektronika ES030-5 (maximum 30V and maximum current 5A) unit [21]. The power supply leads and the thermocouple in the vacuum are connected to the outside world through an electrical feedthrough.

3.5. PERFORMANCE TESTS

The in-situ substrate heater was assembled and mounted in the SEM for initial tests. During the ramp-up of the substrate heater, the substrate was heated above 170 ^{o}C due to a faulty temperature measurement setup. This caused the soften-

ing of the Al block which led to permanent deformation of the spring contacts. This required a new clip made of Phosphor Bronze (copper color) to be placed over the spring contact and the substrate as shown in figure 3.12. This clip is needed to keep the contact spring in place.

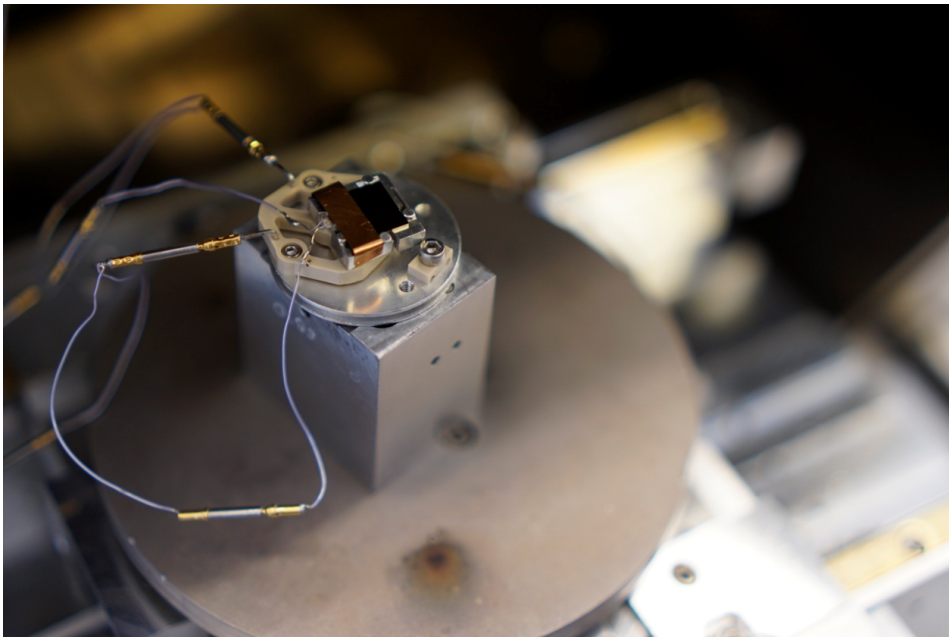

Figure 3.12: Photograph of the in-situ substrate heater mounted on the SEM stage showing the electrical connections to the Pt heater. Also seen is a piece of Phosphor bronze (copper color piece on top of the heater block) which is used to hold the flexible spring contact in place (to limit thermal drift during ramp-up) after we used the heater at a temperature higher than 170 ^{o}C resulting in the heater block (Al 6082 T6) becoming soft.

We manually control the power of the Pt heater, by changing the voltage of the power source to reach 100 ^{o}C. Figure 3.13 shows the ramp-up of the substrate heater to a temperature of 100 ^{o}C. We are able to heat the substrate to the desired temperature (100 ^{o}C) in less than 9 minutes, that gives us a ramp-up rate of 8.2 ^{o}C/min. So, by heating the substrate for 15 minutes we will be able to reach approximately 150 ^{o}C.

Figure 3.14 shows the ramp-down of the substrate heater after it is heated to a temperature of 150 ^{o}C. The temperature data were manually noted down at 10 minute intervals. It takes more than 40 minutes to bring the substrate below 30 ^{o}C. This results in a ramp-down rate of 3 ^{o}C/min. This is well beyond our ramp-down requirement. This is because the heater is used at pressures of 10^{-6} to 10^{-5} mbar. So, there are few gas molecules present in the chamber. Therefore, con-

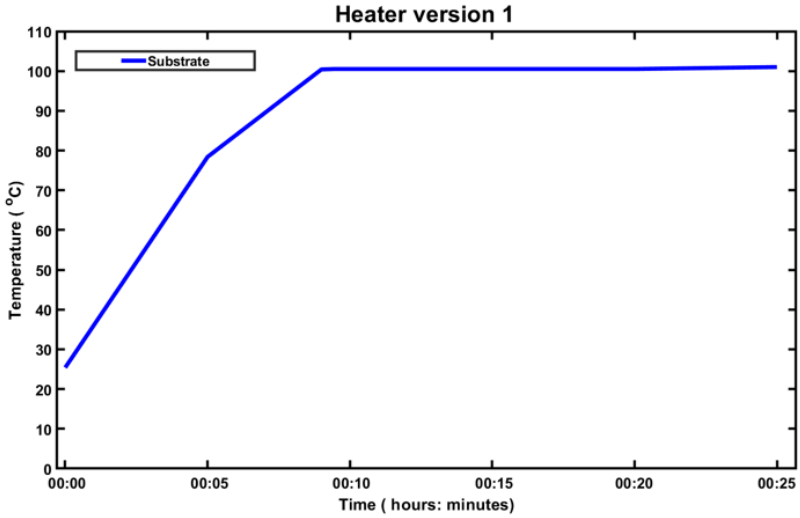

Figure 3.13: Graph showing the ramp-up of the substrate temperature from room temperature to 100 ^{o}C manually measured in steps of 5 minutes. We are able to ramp-up the substrate to the desired temperature in 9 minutes.

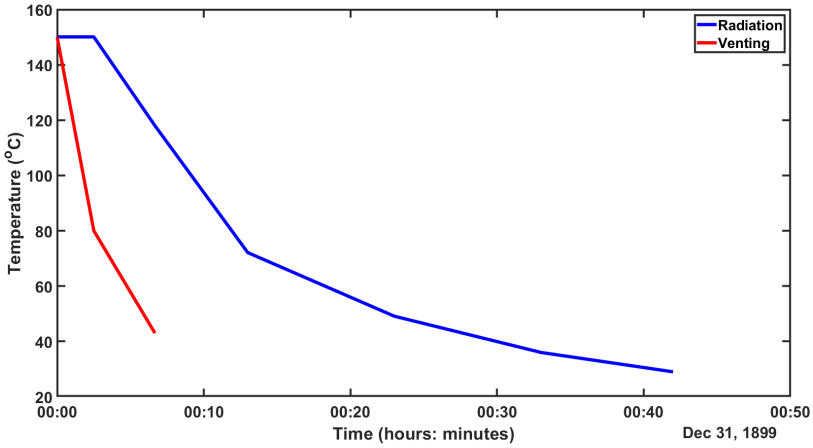

Figure 3.14: Graph showing the ramp-down of the measured temperature of the substrate, when the power to the Pt heater is switched off. Cooling by radiation is indicated by the blue curve, forced cooling by venting for 2 minutes and 30 seconds followed by pump down is indicated by the red curve. With radiation alone it takes about 40 minutes to bring the substrate under 30 ^{o}C, whereas with the chamber vent plus chamber pump procedure it takes 6 minutes and 40 seconds to reach 40 ^{o}C.

duction and radiation are the only mechanisms behind heat transfer. Moreover, to protect the stage from heating we have thermally isolated the sample holder containing the substrate from the stage. Due to this, we are left with radiation as the only mechanism behind heat transfer. To cool down the substrate, we decided to vent the chamber and then pump the chamber after 2 minutes and 30 seconds so that the chamber is not fully vented. It takes about 3 minutes to completely vent the chamber in our Nova Nano SEM. After the chamber reaches high vacuum pressure ($< 9\ 10^{-5}$), the substrate is at 40 ^{o}C in 6 minutes and 40 seconds. This results in a ramp-down rate of 16 ^{o}C/min. This chamber vent plus chamber pump cycle should be repeated to bring the substrate to room temperature if any processing is to be done after the high temperature processing. To test the drift at a constant temperature, we heated the substrate to 200 ^{o}C and exposed the Si chip to an e-beam without any precursors present. We increased the temperature of the substrate to 200 ^{o}C, as we already went past the heater block temperature limit of 170 ^{o}C during our previous tests with the faulty temperature measurement. The scan parameters used during the e-beam exposure were 20 kV, 0.62 nA, 150 x 150 nm^2 and a dose of 5.58 μC/μm^2. Figure 3.15 shows the contrast adjusted secondary electron (SE) image of the Si chip with the exposed region indicated by a red square. We can observe a low C deposition and we don't observe any deviation in the shape of the structure. Moreover, we kept the beam on and imaged the exposed area for 10 minutes. During imaging, we observed no noticeable drift, so we don't observe any drift during imaging nor during the exposure of the pattern.

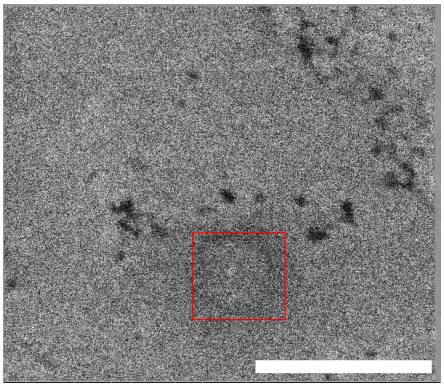

Figure 3.15: Contrast adjusted secondary electron (SE) image of a Si chip which is exposed to the e-beam of 20 kV, 0.62 nA, 150 x 150 nm^2, dose of 5.58 μC/μm^2. The substrate was kept at a temperature of 200 ^{o}C, and we can observe carbon deposition (red square) on the sample. The scale bar is 500 nm.

3.6. SUMMARY

To summarize, in the previous sections we listed the different requirements and restrictions for building an in-situ substrate heater to be used in an SEM. We set a temperature limit of 150 ^{o}C during the design phase of the heater, but due to a faulty temperature measurement in the first run we went well above the temperature limit. This led to the heater block component of the substrate heater to become soft. This led to the spring contacts to expand beyond their limit, which is why we used a clip made out of Phosphor Bronze to hold the spring contact in place. The ultimate temperature limit of this heater is now 260 ^{o}C, being the temperature limit of the isolator block which is made out of PEEK. We measured a ramp-up rate of 8.2 ^{o}C/min and a ramp-down rate of 16 ^{o}C/min when we used the chamber vent plus chamber pump method to cool down the heater. We were also able to carry out a patterned exposure on a Si chip at a constant temperature of 200 ^{o}C and imaged the sample for 10 minutes without any noticeable drift. With the lessons learnt in this version of the substrate heater, an improved design is made for a heater which can reach upto 300 ^{o}C for carrying out thermal ALD.

3.7. REQUIREMENTS FOR HEATER VERSION 2

The previously designed heater (referred to as heater V1) is not suitable for ALD applications due to its limited maximum usable temperature. The Pt ALD process requires a temperature of 300 ^{o}C, while heater V1 can only safely operate up to 260 ^{o}C due to deformed spring contacts. Therefore, it is necessary to design and fabricate a new in-situ substrate heater (referred to as heater V2) capable of reaching temperatures up to 300 ^{o}C. It is important to ensure that integrating heater V2 into the SEM does not interfere with the operation of the SEM itself, allowing for continued functionality in FEBID, SEM imaging, and ALD processes. The requirements for the new heater remain similar to those of heater V1, with the exception of an increased maximum temperature of 300 ^{o}C. Additionally, the requirement for maintaining substrate position stability while varying the temperature can be relaxed to allow for more flexibility.

And the materials used should not lose their mechanical properties while using the substrate heater constantly at 300 ^{o}C. Hence we need to choose a capable material housing the heater and the substrate, to withstand a temperature of 300 ^{o}C. The discussion for all other requirements are the same as for the heater V1.

3.8. DESIGN

We already have a Pt heater element which can go upto a temperature of 600^{o}C. But a suitable material has to be chosen for the heater block to allow for temperatures up to 300 ^{o}C. Al loses it's mechanical properties at 170^{o}C. Hence we need to look at other metals to make the heater block. If we assume a similar geometry (14x14 mm^2 and 2.5 mm in height) as in heater V1, then from equation 3.1 we would require a power of 0.29 W, 0.27 W and 0.46 W if the heater block is made out of Ti Grade 5, Ti Grade 2 and Stainless Steel respectively. Hence, we can use the already existing Pt heater for heating the heater block and the substrate. The heater block needs to have a high tensile strength as we heat it up to a temperature of 300 ^{o}C, Such that it can withstand the expansion and contraction during ramp-up and ramp-down without breaking down. The tensile strength's of Ti Grade 5, Ti Grade 2 and stainless steel are 641 MPa, 103 MPa and 165 MPa respectively at around 300 ^{o} C[22][7]. Ti Grade 5 has the highest tensile strength at the desired operating temperature of 300 ^{o}C. Hence, the heater block is chosen to be made out of Ti Grade 5. The heater block along with the various components is shown in figure 3.16 a. Figure 3.16b shows the bottom side of the heater block along with the slots for the spring contact and the slots to mount the heater block on the isolator block. The power required to heat the heater block to 300 ^{o}C in 20 minutes is 0.663 W, from equation 3.1 using a mass of 0.005 kg which can be calculated from table 3.1. Also, the plate with clamping spring used to fix the Si chip on top of the heater block is shown in figure 3.17. The plate with springs has 3 holes with a diameter of 1.8 mm to fix it to the heater block.

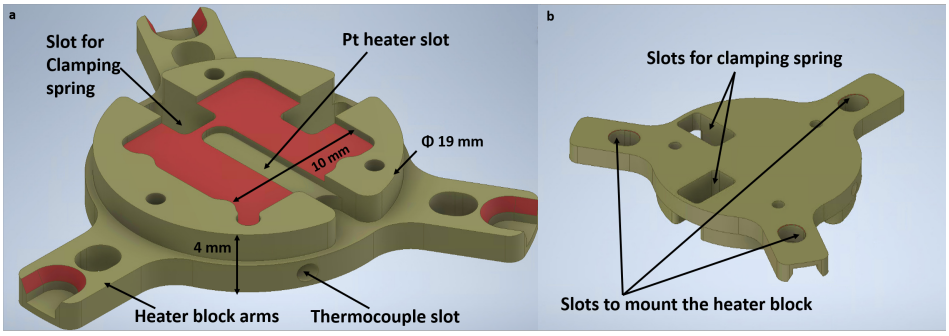

Figure 3.16: a) CAD drawing depicting the heater block having a slot for the Pt heater, two slots for clamping springs and a slot for a thermocouple to measure the temperature of the heater block. Red color is used to give a better contrast. b) Bottom side view of the heater block showing the slot for the clamping springs and slots where the heater block will be resting on the isolator block.

Next, we need to thermally isolate the heater block and the SEM stub. In the heater V1 we used an isolator block to achieve this. PEEK and PTFE can't be used

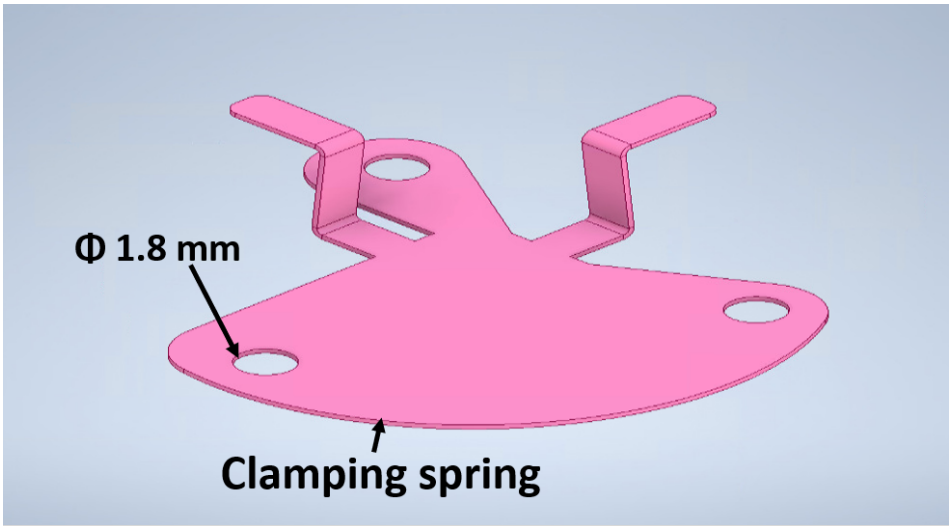

Figure 3.17: a) CAD drawing of the plate with clamping spring used to mount the Si chip of 10 x 10 mm^2. It has 3 holes with diameter of 1.8 mm to fix it to the heater block.

at 300 ^{o}C. Glass and MACOR can be used at this temperature, but glass has a lower thermal conductivity (1 W/m.K) as compared to MACOR (1.6 W/m.K). Also the coefficient of thermal expansion of Ti and glass are closely matched. Hence, we decided to use glass as the material for the isolator block. If we assume a design similar to heater V1 with a contact surface area of 23.96 mm^2, the power loss due to conduction is 1.68 W as calculated from equation 3.2. The power loss due to conduction is 2.5 times higher than the power required to heat up the heater block. We can't use the design from heater V1.The solution found was to use glass balls to isolate the heater block from the SEM stub, to minimize the contact area and minimize the power loss due to conduction. Figure 3.18 shows the ANSYS steady state thermal simulation for the case where a hot cylindrical block is kept at 300 ^{o}C and is isolated from an SEM stub using a glass ball of 3 mm diameter. A 3 mm glass ball is used to keep the total height of the heater within specifications. In this case, the SEM stub raises to a temperature of 53 ^{o}C.

Figure 3.19 shows the ANSYS steady state thermal simulation for the case where a hot cylindrical block is kept at 300 ^{o}C and is isolated from an SEM stub using 4 glass balls in a tetrahedron configuration [23]. In the case of 4 glass balls in tetrahedron configuration, the SEM stub stays at 22 ^{o}C. The steady state thermal simulation of just the 4 glass balls is shown in figure 3.20 a, and the equivalent electrical circuit for the 4 glass balls setup is shown in figure 3.20 b. Here, R_{GB} is the thermal resistance of the glass ball, in the tetrahedron configuration the total thermal resistance is equal to $\frac{4}{3}$ R_{GB}. The contact resistance

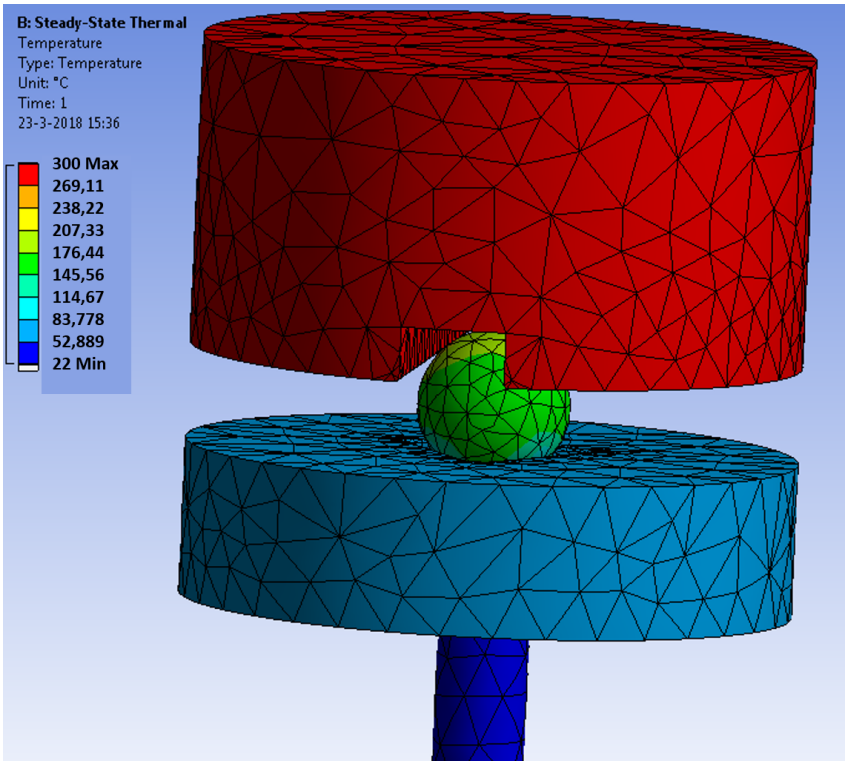

Figure 3.18: a) ANSYS steady state thermal simulation depicting the estimated temperature of the SEM stub, while keeping the heater block (here a cylindrical block) at a temperature of 300 ^{o}C. In this case, we used a single glass ball to thermally insulate the SEM stub. The SEM stub raises to a temperature of 53 ^{o}C. Image courtesy of Ruud van Tol.

between the pedestal stub and glass balls is ignored, along with the contact resistance between the glass ball and the heater block in the equivalent electrical circuit shown in figure 3.20 b. The tetrahedron configuration helps in keeping the pedestal stub at room temperature, this is due to the reduction in the total surface area in contact with the heater block as well as the pedestal block and increase in the conduction path. This results in lower power loss due to conduction.

To mount the heater block, 3 tetrahedron configurations are required to balance the heater block on an SEM stub. Therefore, we can't use an existing SEM stub. Hence we decided to make a custom SEM stub (hereafter pedestal stub) with sockets to hold the glass balls in place. Figure 3.21 a, shows the pedestal stub with sockets for holding the glass balls in place. It has 3 sockets to balance the heater block properly. Figure 3.21 b, shows the pedestal stub alone with a

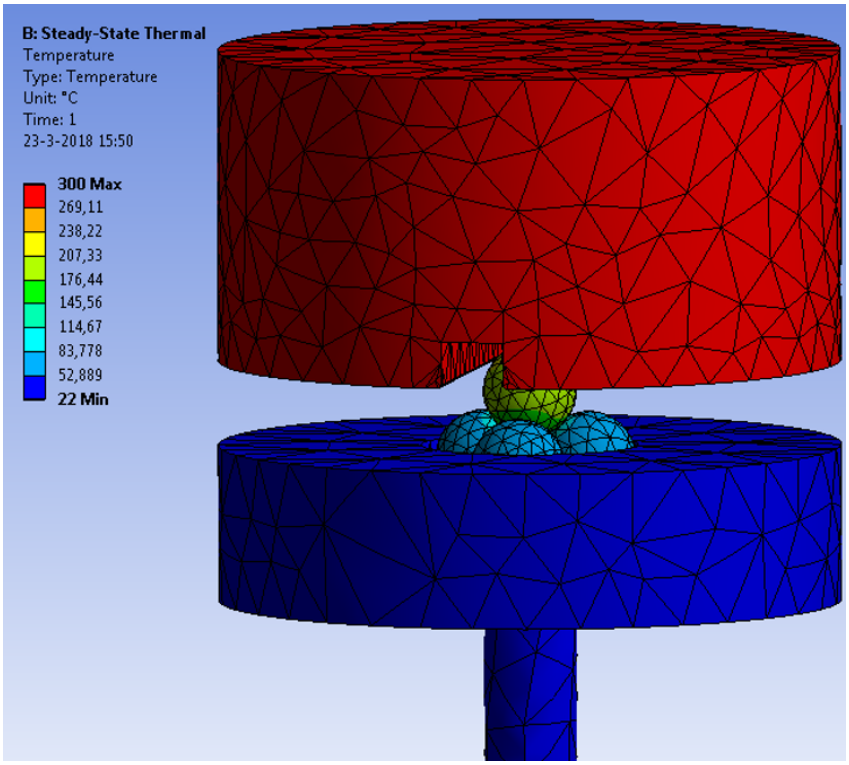

Figure 3.19: a) ANSYS steady state thermal simulation depicting the estimated temperature of the SEM stub, while keeping the heater block (here a cylindrical block) at a temperature of 300 ^{o}C. In this case, we used a 4 glass balls arranged in a tetrahedron configuration to thermally insulate the SEM stub and it keeps the stub at room temperature. Image courtesy of Ruud van Tol.

diameter of 38 mm and the pin has a diameter of 3.2 mm. The 4 glass balls in the tetrahedron configuration are shown in figure 3.21 c. The height of the substrate heater with the heater block mounted on the pedestal stub through the glass balls is 11.5 mm (shown in figure 3.22), this height is 1.5 mm greater than the height of the heater V1. This increase in height of 1.5 mm of the substrate heater can be accommodated by lowering the stage. Figure 3.23 shows the substrate heater with a Si chip (10 x 10 mm^2) along with it's various components. Now, the heater block is mounted on the pedestal stub without any clamping mechanism to stop it's movement. So, we need to hold the heater block in a fixed position. This is done by using 3 clamps along the arms of the heater block. The clamps should not make a direct contact with the heater block, as it will lead to a power loss due to conduction through the clamps. Hence, we decided to use a glass ball between the clamps and the heater block element. The CAD drawing of the clamps

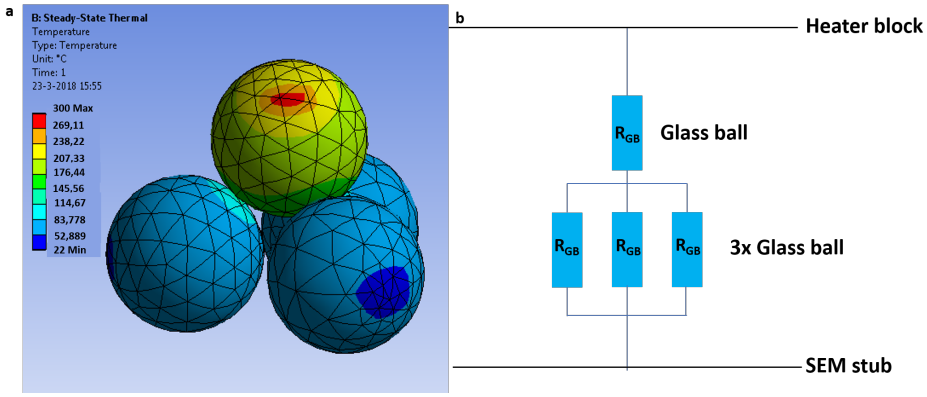

Figure 3.20: a) Close-up of the ANSYS steady state thermal simulation shown in figure 3.19 of the heat flow in the 4 glass balls arranged in tetrahedron configuration. Image courtesy of Ruud van Tol. b) Electrical equivalent circuit of the the 4 glass balls, R_{GB} is the thermal resistance of one glass ball. The contact resistance between the pedestal stub and glass balls is ignored, along with the contact resistance between the glass ball and the heater block.

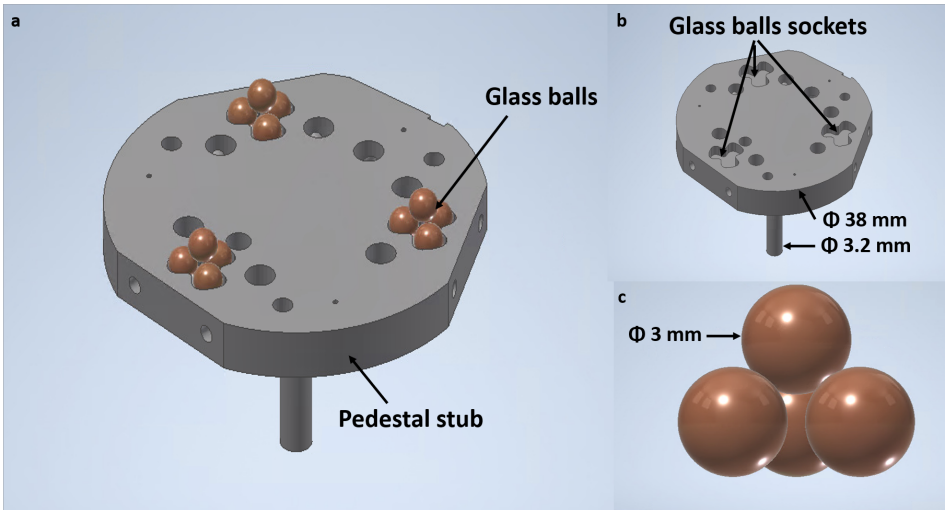

Figure 3.21: a) CAD drawing of the custom SEM stub (pedestal stub) with the glass balls in tetrahedron configuration mounted on the sockets. b) CAD drawing of the pedestal stub alone, with the 3 sockets to hold the glass balls. c) A close-up drawing of the 4 glass balls in tetrahedron configuration.

is shown in figure 3.24. The clamp is fixed to the sides of the pedestal by means of 2 M2 screws (shown in figure 3.24). The M2 screws are thermally isolated from the pedestal stub and clamp by insulator bushes. The clamp is sandwiched between two insulator bushes, we can use PEEK here as the temperature after 1

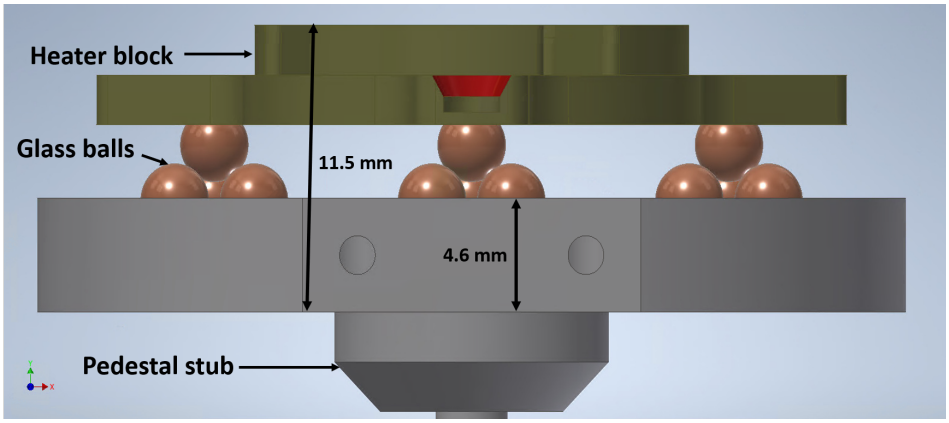

Figure 3.22: CAD drawing of the cross-section of the heater block mounted on the pedestal stub using 3 tetrahedron configurations of glass balls.

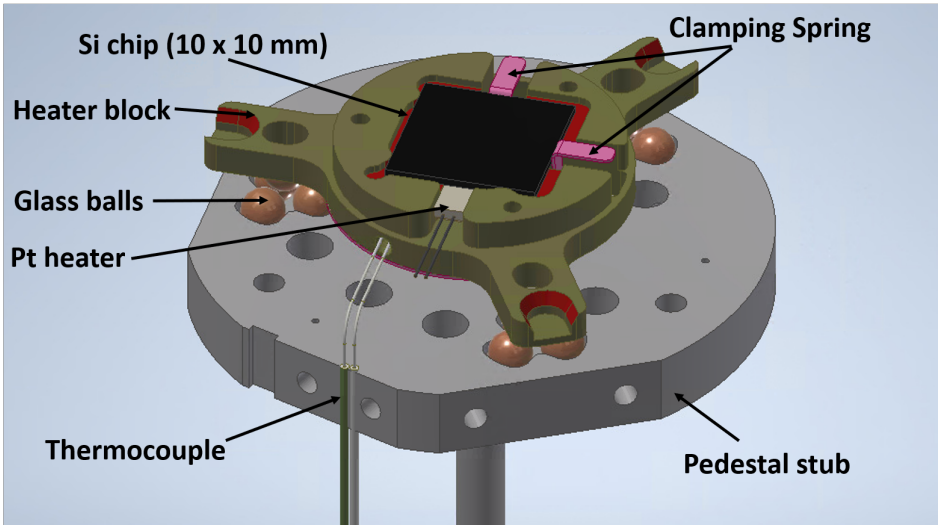

Figure 3.23: CAD drawing showing the substrate heater with a Si chip (10 x 10 mm^2) mounted on the heater block, which is in turn mounted over the pedestal stub using the glass balls in tetrahedron configuration. Also shown are the clamping springs which are used to mount the Si chip.

glass ball is around 53 ^oC as seen in figure 3.18. A close-up sideview of the clamp is shown in figure 3.25 along with the components.

The electrical connection to the Pt heater cannot be soldered as for the heater V1, as our desired temperature is well above the melting point of solder. So, we used spot welding to connect 2 wires to electrical connectors (with a dimension

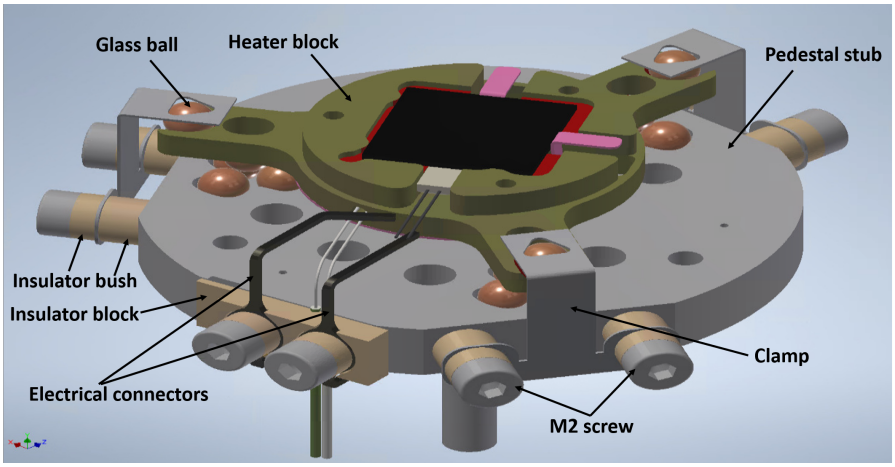

Figure 3.24: CAD drawing showing the 3 clamps which are used to fix the heater block over the pedestal stub. The electrical connection to deliver power to the Pt heater is implemented by 2 electrical connectors.

of 0.5 x 0.5 mm^2) which are clamped to the side of the pedestal stub, as shown in figure 3.24. The electrical connectors are thermally isolated by using a isolator block. A close-up of the electrical connectors is shown in figure 3.26. Also we need to electrically connect the heater block and the pedestal stub to prevent charging of the Si chip. Similar to the heater V1 design, we used a spring which is placed on the pedestal stub and a screw on the heater block to electrically connect them. The tensile relief structures for the wires can be seen in figure 3.26.

Next, we need to check, whether the heater block requires any shielding to protect the pole piece and the pedestal stub. From the CAD drawing, the backside of the heater block has an area of 382.47 mm^2. The power loss due to radiation as determined from equation 3.3 is 1.53 W. An ANSYS steady state thermal simulation is shown in figure 3.27 depicting the effect of radiation when a block similar to our heater block is kept at 300 ^oC, resulting in the temperature of the pedestal stub to increase to 122 ^oC. Hence, a heat shield is required to keep the pedestal stub at room temperature. Figure 3.28 shows an ANSYS steady state thermal simulation of the pedestal stub shielded by 3 heat shields when the heater block (a cylindrical block) is kept at 300 ^oC. The pedestal stub which rests on the SEM stage is kept at room temperature. A single heat shield is not enough to complete stop all the radiation, as seen in figure 3.28.

The CAD drawing of the stacked heat shield assembly is shown in figure 3.29, with a close-up look of the connection between two heat shields. We use a point contact to reduce heat transfer through conduction. A single heat shield has a thickness of 0.2 mm and the different levels of the heat shield are spaced apart by

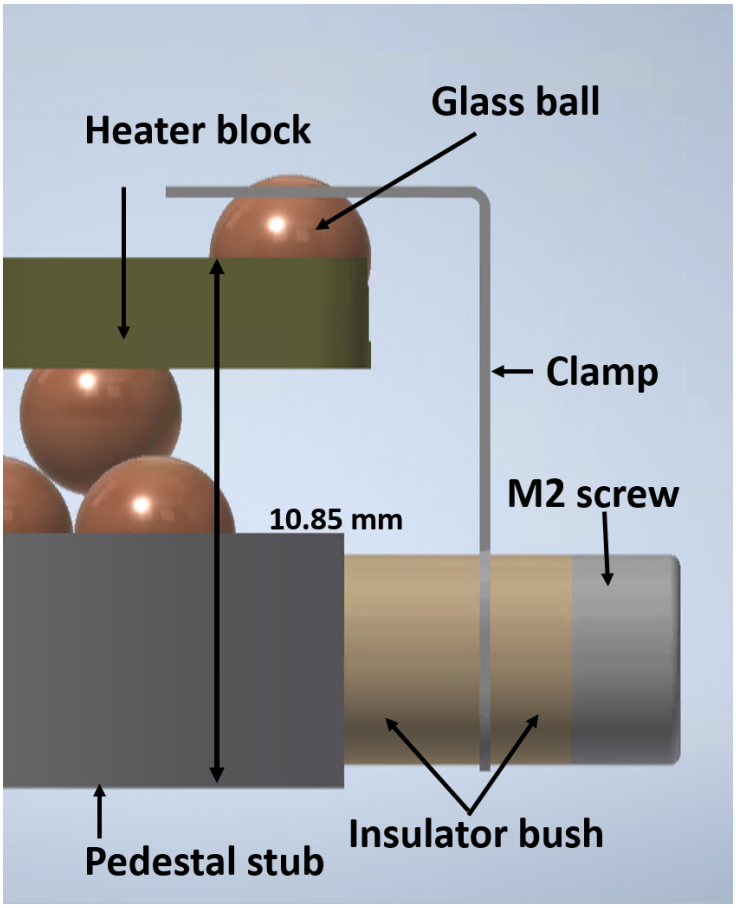

Figure 3.25: CAD drawing showing the side view of a clamp with the glass ball on top of the heater block and the insulator bushes to thermally isolate the clamp

0.6 mm. The different heat shields are fixed in such a way that there is minimum surface area between different heat shields (shown in 3.29 a) of 0.1 mm^2 (0.5 x 0.2 mm^2). Finally, we need to check whether we require a heat shield to protect the pole piece and the detectors. The total area of the heater block facing the pole piece without taking into account the Si chip is 233.24 mm^2. The radiated power from the heater block to the pole piece as calculated from equation 3.3 is 0.93 W (approx 1 W). An ANSYS steady state thermal simulation depicting the influence of 1 W radiated power on the pole piece (made of Mu metal) is shown in figure 3.30, resulting in the temperature of the pole piece to increase to 31 ^oC. Similar to the heater V1 temperature increase estimation, we estimate a temperature of 30 ^oC in 1 hour with a power of 1W. The Si chip adds an additional 0.43 W in radiated

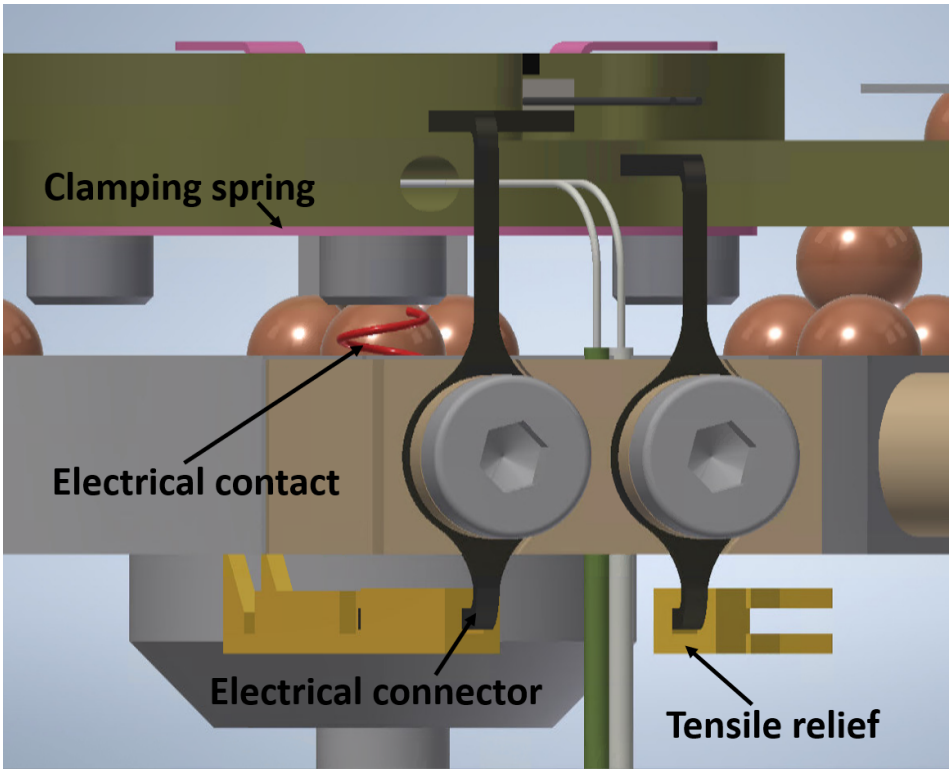

Figure 3.26: CAD drawing showing the side view of the electrical connectors, along with various other components.

power to the pole piece. With a radiated power of approximately 1.5 W at the pole piece, the temperature increases to 35 ^{o}C as determined from equation 3.3. Hence, we would require a heat shield to protect the pole piece and the detectors. The complete in-situ substrate heater with a heat shield over the heater block is shown in figure 3.31.

For cooling the substrate heater, similar to the heater V1, we can vent the SEM chamber and pump the chamber before the chamber reaches atmospheric pressure.

3.9. FABRICATION AND ASSEMBLY

The heater block is made out of Ti grade 5 as discussed in the previous section, and is machined (by a lathe tool) to the desired shape. The clamping springs plate is made out of sheet metal of stainless steel (316/ 1.4401) with a thickness of 0.2 mm and is non-magnetic. A water jetting tool (high pressure jet of water)

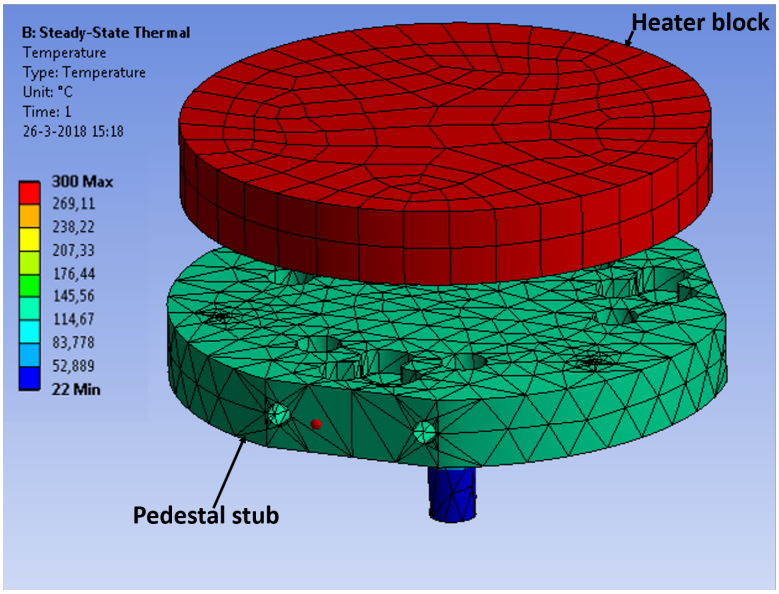

Figure 3.27: ANSYS steady state thermal simulation depicting the effect of radiation on the pedestal stub when the heater block (a cylindrical block) is kept at 300 ^{o}C. The temperature of the pedestal stub increases to a temperature of 122 ^{o}C. Image courtesy of Ruud van Tol.

was used to cut the sheet metal into shape. The glass balls with a diameter of 3 mm were bought commercially [24]. The pedestal stub is made out of stainless steel 316, and is machined to the desired shape. The three clamps are also made out of stainless steel 316 sheet metal and are cut into the desired shape by a water jetting tool. The insulator bushes and the insulator block are made out of PEEK as discussed in the previous section and are machined into the desired shape. The two electrical connectors are made out of stainless steel 316, machined to the desired shape. The spring which is used for the electrical contact between the heater block and the pedestal stub is made out of phosphor bronze as it is non-magnetic. For the tensile relief we used a gold coated crimp socket made out of brass [25]. The stacked heat shield is made out of stainless steel 316 sheet metal with a thickness of 0.2 mm. We used a water jetting tool to cut the sheet metal. The different levels of the stacked heat shield were fixed into position by laser welding. The pedestal ring is made of stainless steel 316 and is machined into shape. The heat shield is also made out of stainless steel 316 sheet metal with a thickness of 0.2 mm and was cut into shape using a water jet tool. Similar to heater V1, we used a commercially available K-type thermocouple for accurately measuring the temperature of the heater block [17].

After fabrication, all the sheet metal components were bent into the desired

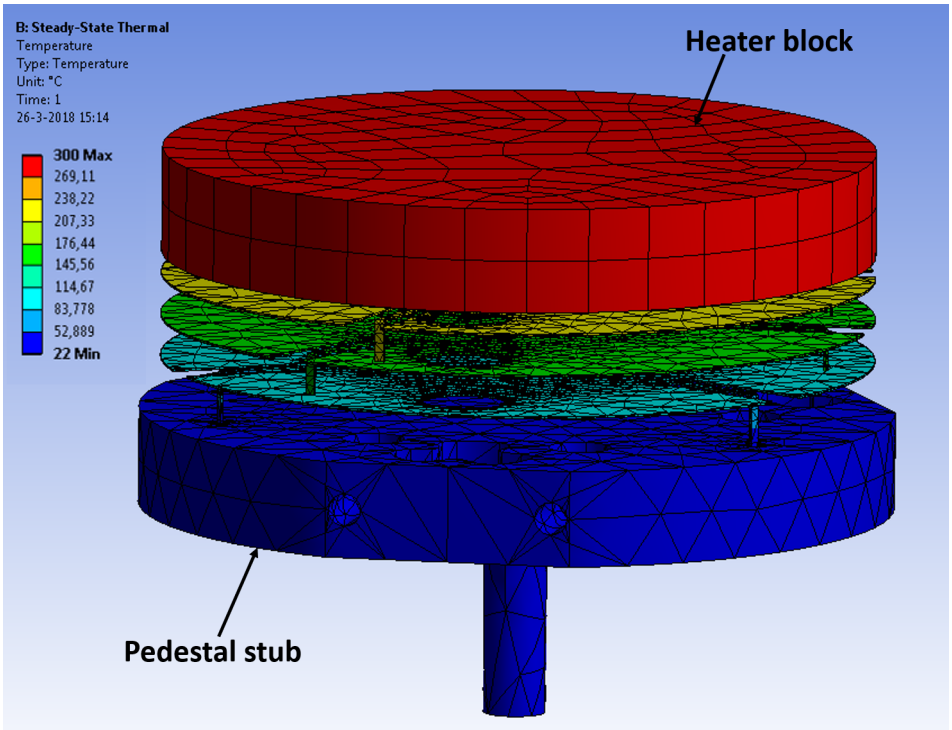

Figure 3.28: ANSYS steady state thermal simulation depicting the effect of radiation with the pedestal stub shielded by 3 heat shields, when the heater block (a cylindrical block) is kept at 300 ^{o}C. Image courtesy of Ruud van Tol.

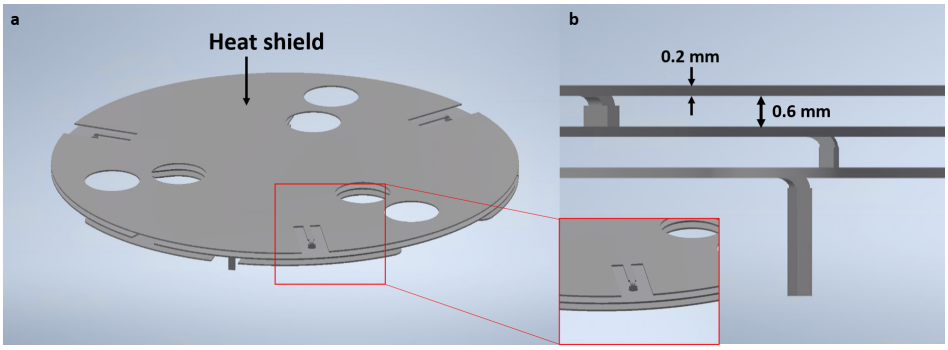

Figure 3.29: a) CAD drawing of the stacked heat shield assembly. Inset picture shows the connection between the two heat shield. b) CAD drawing of the heat shields in side view with the thickness of the heat shield and distance of separation between them.

shape. The various components need to be cleaned before installing in the SEM. Similar to heater V1, the metallic components (heater block, clamping spring,

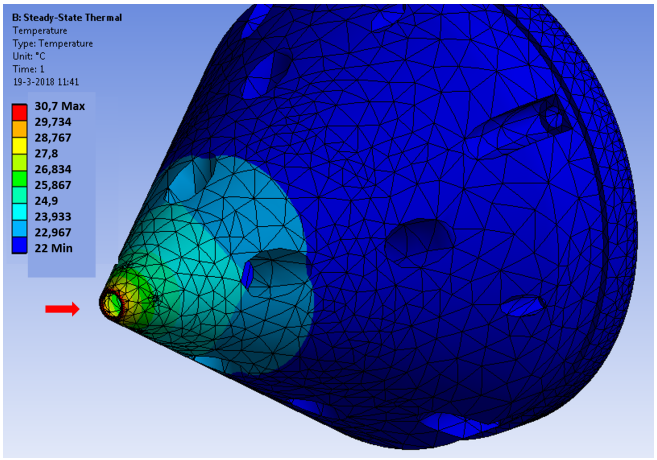

Figure 3.30: ANSYS steady state thermal simulation depicting the influence of 1 W radiated power on the pole piece assumed to consist of Mu metal. It results in a temperature increase to 31 ^{o}C at the bottom of the pole-piece (indicated by red arrow). Image courtesy of Ruud van Tol.

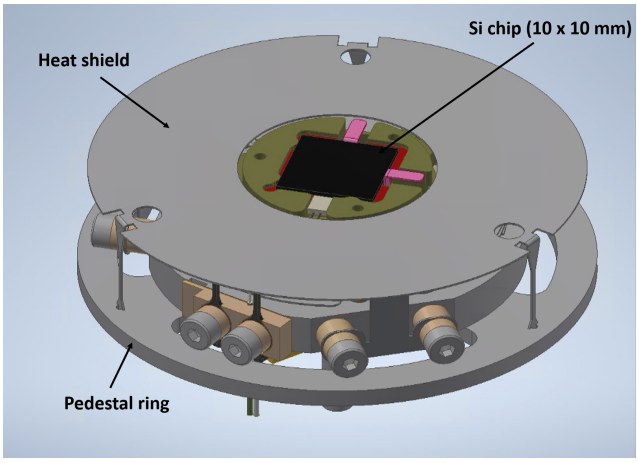

Figure 3.31: CAD drawing of the compete in-situ substrate heater with a heat shield covering the heater block.

pedestal stub, clamps, electrical connectors, screws, clamping spring, the stacked heat shield, pedestal ring, heat shield and the crimp socket) were cleaned in a beaker containing acetone for 2 hours in an ultasonic bath followed by another 2 hours of ultrasonication in an ethanol containing beaker. Finally the parts were blown dry by N_2. All the non-metallic components (Pt heater, the K-type thermocouple, insulator bush, insulator block and the glass balls) were placed in a beaker containing isopropyl alcohol in an ultrasonic bath for two hours. And

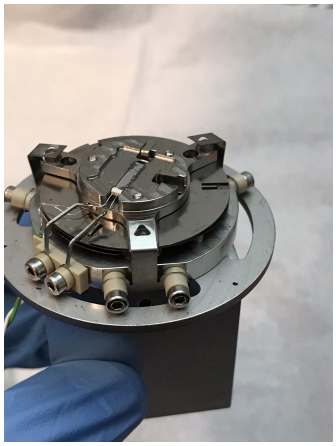

Figure 3.32: Photograph showing the in-situ heater after assembly but without Si substrate and upper heat shield.

blown dry by N_2.

Similar to the heater V1, we used the commercially available PELCO high temperature carbon paste to glue the platinum micro-heater to the heater block. The sample holder was air cured for about 2 hours and at 90 ^{o}C for 2 hours in a vacuum oven. This was followed by curing at 180 ^{o}C for 2 hours to achieve proper electrical and mechanical properties. We used this glue as it is easy to remove it by placing it in a beaker containing water. All the components were assembled based on the CAD drawing.

Finally the leads of the Pt micro-heater were laser welded to the contact leads. After the laser welding, the in-situ substrate heater was baked in a vacuum oven at 150 ^{o}C overnight to remove any contaminants from the laser welding. Figure 3.32 shows the photograph of the assembled heater (without the substrate and heat shield) on top of the Al block for the Nova Nano SEM. To deliver power, we used the same power source we used for heater V1. To accurately measure the temperature, we used a Graphtec Corporation midi LOGGER GL220 [26].

3.10. PERFORMANCE TESTS

Now that we have assembled the heater, it needs to be tested that our design holds i.e., whether the top heat shield, the stacked heat shield and the glass balls as isolator function in keeping the stage and the pole piece at room temperature. We need to measure the temperature radiated by the heater. This is done to test whether the design of the radiative shield keeps the detectors within their oper-

ating temperature. The pole piece is generally kept at a distance of 5 mm from the surface of the substrate. To mimic that, we constructed a setup in the SEM to measure the temperature at a distance of 4 mm from the substrate. Here, we replaced the pole piece with a piece of sheet metal made of stainless steel with a thickness of 0.2 mm. Two additional K-type thermocouples were connected to the shield and the stage (Al block) to measure the temperature of the shield and the stage. The thermocouple attached to the shield was glued to the shield by kapton tape. The thermocouple attached to the stage was placed in a hex screw hole in the Al block.

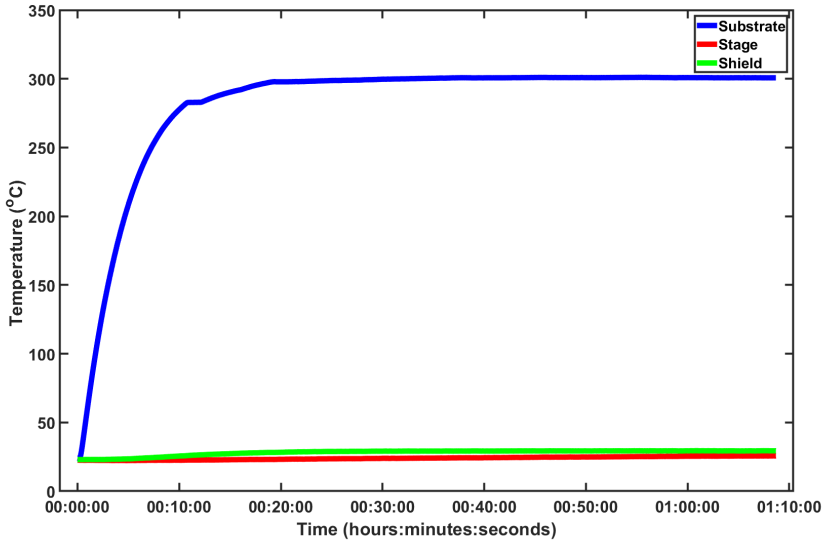

Figure 3.33: Graph showing the measured temperature of the substrate, the stage (Al block) and the shield used to test the radiation as we heat the substrate to 300 ^{o}C.

We placed the substrate heater in the SEM and moved the stage away from the pole piece towards the door of the SEM chamber. After a base pressure of 2x10^{-6} mbar is attained, we ramped the substrate temperature to 300 ^{o}C. Similar to heater V1, we heated the substrate by adjusting the power delivered to the Pt heater. Figure 3.33 shows the temperature of the substrate, the stage and the shield as a function of time. From figure 3.33, it is visible that we observe an increase of 2 ^{o}C and 6 ^{o}C for the stage and the shield respectively, when the sample holder is kept at a temperature of 300 ^{o}C. The shield's increase in temperature will be much higher than the actual increase in temperature for the pole piece, as we used a thin sheet metal for our testing. The increase of the stage temperature is at the top of the Al block, the actual stage with the sensitive piezo

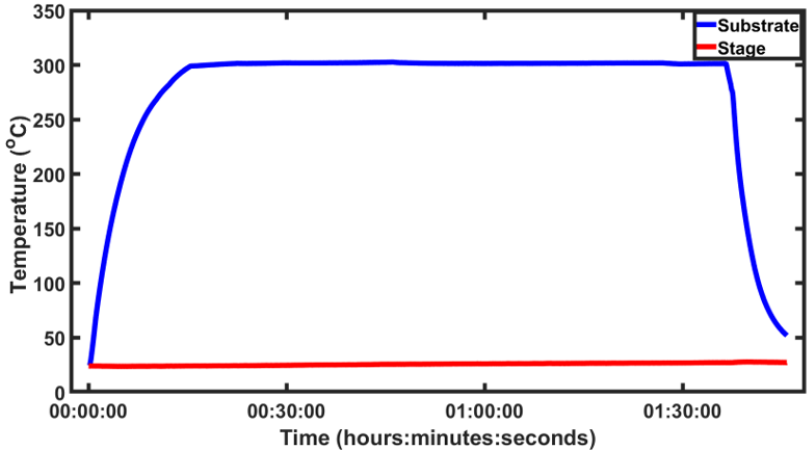

Figure 3.34: Graph depicting the temperature of the substrate and the stage as the substrate is heated to 300 ^{o}C. We are able to ramp-up the temperature to 300 ^{o}C in 15 minutes and ramp-down the temperature to 55 ^{o}C in about 10 minutes.

components is further away. This validates our design to thermally isolate the SEM stage from the substrate heater and the design of the radiation shield. The in-situ substrate heater is now safe to operate under the pole piece. Now that we can heat the substrate, we need to measure the time it takes to ramp-up and ramp-down the substrate temperature. The measured temperature of the substrate as we ramp-up and ramp-down the substrate is shown in figure 3.34. We are able to reach 300 ^{o}C in 15 minutes, resulting in a ramp-up rate of 18.4 ^{o}C/min and able to bring down the substrate temperature to 40 ^{o}C in about 10 minutes, resulting in a ramp-down rate of 25 ^{o}C/min. The ramp-down procedure utilized here was to vent the chamber completely. We could carry out cycles of chamber vent plus chamber pump to bring the substrate to room temperature. In addition, we carried out an experiment to determine the temperature driven drift while ramping up the substrate to 300 ^{o}C, this is shown in figure 3.35. We positioned the substrate over a patterned structure (indicated by the red cross in figure 3.35a) while at room temperature. The position of the patterned structure after the temperature is increased to 300 ^{o}C is shown in figure 3.35b. We can observe a shift of 25 μm in the X-direction and a shift of -28.25 in the Y-direction from the patterned structure. This is a consequence of the relaxed requirement of maintaining substrate position stability while varying the temperature in the heater V2 when compared with heater V1.

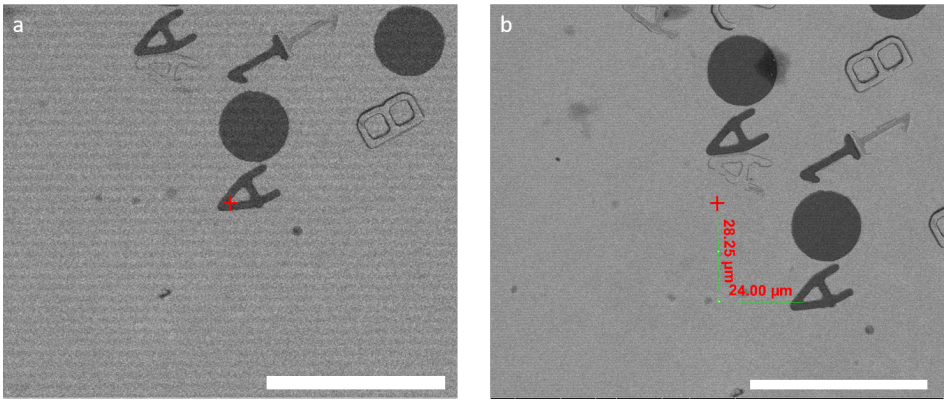

Figure 3.35: a) SE image of substrate centred at a patterned structure at room temperature (center indicated by a red cross). The scale bar is 50 μm. b) SE image of the substrate after the temperature is increased to 300^o C. We observe a shift of 25 μm in the X-direction and a shift of -28.25 in the Y-direction from the patterned structure. The scale bar is 50 μm.

3.11. CONCLUSION

To conclude, in this chapter we have set requirements for two in-situ substrate heaters, V1 and V2, presented the designs and fabrication process, as well as some initial tests. Heater V1 (designed for 150^{o}C, but it could reach temperatures up to 260 ^{o}C) was designed to meet the requirements for partial cleaning of the substrate, removal of adsorbed water and purification of FEBID structures. The heater $V1$ can be used to heat the substrate from room temperature to 260 ^{o}C. The target temperature for heater V1 was set at 150 ^{o}C, but due to a faulty temperature measurement setup we were able to use the heater up to 260 ^{o}C with an additional phosphor bronze clip to keep the substrate in place, and giving up on the low substrate drift. The upper limit of temperature, 260 ^{o}C stems from the temperature limit of the isolator block made of PEEK. We are limited to a sample size of 10 x 10 mm^2. To bring the substrate back to room temperature, we used the venting mechanism of the SEM chamber.

Heater V2 (capable of heating up to 300 ^{o}C) was designed to meet the requirement of in-situ thermal ALD processes. Heater V2 can be used to heat the substrate from room temperature to 300 ^{o}C. We replaced the isolator made of PEEK by glass to meet the temperature requirements. A series of heat shields were used to keep the SEM stage and the pole piece within their temperature range. Here also, the sample size is limited to 10 x 10 mm^2. We utilized the venting mechanism of the SEM chamber to cool the substrate to room temperature.

REFERENCES

[1] N. Maluf and K. Williams, *An Introduction to Microelectromechanical Systems Engineering*, Artech House Microelectromechanical Systems (Artech House, 2004).

[2] https://www.minco.com/wp-content/uploads/Minco Thermal-Solutions-Design-Guide.pdf, *"Minco Thermal Solutions Design Guide",* (retrieved 23-08-2021).

[3] https://www.minco.com/wp-content/uploads/Estimating-Power-Requirements-of Etched-Foil-Heaters.pdf, *"Estimating Power Requirements of Etched Foil Heaters",* (retrieved 23-08-2021).

[4] https://www.makeitfrom.com/material-properties/6082 T6-Aluminum, *"6082 T6-Aluminum",* (retrieved 23-08-2021).

[5] L. Zorana, S. Branko, Z. Milan, Z. Aleksandar, and H. Miodrag, *The determination of the emissivity of Aluminum allow AW 6082 using infrared thermography,* (2015) pp. pp. 23–26.

[6] http://asm.matweb.com/search/SpecificMaterial.asp?bassnum=MQ316J, *"Stainless steel 316",* (retrieved 23-08-2021).

[7] https://www.spacematdb.com/spacemat/manudatasheets/, *"Titanium Alloy Guide",* (retrieved 23-08-2021).

[8] S. Shrestha and K. Chou, *A Build Surface Study of Powder-Bed Electron Beam Additive Manufacturing by 3D Thermo-fluid Simulation and White-light Interferometry,* International Journal of Machine Tools and Manufacture **121** (2017), 10.1016/j.ijmachtools.2017.04.005.

[9] https://matmatch.com/learn/material/polytetrafluoroethylene-ptfe teflon, *"PTFE",* (retrieved 23-08-2021).

[10] https://www.engineeringtoolbox.com/emissivity-coefficients-d447.html, *"Emissivity of common materials",* (retrieved 23-08-2021).

[11] http://www.matweb.com/search/datasheet.aspx?matguid=0654701067d147e88e8a38c646dda195, *"Al_2O_3",* (retrieved 23-08-2021).

[12] T. Misuri, T. Vrebosch, L. Pieri, M. Andrenucci, S. Alta, M. Tordi, E. Marcuzzi, M. Bartolozzi, and S. Renzetti, *Telemicroscopy and Thermography Diagnostic Systems for Monitoring Hall Effect Thrusters,* (2011).

[13] https://www.corning.com/worldwide/en/products/advanced-optics/product-materials/specialty-glass-and-glass-ceramics/glass-ceramics/macor.html, *"MACOR",* (retrieved 23-08-2021).

[14] G. W. Armin Berenjian, *History and Manufacturing of Glass,* **Vol. 7**, pp. 18 (2017).

[15] https://shop.allectra.com/products/343-HEATER-2X10-V2, *"343-HEATER-2X10-V2",* (retrieved 23-08-2021).

[16] https://super-metals.com/wp content/uploads/2015/04/Mumetal.pdf, *"Super-metals, Mumetal Magnetic Shielding",* (retrieved 23-08-2021).

[17] https://nl.rs online.com/web/p/thermocouples/6212158/?sra=pstk, *"RS PRO Type K Thermocouple 1m Length, 2mm Diamter",* (retrieved 23-08-2021).

[18] https://www.agarscientific.com/sem/specimen-stubs-mounts/sem-specimen-stubs 46, *"Agar scientific, SEM specimen stubs, 32mm Dia, 8mm pin",* (retrieved 23-08-2021).

[19] https://nl.rs-online.com/web/p/pcb headers/9094394, *"PCB Pin Header",* (retrieved 23-08-2021).

[20] *"PELCO High Temperature Carbon Paste",* (retrieved 23-08-2021).

[21] https://www.delta-elektronika.nl/en/products/dc-power-supplies-150w-es150 series.html, *"ES150 SERIES",* (retrieved 23-08-2021).

[22] https://www.integritystainless.com/wp-content/uploads/2016/07/NAS CR-Grade-316-316L.pdf, *"Stainless Steel 316, 316L",* (retrieved 23-08-2021).

[23] P. Hanzelka, J. Vonka, and V. Musilova, *Low conductive support for thermal insulation of a sample holder of a variable temperature scanning tunneling microscope,* Review of Scientific Instruments **84**, 085103 (2013), https://doi.org/10.1063/1.4817214 .

[24] *"Fabory, Glass ball 3mm, Article number 66990.003.000 ",* (retrieved 23-08-2021).

[25] https://nl.farnell.com/amphenol-icc-fci/47745-001lf/crimp-socket-22-26awg/dp/1097977?CMP=GRHB SF-OEM, *"Crimp Socket, 47745-001LF",* (retrieved 23-08-2021).

[26] https://www.dataq.com/resources/obsolete/products/gl220/, *"Graphtec Corporation, GL220 midi data logger",* (retrieved 23-08-2021).

4

AREA SELECTIVE THERMAL ALD IN SEM

4.1. INTRODUCTION

In the previous chapter, we demonstrated two in-situ substrate heaters V1 and V2 which can go upto 250^{o}C and 300^{o}C, respectively inside the SEM. The heater V2 satisfies the temperature requirement for having an in-situ ALD tool inside the SEM. If we are able to achieve the pressure requirement, sufficient local high pressure for ALD process, we will be able to achieve an in-situ ALD process in the SEM. We would require a miniaturized ALD tool as it can produce a pure layer of material with precise control over the deposited layer thickness. With area selective ALD we can pattern and grow a layer in the desired shape without any pattern transfer process. The working principle of ALD was briefly discussed in chapter 2, it involves the sequential dosing and purging of the precursor and the co-reactant alternatively. It is a self-limiting process. A single cycle of ALD results in the growth of a monolayer or sub-monolayer. The desired thickness is obtained by carrying out these cycles for the desired time. ALD operates in a temperature range in which the growth rate is uniform. Each precursor and co-reactant pair has its own temperature window. Outside the temperature window, the growth rate is poor or more like CVD deposition. At low temperatures, the growth rate is low due to low reaction rates or high due to precursor condensation. At high temperatures, the growth rate is high due to thermal decomposition of the precursor resulting in a CVD type growth or low due to reduced residence time of the precursor on the substrate [1]. The growth per cycle is well documented in the literature for a particular precursor and co-reactant. The main advantages of ALD are its conformal nature, atomically precise growth and pu-

rity. Due to its conformal nature, it is easy to deposit material on 3D structures. Area selective ALD is a special type of deposition, in which deposition takes place only in the area of interest instead of the whole substrate like in conventional ALD. Area selectiveness is achieved by either activating an area or deactivating it for ALD growth. There exist several strategies to activate or deactivate an area. Self-aligned monolayers (SAM) can be used to achieve area selective ALD. The SAM can be patterned in various ways [2].

Pt thermal ALD, for example uses $MeCpPtMe_3$ as the precursor. The co-reactant used is either O_2 or dry air. The only observable difference between the two co-reactants is that using O_2 as the co-reactant results in a better adhesion to the substrate [3]. The temperature window for Pt ALD is between 225^{o}C and 300^{o}C. The growth rate at 300^{o}C is about 0.045 nm/cycle and at 250^{o}C it is about 0.04 nm/cycle [4]. The observed growth per cycle is less than a monolayer, due to steric hindrance. The precursor molecule hinders the adsorption of the precursor molecule to adjacent sites due to its size.

Area selective ALD of Pt is achieved using Pt FEBID seed layers [5][4][6]. This process combines the high-resolution capability of FEBID with the precise growth of ALD along with a pure deposit overcoming the disadvantage of FEBID. This approach of using FEBID seed layers for area selectiveness has been termed as the direct write approach [5]. The FEBID seed layers are made in an SEM and the sample is introduced in a standard ALD tool for the ALD deposit. We want to integrate an in-situ ALD in an SEM so we can combine the two processes in a single instrument. This approach has already been tried [7], but the deposit did not show ALD growth but rather a CVD type growth. At the same time as this research was carried out, the Huth group in Frankfurt published an article with the same target of having an in-situ ALD in SEM [8]. We will describe the differences later.

4.2. REQUIREMENTS FOR ALD IN SEM

When we add the miniature ALD tool, it shouldn't affect the normal operation of the SEM i.e., we should be able to use the SEM for inspection. This criterion, in addition to the restrictions mentioned in chapter 2. leads us to several requirements for implementing the add-on ALD.

1 The precursor and the co-reactant gas shouldn't interact with any of the components of the microscope.

2 For the supply of the co-reactant, the gas should be introduced to the chamber.

3 A substrate heater that reaches up to 300^{o}C, as most of the ALD process temperature window is around this temperature.

4 During the precursor and co-reactant dosing, the local pressure should be sufficiently high to get the ALD process going.

5 All materials used should be non-magnetic.

6 All materials used should be vacuum compatible and have low outgassing.

7 If insulating materials are used, they should be shielded from the direct line of sight of the electron beam.

8 No additional pump should be needed.

We need to choose an ALD process which satisfies the requirements. The precursors used for ALD are generally CVD precursors, and for FEBID the precursors used are often the same CVD precursors. Due to this, as a first step, we can look into the ALD process which uses the same precursors as FEBID processes since these precursors have been tested extensively in the SEM. The precursor should be chosen such that the temperature required to heat up the precursor should be within the temperature range of the heating element. Also, the precursor should be chosen such that it is easy to re-fill the precursor and it should not be toxic. The common co-reactants for ALD processes are O_2, O_3, dry air(80% N_2 and 20% O_2), H_2O and H_2 [9][10][11]. This results in safety concerns as some of these co-reactants explode when exposed to atmosphere. We developed our own in-situ substrate heater which can reach up to 300^oC as discussed in chapter 3, which satisfies the temperature requirements for most of the ALD processes. In a standard ALD tool, during the precursor and the co-reactant dosing the chamber reaches a high pressure at which we can't operate the SEM. This issue needs to be solved in order to carry out ALD in the SEM.

4.3. DESIGN OF THE ALD SETUP

For our experiments, we are using a Nova Nano 600i dual beam scanning electron microscope from Thermo Fisher Scientific. Here, we will concentrate on implementing area selective thermal ALD of Pt. The precursors used for Pt ALD are $MeCpPtMe_3$ and $Pt(acac)_2$ [11][7]. Here we will utilize the $MeCpPtMe_3$ precursor, which is also used for Pt FEBID. During the precursor dosing, the chamber pressure is around $1-25$ mbar as discussed in chapter 2. The SEM can't operate at this pressure, hence the precursor can't be flooded into the chamber directly. For Pt FEBID, we use a GIS for the local delivery of the precursor gas close to the substrate. Through the use of a GIS the local pressure near the substrate is increased, hopefully enough to enable in-situ ALD. Here, we decided to go with dry air as the co-reactant as it is easier to implement due to safety reasons. For delivery of the co-reactant we need to bring in the dry air into the SEM, we cannot

flood the chamber due to the reason mentioned above. The best solution here would be to have a directed flow similar to the GIS. Since we already have a GIS in place, it would be easier to replace the GIS needle with a modified one, that can deliver gas from outside the SEM. The modified GIS needle with a side entry port for gas, is mounted to a GIS module of which the valve remains closed and is used as holder for the modified needle, is shown in figure 4.1. Now, we will be able to locally deliver dry air near the substrate.

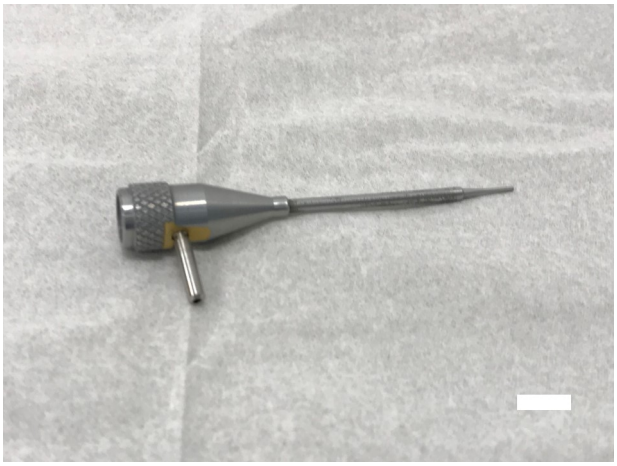

Figure 4.1: Photograph of the needle assembly with gas feed for the co-reactant. Scale bar is 6 mm.

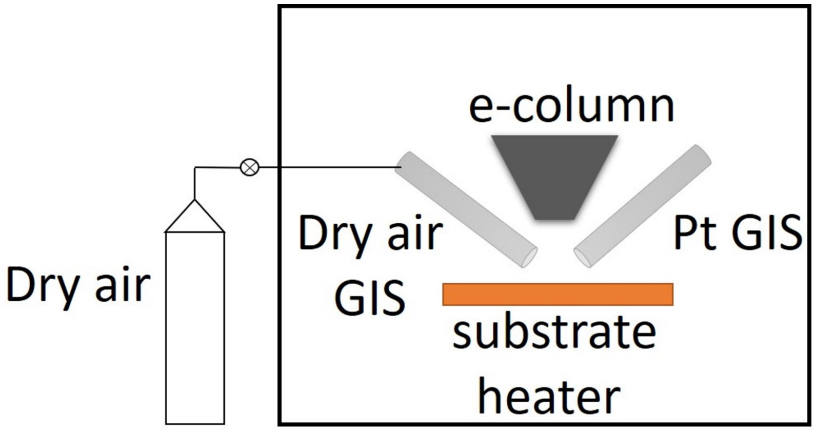

Figure 4.2: Sketch of the setup for in-situ ALD inside an SEM.

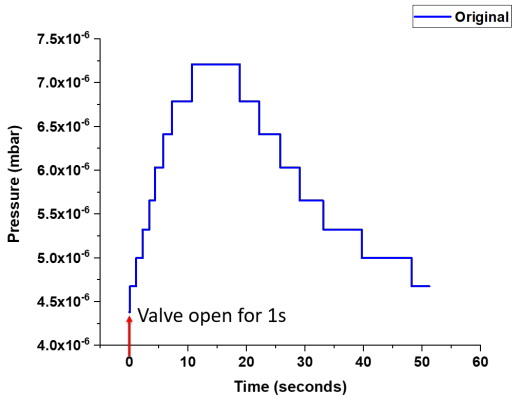

Figure 4.3: Pump down curve for the platinum precursor when valve is opened for a second.

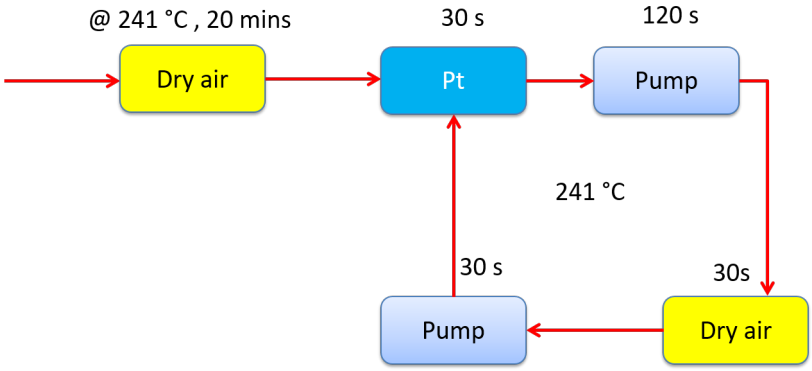

Figure 4.4: Illustration showing the recipe of an ALD process in SEM, along with the purification step.

In a standard ALD tool, the chamber walls are heated to prevent the precursor from condensing onto the walls. This cannot be done in an SEM chamber, because of the presence of delicate parts. Moreover, in a standard ALD tool, the whole chamber is flooded with the precursor, requiring chamber heating. In our case, we have local high pressure only near the region of interest. The sketch of the setup inside the SEM is shown in figure 4.2 showing the different components. In figure 4.2, the substrate lies on top of a heater, the precursor gas is fed through a GIS, which has been brought near the substrate. The co-reactant gas is also delivered close to the substrate through the use of another GIS (modified GIS needle with gas delivery). In area selective ALD, there is only growth in the seed layer area. Inside the SEM, we can use the FEBID technique by using the

precursor GIS and an e-beam to deposit the seed layers.

We now need to develop a recipe for ALD in SEM. From literature we observe that a cycle duration is a couple of seconds [5][7]. To estimate the precursor gas dose and purge time inside the SEM, we carried out pump down curve measurements i.e., we introduced the Pt precursor into the chamber and noted the time it takes to reach the base pressure when the gas supply is cut off. This is shown in figure 4.3. We did the same for the dry air co-reactant. Based on these results we decided on the cycle duration as shown in figure 4.4. Here, we choose a substrate temperature of 241^oC, which is well below the temperature requirement for the ALD process. For the thermal Pt ALD process using the precursor $MeCpPtMe_3$, the temperature window of the ALD process starts at 200^oC [12]. But the growth per cycle at this temperature is low (approx. 0.01 nm/cycle). At a temperature of 241^oC, we have a growth per cycle of 0.04 nm/cycle. So, we can use our heater V1, which can go upto a maximum temperature of 250^oC for our initial experiment. Figure 4.5 shows the Pt GIS and dry air GIS inserted close to the substrate.

We begin by patterning Pt FEBID seed layers on a substrate. The deposited seed layers contain $15-20$ at.% of Pt with the rest being carbon. It has been observed that baking the substrate at 150^oC with a flow of oxygen resulted in the purification of the Pt/C FEBID seed layers in the absence of an electron beam [8]. For the Pt ALD processes carried out without the purification step, there is a reduced growth. The reason for the reduced growth is because in the first few cycles, combustion of the carbon present in the seed layer takes place resulting in the purification of the seed layer. After the combustion, the normal ALD cycle begins resulting in a reduced total growth. Thus the deposited seed layers need to be purified. We bake the substrate at 241^oC for 20 minutes with a flow of dry air to purify the deposited seed layers. We chose a temperature of 241^oC, to begin the ALD process immediately after the purification step. After the initial cleaning step, we proceed with the precursor dosing of about 30 seconds. We choose this value as we want to operate in the saturation regime and not in an under saturated regime where the growth rate is lower than the ALD growth rate. After the initial test of the ALD in SEM, the dosing time can be brought closer to a time found in a standard ALD tool. The Pt precursor dosing is followed by a purge to remove the leftover precursors from the chamber. We chose a time of 120 seconds as this is the time it takes to reach the base pressure after closing the valve. The co-reactant is dosed into the chamber following the purge. We chose a duration of 30 seconds for the same reason as for the precursor dosing to operate the process in the saturated regime. This step is followed by the purge step which is done to remove any leftover co-reactants from the chamber, similar to the previous step we chose a duration of 30 seconds based on the pump down time and to operate in the saturated regime.

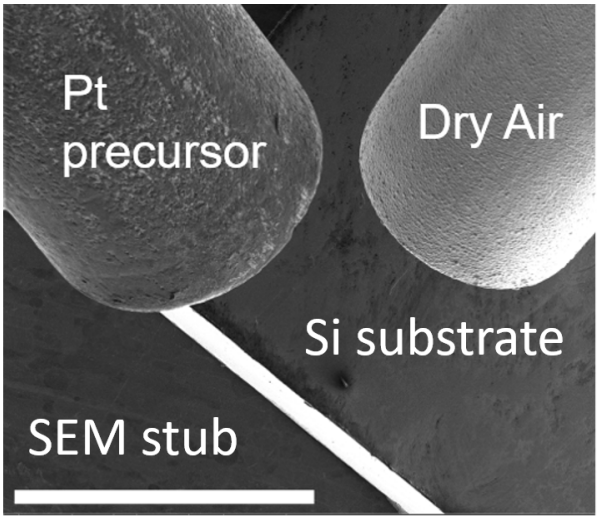

Figure 4.5: Secondary electron image showing the Pt GIS and dry air GIS inserted close to the substrate. The slanted white edge seen from the Pt precursor is the edge of the Si substrate. Scale bar is 1 mm.

4.4. FIRST ALD IN SEM EXPERIMENTS

Si substrates of 1 x 1 cm were used as substrates. First the Si substrates were cleaned using the solvent clean method: acetone clean for 15 minutes followed by ethanol clean for 15 minutes. For the FEBID seed layer deposition, we used the following parameters, 5 kV, 98 pA, 1μs dwell time and 11.41 nm pitch to pattern series of squares with 1 x 1μm^2 dimensions. The dose for the patterned seed layers was varied by increasing the passes (133, 266, 532, 665, 1064, 1328, 1993, 2658, 6650 and 13275) as follows, 0.1, 0.2, 0.4, 0.5, 0.8, 1, 1.5, 2, 5 and 10 nC/μm^2. The seed layer patterns were repeated on a control wafer in the same run to determine the growth after ALD cycles. The ALD process was started once a base pressure of 4x10^{-6} mbar was reached. This is done to minimize the effect of background water vapor and other contaminants present in the chamber. Also, we heat the GIS for half an hour before we start the process. This is done to make sure the whole GIS is heated.

Once the base pressure is reached, we ramp-up the temperature of the substrate to 241 ^{o}C and bake the substrate in the flow of dry air to purify the deposited seed layers. After the purification step, we immediately begin 17 cycles of ALD with the recipe shown in figure 4.4 keeping the substrate at a tempera-

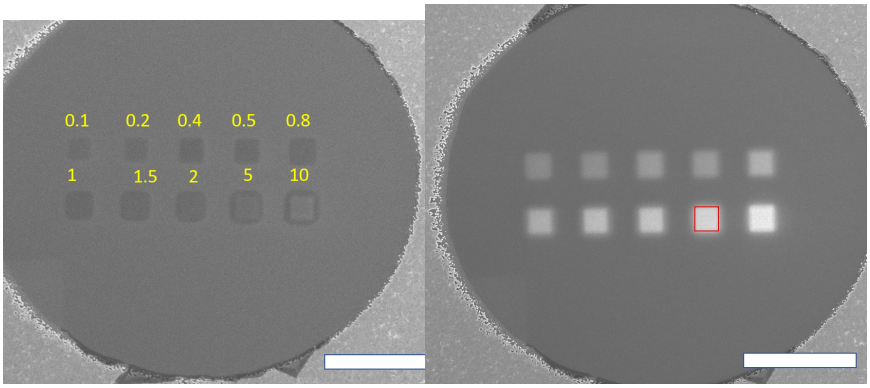

Figure 4.6: a)Secondary electron image of Pt/C seed layers grown by FEBID with varying doses (indicated in nC/μm^2). b)Secondary electron image of the same seed layers after 17 cycles of ALD, with a clearly observed contrast change. Inset red rectangle shows the layer shown in figure 4.7. Scale bar is 5 μm

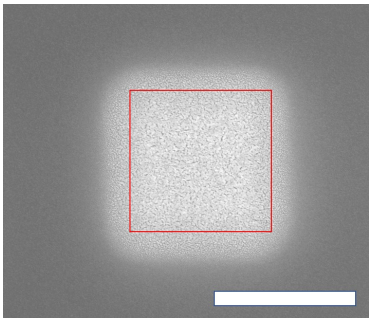

Figure 4.7: Secondary electron image of one of the layers seen in figure 4.6 after 17 cycles of ALD, with the observed contrast change and the granular structure of the deposit. The inset shows the rectangular area exposed to the electron beam while depositing the seed layer. Scale bar is 1 μm

ture of 241 ^{o}C. Figure 4.6a shows the SE micrograph of the seed layers before the ALD process. For lower doses, the deposited seed layers look dark. As the dose of the deposit increase, we observe a brighter deposit area due to more Pt being deposited at higher doses. After the ALD cycles, when we take an SEM image, we observe a contrast change over the patterned layers as shown in figure 4.6b. A similar contrast reversal of the FEBID seed layers after ALD was observed in [13][7]. This observed contrast change is due to the growth of the layer [13][7]. Any carbon present in the seed layer would be combusted due to the catalytic reaction of Pt in the presence of dry air at 241 ^{o}C. A close-up of the seed layers showing the granular structure of the deposit after ALD is shown in figure 4.7. An EDX measurement could not be done on these samples as they are too thin.

Moreover we observe Pt growth outside the seed layer. This region corresponds to the carbon halo observed in the Pt/C seed layers before ALD. The carbon halo is a result of the dissociation of the precursor molecules by the secondary electrons generated by the BSE. The size of the halo varies with the primary energy of the electron beam. Even for a dose of 0.1 nC/μm^2 we observe a contrast reversal, so we could reduce the initial seed layer dose further. In our in-situ ALD setup, it takes about 3 minutes and 30 seconds to complete a single cycle of ALD, whereas in a standard ALD tool it takes less than 30 seconds for a single cycle [4].

We reduced the time duration to 3 minutes by reducing the Pt dosing to 15 seconds and the purge time of the co-reactant dry air to 15 seconds as shown in figure 4.8. The lowest dose for the seed layer we used in the previous experiment was 0.1 nC/μm^2. We can further lower the dose of the seed layers to estimate the minimum dose required for the ALD growth. Thus we patterned Pt seed layers with a dose of 0.001, 0.01, 0.02, 0.04, 0.05, 0.06, 0.08, 0.1, 0.2 and 1 nC/μm^2 by varying the passes 1, 13, 27, 53, 66, 80, 106, 133, 266 and 1328 respectively. The patterns were repeated on a control wafer at the same time to determine the growth after the ALD cycles. The ALD process was repeated with the modified recipe for 17 cycles at a substrate temperature of 241 ^{o}C. Similar to the previous experiment, we see a contrast change (figure 4.9 a and c) immediately after the ALD cycles. We used an AFM in SEM tool from Nano Analytik for AFM measurements [14][15]. We carried out AFM measurements of the seed layer after purification and of the seed layer after 17 cycles of ALD indicated by the red rectangles in figure 4.9 i.e., at a dose of 0.1 nC/μm^2. We observe a growth of 0.7 nm after 17 cycles of ALD (from figure 4.9 b and d), i.e. 0.04 nm/cycle, in excellent agreement with the literature data for Pt ALD growth rate at that temperature of 0.04 nm/cycle [12]. For doses below 0.1 nC/μm^2, we observed not a continuous Pt seed layer. So a dose value of 0.1 nC/μm^2 must be kept as the lowest limit for the seed layer. We have now demonstrated a working in-situ ALD in an SEM. Even though we have a working ALD in SEM, it takes about 3 minutes for a single cycle. This is a serious drawback for the ALD in SEM, that needs to be overcome to make it viable as an alternative to a standard ALD process.

4.5. DECREASE THE ALD PROCESS TIME

Needle configuration	Rise time (s)	Plateau time (s)	Decay time (s)
Standard needle	9.5	8.5	29

Table 4.1: Table showing the time it takes for the platinum precursor to reach a maximum value, saturation time and time taken to reach the base pressure.

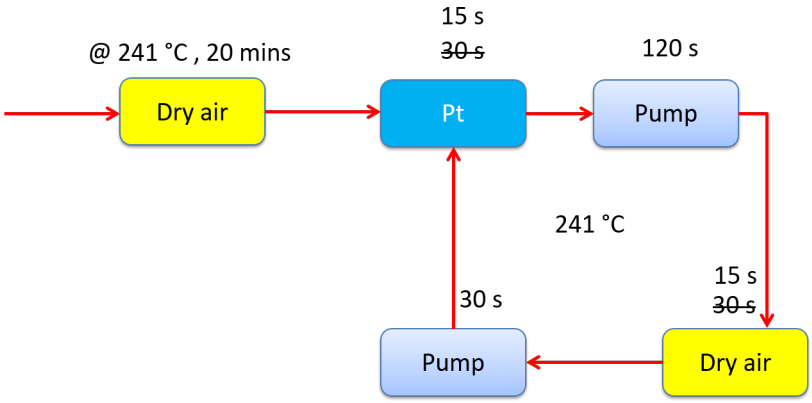

Figure 4.8: Illustration showing the modified recipe of an ALD process in SEM.

If we take a look at the recipe for the in-situ ALD process in SEM shown in figure 4.4, the main reason for the long duration of a cycle is the Pt precursor purge time of 120 s. Looking at the pump down curve for the Pt precursor shown in figure 4.10, it takes about 50 seconds to reach the base pressure after a Pt dosing for 1 second. We can divide the pump down curve into three regions: region-1 to reach the maximum value (rise time), region-2 of the maximum value (plateau time) and region-3 to reach the base pressure starting from the maximum value (decay time). Table 4.1 shows the different time taken by the three regions in the pump down curve. We observe, it takes about 9.5 seconds to reach the maximum pressure, even though the valve was kept open for 1 second. Also, the plateau time is observed to be about 8.5 seconds followed by a decay time of 29 seconds. The long rise time (Region 1 in figure 4.10) long plateau (Region 2 in figure 4.10) and the long decay times (Region 3 in figure 4.10) are caused by the location of the valve in the standard GIS.

Figure 4.11 shows a photograph of the GIS, crucible, the plunger which acts as the closing valve, and the GIS needle. Also the location of the valve is indicated. The crucible is filled with the precursor, in our case the Platinum precursor. The plunger controls opening and closing of the valve. The GIS needle delivers the gas near the substrate from the crucible. The valve of the GIS is located 7.5 cm above the tip of the needle. The total volume of the GIS needle behind the valve towards the nozzle is about 271 mm^3. The internal surface area of the needle behind the valve to the end of the needle is about 428 mm^2. For gas removal from a vacuum system by a pump, we can use the following equation, t = V/S_{eff}*ln(P_o/P) where V is the volume in m^3, S_{eff} is the effective speed of the pump (2.10^{-3} l/s conductance of the GIS needle), P_o is the initial pressure in

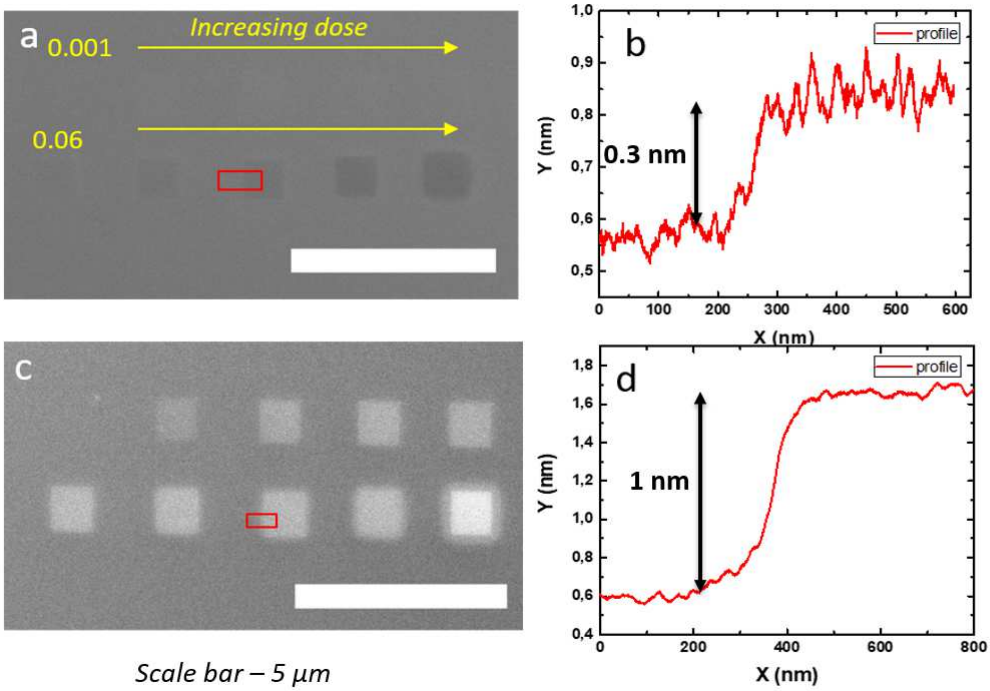

Figure 4.9: (a) Secondary electron image of Pt/C seed layers deposited with various doses (indicated in nC/μm^2) (b) AFM profile over the seed layer indicated by the red rectangle. (c) Secondary electron image of the same seed layers after 17 cycles of ALD, with a clearly observed contrast change. (d) AFM profile of the same seed layer as in a) after 17 cycles of ALD. The scale bar is 5 μm.

Pascal and P is the final pressure in Pascal [16]. The above equation doesn't take into account the effects of desorption, diffusion and permeation in gas removal. Based on the above equation, if we calculate the amount of time it takes to remove the precursor gas from the GIS needle, it should take about 2 seconds to completely remove the volume of gas. But in reality, it takes us a total of 37.5 s (8.5s from region-2 plus 29 s from the region-3). The longer time is because there is also the surface area with which the gas interacts. The Pt precursor when travelling from the valve to the end of the needle, collides with the internal surface of the needle, gets adsorbed to the surface and after some time desorbs from the surface. This time of residence on the surface is called the residence time. The residence time is a function of temperature, lower temperature leads to an increased residence time whereas higher temperatures results in a shorter residence time [17]. The Pt crucible is heated to a temperature of 45 ^{o}C in a GIS.

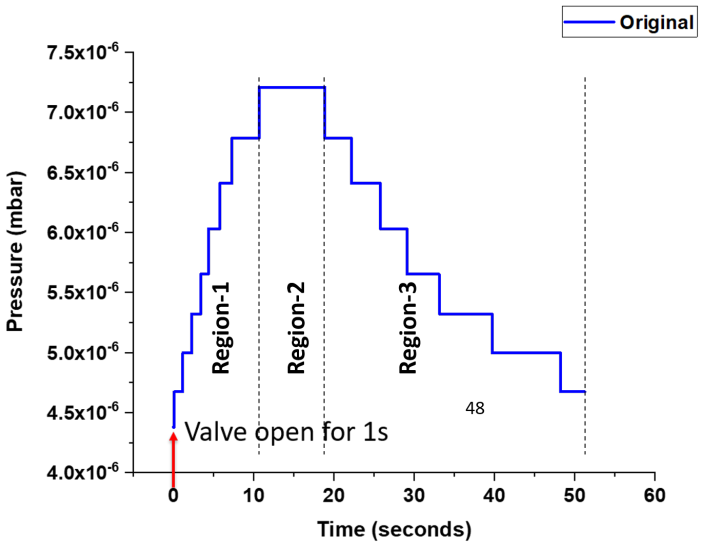

Figure 4.10: Graph showing the pump down curve for the Pt precursor when the valve is kept open for 1 second.

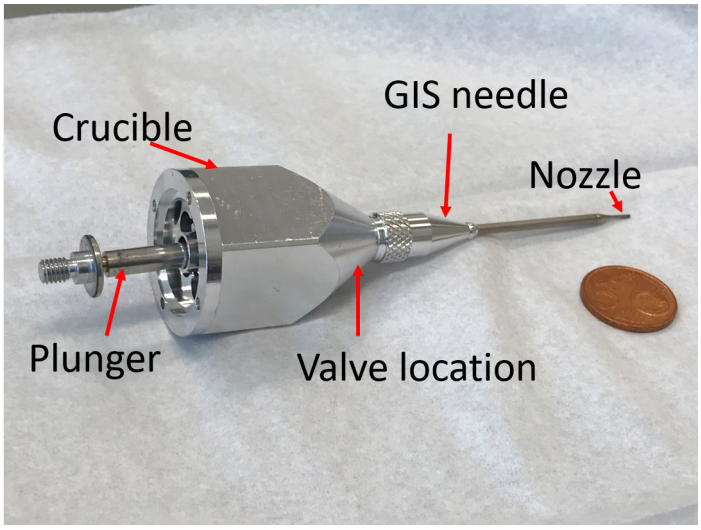

Figure 4.11: Photograph showing the GIS crucible, needle assembly, nozzle and the plunger valve.

Figure 4.12 shows an ANSYS transient thermal simulation of the GIS needle assembly with the crucible, 600 s after raising the crucible to a temperature of 50 ^{o}C. The nozzle of the needle assembly is at a temperature of 41.7 ^{o}C, a reduction

of 8.3 ^{o}C from the crucible to the nozzle. In reality, for Pt precursor the GIS crucible is heated to 45 ^{o}C, we should expect the temperature of the nozzle to be 36.7 ^{o}C. This temperature is a little above the melting point of the Pt precursor 30 ^{o}C -31 ^{o}C (MeCpPtMe$_3$, CAS: 94442-22-5). And in a standard ALD tool, the precursor gas lines and the chamber walls are heated to a temperature of 70 ^{o}C to prevent condensation. We cannot heat the chamber walls of the SEM chamber. To replicate this, we could increase the Pt crucible temperature but this will result in a faster consumption of the precursor. An alternative solution would be to reduce the internal surface area of the needle behind the valve. This can be achieved by extending the plunger and the valve towards the end of the needle.

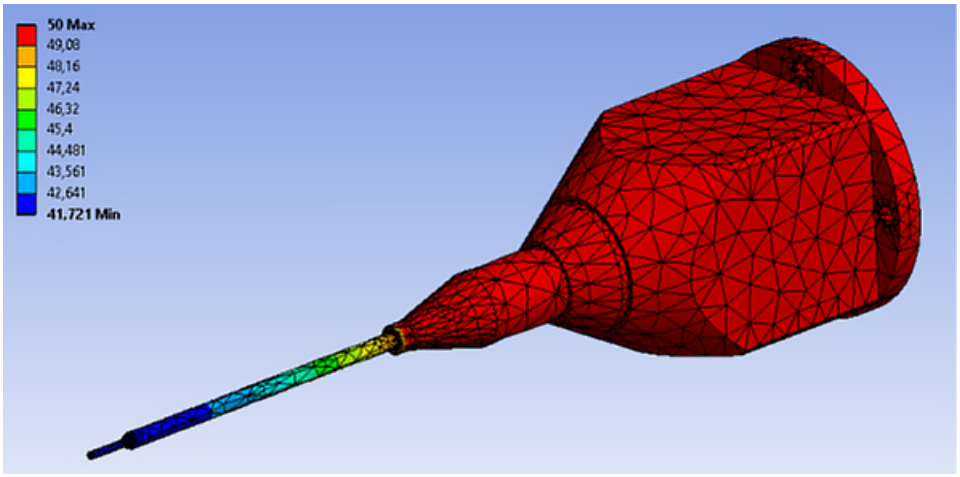

Figure 4.12: ANSYS transient thermal simulation of the GIS needle assembly with the crucible, 600s after raising the crucible to a temperature of 50 ^{o}C. Image courtesy of Youp van Goozen.

4.6. DESIGN OF THE MODIFIED GIS NEEDLE ASSEMBLY

Figure 4.13 shows the CAD drawing of the current GIS needle assembly showing the different parts. A zoom-in of the needle is shown in figure 4.14. The inner diameter of the needle and the nozzle is 1.5 mm and 0.5 mm respectively. The outer diameter of the needle and the nozzle is 2 mm and 1 mm respectively. The proposed solution is to move the valve shown in figure 4.13 near the nozzle. Figure 4.15 shows the proposed solution by extending the plunger towards the nozzle. A new needle needs to be fabricated to move the valve near the nozzle and to have the plunger extension.

Figure 4.16 shows the new arrowhead valve which will be used as the close

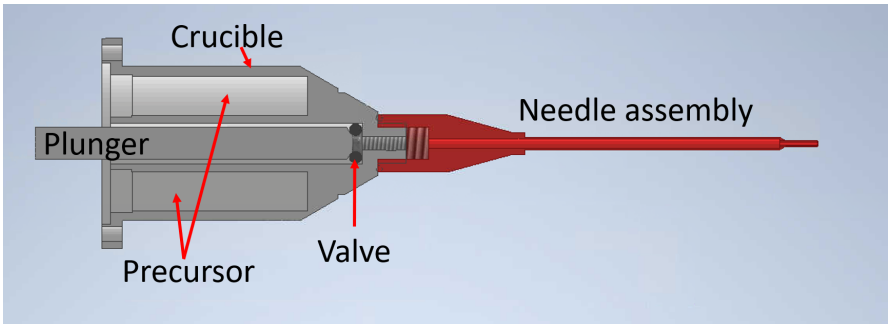

Figure 4.13: CAD drawing of the original GIS needle assembly along with the crucible and plunger.

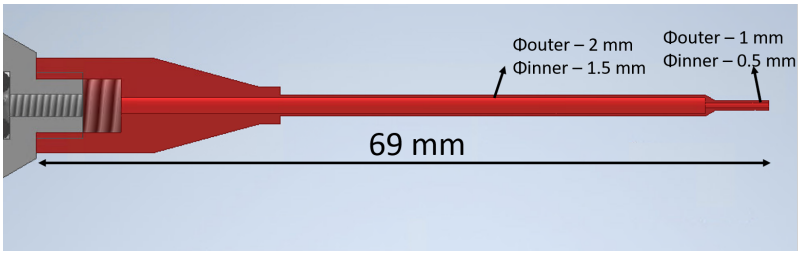

Figure 4.14: CAD drawing of the original GIS needle assembly showing the different dimensions.

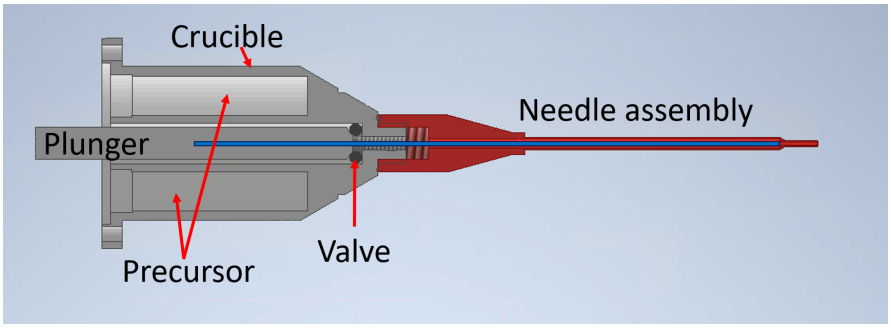

Figure 4.15: CAD drawing of the GIS needle assembly along with the proposed extension of the plunger (shown in blue).

valve. The arrowhead valve is made of PEEK to have a proper seal when it is in close position. The arrowhead is connected to an extension rod as shown in figure 4.17. The extension rod is made of Titanium grade 2, to have better thermal conductivity. The needle assembly with its dimension is shown in figure 4.18 The needle assembly is made of titanium grade 2. To fix the extension rod into the plunger, we need to modify the plunger. The modified plunger has been de-

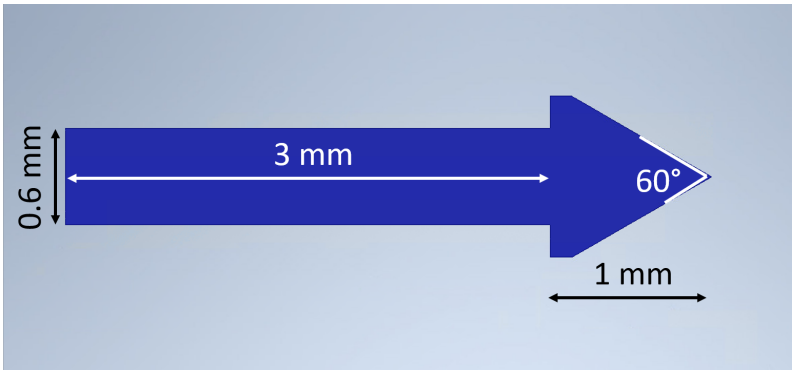

Figure 4.16: CAD drawing of the PEEK arrowhead valve with its dimension.

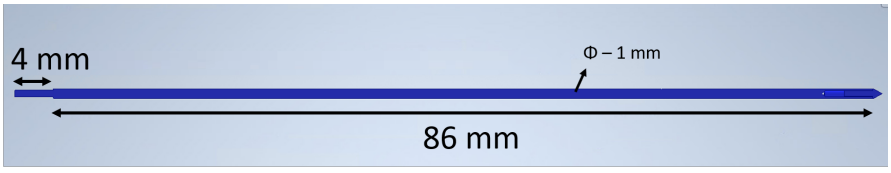

Figure 4.17: CAD drawing the extension rod along with the PEEK arrowhead fixed to it.

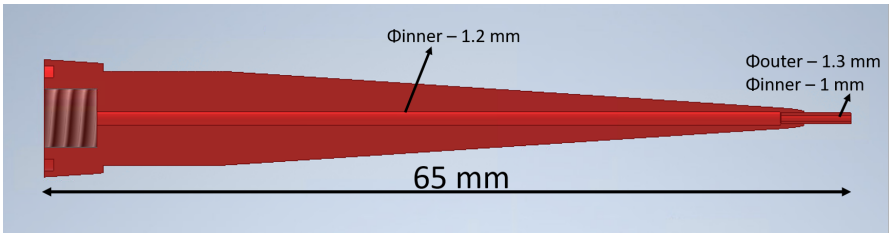

Figure 4.18: CAD drawing of the new modified needle assembly with its dimension.

signed to have a differential screw assembly to control the length of the extension rod. The modified plunger is shown in figure 4.19. A close-up of the differential screw assembly is shown in figure 4.20. The differential screw assembly is made of 2 set screws (M2.5 screw and M2 screw), a shaft made of titanium grade 2 and a spring. By moving the outer set screw (M2.5 screw in figure 4.20) inside the plunger, we can insert the extension rod further into the plunger valve. The complete CAD illustration of the new needle attached to the GIS is shown in figure 4.22.

Figure 4.21 shows the close-up view of the PEEK arrowhead valve near the nozzle. If we move the valve near the tip of the needle i.e., 6 mm away from the tip instead of 75 mm, this will result in a volume of 1.7 mm^3 and a surface area of

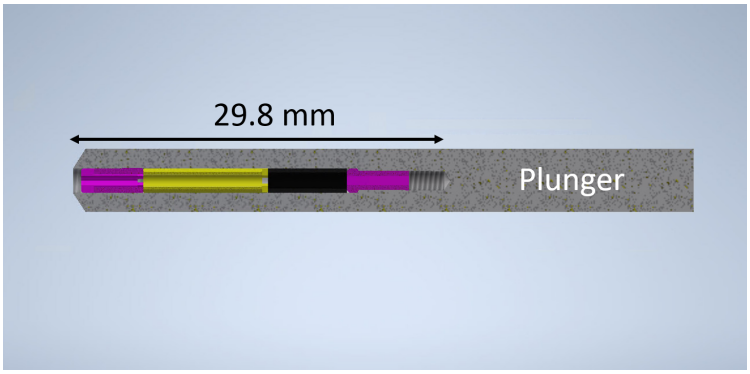

Figure 4.19: CAD drawing of the plunger along with the differential screw assembly.

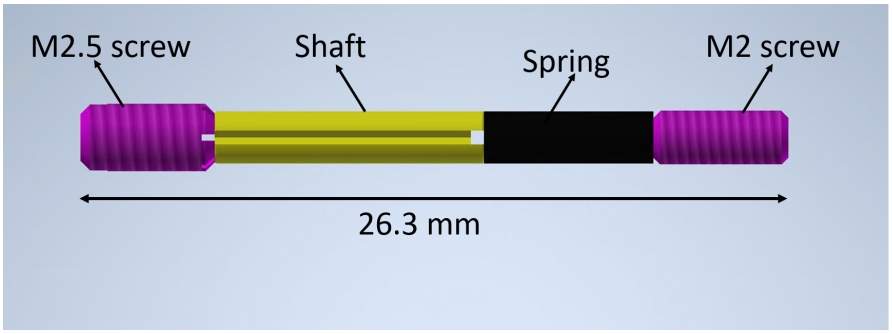

Figure 4.20: CAD drawing of the differential screw assembly used for positioning the extension rod.

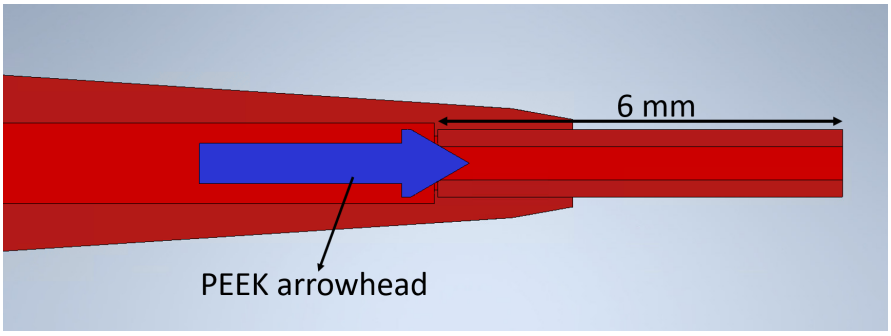

Figure 4.21: CAD drawing of the PEEK arrowhead along with the nozzle.

9.4 mm^2 after the valve. This should result in quicker pumpdown time for the Pt precursor.

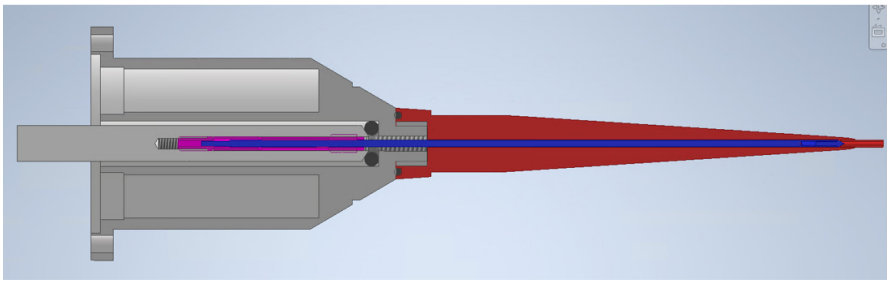

Figure 4.22: CAD drawing showing the complete GIS assembly with the modified needle.

4.7. FABRICATION AND ASSEMBLY

A plunger from a standard GIS was machined in a lathe to obtain the desired geometry shown in figure 4.19. The extension rod and the PEEK arrowhead were machined in a lathe to the desired specifications as shown in figure 4.17 and 4.16. The new needle was fabricated by EDM (electric discharge milling) as shown in figure 4.18, the conical shape was first fabricated by a sharpner tool. The inner threading, where the needle will be mounted to the GIS, was then machined and the channel in the needle was made by electrical discharge machining to get the required dimensions.

All the components of the GIS were thoroughly cleaned before being inserted into the SEM. The metallic parts were first cleaned in a beaker containing Acetone for 2 hours ultrasonically followed by blow-drying the components in dry air. The non-metallic parts were cleaned in a beaker containing ethanol for 2 hours followed by blow-drying in dry air. The arrowhead was glued to the extended plunger valve by using Stycast 1266. Stycast 1266 is vacuum compatible and heat resistant upto 200 ^{o}C. This was done so that the arrowhead didn't fall off onto the GIS needle blocking the flow of precursor into the SEM chamber. The plunger valve with the modifications was prepared by fitting it with the two set screws and the spring to have control of the plunger valve. The modified plunger valve was inserted into the standard GIS assembly from Thermo Fisher Scientific, after which we inserted the extended plunger with the arrowhead valve into the modified plunger. The extension rod is inserted such that outside the plunger there is length of 66.5 mm to have the valve closed. This was determined by mounting the GIS and testing the GIS with a gas flow. Then we fitted the new GIS needle made of Ti onto the GIS crucible. Finally, we mounted the GIS onto one of the GIS ports of the SEM chamber.

4.8. RESULTS AND DISCUSSION

We performed pump down measurements by letting in the Pt precursor for a duration of 1 second and noted down the time taken to reach a base pressure of 2.10^{-6} mbar. The result of this experiment is shown in figure 4.23, we observe an improvement of an order of magnitude to evacuate the chamber to the base pressure.

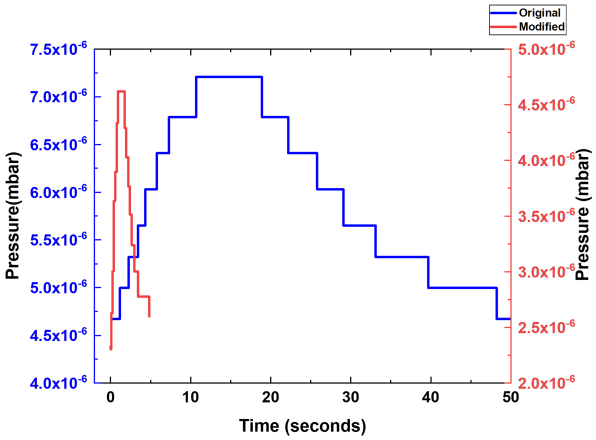

Figure 4.23: Graph showing the pump down curve for the original (blue) and the modified GIS (red) when the Pt precursor is let in for a duration of 1 second.

Needle configuration	Rise time (s)	Plateau (s)	Decay time (s)
Standard needle	9.5	8.5	29
Modified needle	0.6	1.3	2.5

Table 4.2: Table showing the time it takes for the platinum precursor to reach a maximum value, saturation time and time taken to reach the base pressure for the modified needle.

From table 4.2, we observe a reduction in time for all three regions of the pump-down curve. This validates our design to reduce the pump down time for the precursor. With a Pt dose time of 1 second, we should be able to have a pump down time of 5 seconds. We now modified the recipe for ALD to the one shown in figure 4.24. The control of the Pt precursor valve and the dry air was done manually. Even though we could reduce the Pt dosing time to 1 second and the Pt pump downtime to 5 seconds, we started with Pt dosing time of 10 seconds followed by a pump downtime of 25 seconds to ensure that we operate in the saturation regime of the ALD process. The Pt dosing and pump down time can be gradually reduced to extract the saturation curves of the ALD process. We car-

ried out an ALD process with the new recipe, we took a clean Si substrate with 1 x 1 cm dimensions and deposited Pt FEBID seed layers on it with a dose of 5 nC/μm^2 with the following parameters, 5 kV, 98 pA, 1μs dwell time, 382 passes and 2.74 nm pitch to pattern series of squares with 1 x 1μm^2 dimensions. The dose was mistakenly chosen as 5 nC/μm^2 instead of 0.05 nC/μm^2, resulting in a much thicker seed layer than intended. The Pt FEBID seed layers were also deposited on a control substrate. The ALD process was started once we reach a base pressure of 4 x 10^{-6} mbar. Also the GIS was heated for 2 hours before we began the process to ensure that the whole GIS (from the crucible to the nozzle) is at the same temperature. Here we use our heater V2, which can go upto 300 ^{o}C. With a temperature of 300 ^{o}C, the main difference from the previous experiment would be that the growth per cycle would be a bit higher. Once, the base pressure is attained, we ramp-up the temperature to 297 ^{o}C and bake the seed layers with a flow of dry air at 1.6 mbar line pressure for 20 minutes to purify the seed layers. The chamber pressure was 1.5 x 10^{-5} mbar. Immediately after the purification step, we carried out 25 cycles of ALD at 297 ^{o}C. Figure 4.25a shows an AFM scan over the deposited seed layer after the purification step, the inset picture shows the secondary electron image of the seed layer after purification. The seed layer shows a brighter contrast since imaging was done after purification, which results in a purer Pt layer. The AFM profile over the seed layer shows a rough profile as the carbon content in the seed layer is removed during the purification. After the ALD process, we observe a denser Pt layer and a smoother AFM profile.

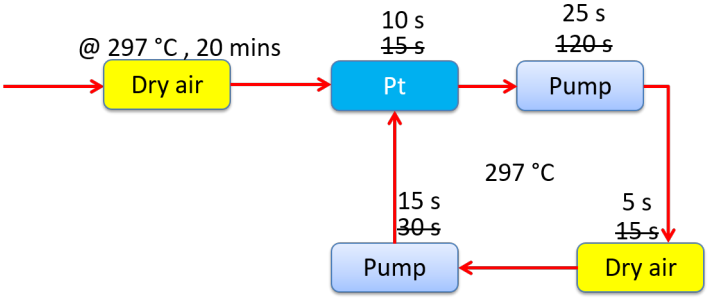

Figure 4.24: Modified recipe with the new valve.

Figure 4.25b shows the AFM scan over the seed layers after 25 cycles of ALD. The inset picture shows the secondary electron image of the layer after ALD. We observe a growth of 1.2 nm, which matches the expected growth at 25 cycles and 297 ^{o}C, confirming that we have ALD growth assuming a growth rate of 0.048 nm/cycle [1]. From the secondary electron image, we observe that the Pt seed

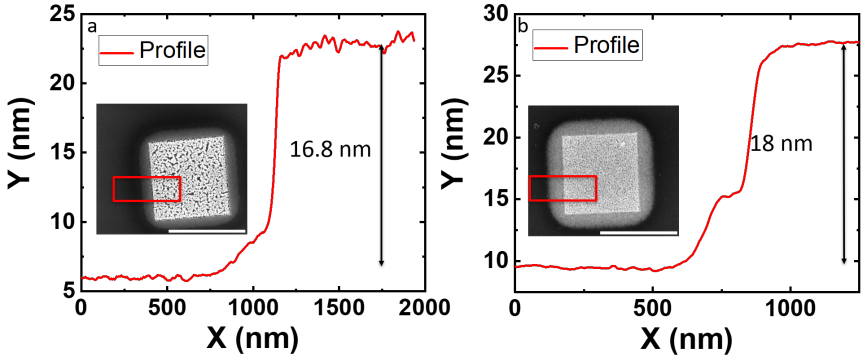

Figure 4.25: a) AFM profile of the seed layer, showing the noisier profile in the seed layer. Inset picture: SE micrograph showing the seed layer, the noisier profile in AFM is due to the voids in the seed layer. Scale bar is 1 μm. b) AFM profile of the layer after ALD, showing a smoother profile. Inset picture: SE micrograph showing the ALD layer, the smoother profile in the AFM is due to the ALD growth as seen. Scale bar is 1 μm.

layer deposited has a lot of voids due to the purification step which removes the carbon from the seed layer. After the ALD cycles, we observe a denser Pt depicting the growth. A single ALD cycle takes 55 seconds, but this is not the minimum possible duration as we manually operate the valves. By controlling the valves electronically, we can bring the ALD cycle time down to below 30s, a value comparable to a standard ALD tool. The ALD layer is too thin to carry out an EDX measurement to determine the purity of the layer.

4.9. CONCLUSION

To summarize, in this chapter we have demonstrated an in-situ ALD process in an SEM. We listed the requirements for in-situ ALD, described the choice of precursor and the co-reactant used, developed a recipe for ALD in SEM and performed area selective ALD using a direct-write method. We chose to demonstrate a Pt ALD process as the same precursor is used for FEBID. The seed layers are deposited using Pt FEBID. For the delivery of the co-reactant we used a modified GIS needle assembly to deliver gas to the substrate. We decided to go with dry air as the co-reactant because it was easier to implement due to safety concerns. We used the in-situ substrate heater V1 we developed to bring the substrate to the desired temperature of 241 ^{o}C. We designed the dosing and the purge time for the precursor and the co-reactant based on literature data and pump down experiments. We patterned Pt FEBID seed layers with different doses to estimate the minimum dose required for ALD growth. With the designed recipe, we car-

ried out 17 cycles of ALD. We observe a contrast reversal after 17 cycles of ALD. To further quantify the result, we measured the growth by an AFM. We measured the height of the seed layers after cleaning and height of the layers after 17 cycles of ALD. We observe a growth of 0.7 nm, this matches with the literature data for Pt ALD at 241 ^{o}C. Thus, we have demonstrated a working ALD in an SEM. Even though we have an in-situ ALD, a cycle duration is about 3 minutes long whereas a cycle duration in a standard ALD tool is only a few seconds. So, if we want to grow a 10 nm layer at 241 ^{o}C it will take us 13 hours. This is a serious disadvantage of the in-situ ALD. Therefore we aimed to reduce the cycle duration to under 30 seconds to make the in-situ ALD tool usable.

We suspected that the long purge time was due to the location of the valve in the standard GIS which is located at 7.5 cm away from the tip of the needle. This leads to the precursor getting adsorbed in the internal surface of the needle, causing the long duration. We decided to solve this by moving the valve closer to the tip of the needle at a distance of 6 mm away from the tip. This reduces the internal surface area behind the valve from 428 mm^2 to 9.4 mm^2 and the volume from 271 mm^3 to 1.7 mm^3. We designed a new GIS needle assembly that brings the valve closer to the tip of the needle. With the new design, we observe an order of magnitude in reduction in the pump downtime. We modified the earlier recipe for the new design and ensued that we operate in the saturation regime of the ALD process. We carried out 25 cycles of ALD with the new GIS and at a temperature of 297 ^{o}C in 43 minutes and we obtained an ALD growth of 1.2 nm matching the expected value from literature. In a standard tool, a single ALD cycle takes place within 30 seconds, whereas in our in-situ ALD process a single cycle takes about 55 seconds. We manually operated the valves for both the precursor and the co-reactant gases. In the future, both the valves should be controlled electronically to bring down the total cycle time under 30 seconds. From 4.23 we can reduce the pump down time, after Pt precursor injection for 1 second, to 5 seconds. With the above two ways, we can reduce the cycle time to values close to those of a standard tool.

REFERENCES

[1] H. Knoops, S. Potts, A. Bol, and W. Kessels, *27 - atomic layer deposition,* in *Handbook of Crystal Growth (Second Edition)*, Handbook of Crystal Growth, edited by T. F. Kuech (North-Holland, Boston, 2015) second edition ed., pp. 1101–1134.

[2] Mackus, A. J. M. and Bol, A. A. and Kessels, W. M. M, *The use of atomic layer deposition in advanced nanopatterning,* Nanoscale **6**, 10941 (2014).

[3] T. Aaltonen, M. Ritala, T. Sajavaara, J. Keinonen, and M. Leskelä, *Atomic layer deposition of platinum thin films,* Chemistry of Materials **15**, 1924 (2003), https://doi.org/10.1021/cm021333t .

[4] A. J. M. Mackus, N. Leick, L. Baker, and W. M. M. Kessels, *Catalytic combustion and dehydrogenation reactions during atomic layer deposition of platinum,* Chemistry of Materials **24**, 1752 (2012), https://doi.org/10.1021/cm203812v .

[5] A. J. M. Mackus, N. F. W. Thissen, J. J. L. Mulders, P. H. F. Trompenaars, M. A. Verheijen, A. A. Bol, and W. M. M. Kessels, *Direct-Write Atomic Layer Deposition of High-Quality Pt Nanostructures: Selective Growth Conditions and Seed Layer Requirements,* The Journal of Physical Chemistry C **117**, 10788 (2013).

[6] A. J. M. Mackus, S. A. F. Dielissen, J. J. L. Mulders, and W. M. M. Kessels, *Nanopatterning by direct-write atomic layer deposition,* Nanoscale **4**, 4477 (2012).

[7] A. J. M. Mackus, *Atomic layer deposition of Pt and its combination with electron beam induced deposition for the fabrication of nanostructures*, Master thesis, Eindhoven University of Technology (2009).

[8] G. D. Prima, R. Sachser, P. Gruszka, M. Hanefeld, T. Halbritter, A. Heckel, and M. Huth, *In situ conductance monitoring of Pt thin film growth by area-selective atomic layer deposition,* Nano Futures **1**, 025005 (2017).

[9] M. Utriainen, M. Kröger-Laukkanen, L.-S. Johansson, and L. Niinistö, *Studies of metallic thin film growth in an atomic layer epitaxy reactor using M(acac)2 (M=Ni, Cu, Pt) precursors,* Applied Surface Science **157**, 151 (2000).

[10] J. Hämäläinen, F. Munnik, M. Ritala, and M. Leskelä, *Atomic Layer Deposition of Platinum Oxide and Metallic Platinum Thin Films from Pt(acac)2 and Ozone,* Chemistry of Materials **20**, 6840 (2008), https://doi.org/10.1021/cm801187t .

[11] D. Vokoun, L. Klimša, A. Vetushka, J. Duchoň, J. Racek, J. Drahokoupil, J. Kopeček, Y.-S. Yu, N. Koothan, and C.-C. Kei, *Al2O3 and Pt Atomic Layer Deposition for Surface Modification of NiTi Shape Memory Films,* Coatings **10** (2020), 10.3390/coatings10080746.

[12] H. C. M. Knoops, A. J. M. Mackus, M. E. Donders, M. C. M. van de Sanden, P. H. L. Notten, and W. M. M. Kessels, *Remote Plasma ALD of Platinum*

and Platinum Oxide Films, Electrochemical and Solid-State Letters **12**, G34 (2009).

[13] A. J. M. Mackus, J. J. L. Mulders, M. C. M. van de Sanden, and W. M. M. Kessels, *Local deposition of high-purity Pt nanostructures by combining electron beam induced deposition and atomic layer deposition,* Journal of Applied Physics **107**, 116102 (2010).

[14] *Nano Analytik, AFM in SEM,* (Accessed on 02-08-2022), https://www.nanoanalytik.net/.

[15] M. Holz, C. Reuter, A. Ahmad, A. Reum, M. Hofmann, T. Ivanov, and I. W. Rangelow, *Correlative Microscopy and Nanofabrication with AFM Integrated with SEM,* Microscopy Today **27**, 24–30 (2019).

[16] J. F. O'Hanlon, *A user's guide to vacuum technology*, 2nd ed. (A Wiley - Interscience publication, 1989).

[17] M. G. Stanford, B. B. Lewis, J. H. Noh, J. D. Fowlkes, and P. D. Rack, *Inert Gas Enhanced Laser-Assisted Purification of Platinum Electron-Beam-Induced Deposits,* ACS Applied materials & Interfaces **7**, 19579 (2015).

5

IN-SITU SPUTTER ETCHING TOOL IN SEM

5.1. INTRODUCTION

In the previous chapters, we have demonstrated an in-situ substrate heater and in-situ area selective ALD in SEM for *Cleanroom in an SEM*. We chose to implement a sputter etching tool for pattern transfer as discussed in chapter 2.

A local sputter etching tool in an SEM was developed based on a DC microplasma source by Matra [1]. Microplasmas are plasma sources, whose dimension in at least one direction is less than 1 mm. Microplasmas can be operated in a wide range of pressures from sub-atmospheric to atmospheric [2]. Matra's tool was based on a DC micro plasma jet with an orifice gas nozzle, shown in figure 5.1 a. The orifice gas needle, shown in figure 5.1 b, is used to reduce the pressure in the SEM chamber. The plasma was created between the orifice gas nozzle and the substrate. The e-beam was used to ignite the plasma, which in turn reduced the breakdown voltage for the plasma generation. The disadvantage of Matra's local sputter etching tool was that it needed an additional turbo molecular pump and a rotary pump, to operate the SEM within its operating pressure, and substrate biasing [3]. Another miniature plasma source was developed by Miyazoe et al. Miyazoe's design was based on an ultra-high frequency (UHF) microplasma jet [4]. It also required a 15 kV high voltage to ignite the plasma and the substrate was biased between −30 V and 20 V. The UHF microplasma jet was used as a local source of ions and radicals for in-situ charge neutralization of insulating materials and improving the metallic content of EBID layers [4] [5]. The plasma was operated at pressures of 10^{-5} mbar to 10^{-3} mbar. Miyazoe et al. reported no effect on the electron beam due to the operation of the plasma source

even though the plasma is operated by a UHF source. The disadvantages of the UHF microplasma jet are the UHF source to generate the plasma, the matching circuit required for the UHF source, the high DC voltage source required to ignite the plasma and substrate biasing. A low energy argon ion source was developed by Mulders et al [6]. Mulder's source was based on electron impact ionization of Ar gas delivered by a specially made GIS. The GIS was modified to deliver Ar gas from outside and a slotted nozzle in the needle allowed for the electron beam to impact Ar to generate ions by electron impact ionization. The substrate was biased to attract the Ar ions. The low energy Ar ion source was used to remove halos from EBID deposition, to transfer an EBID etch mask to an underlying gold film and to obtain artifact free STEM imaging [7][8][9][10]. The disadvantage of this ion source for sputter etching was that it required substrate biasing and that the source was mounted at an angle with respect to the substrate.

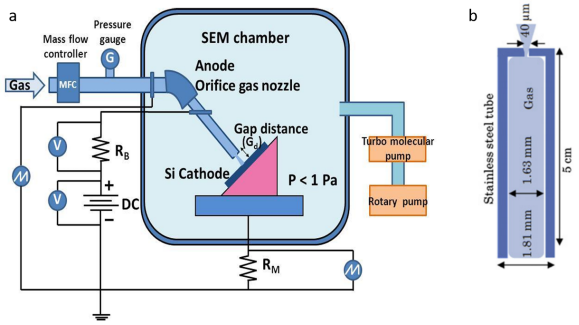

Figure 5.1: a) Schematic drawing of the miniature plasma source developed by Matra [1]. b) Schematic drawing of orifice gas needle. Copyright (2013), with permission from Elsevier

As discussed in chapter 2, sputter etching operates at pressures of 1 to 10^{-3} mbar whereas an SEM operates between 10^{-6} and 10^{-5} mbar. The plasma can be operated by different power sources such as DC, RF and UHF. This leads us to several requirements to implement a miniature plasma source in the SEM. The various requirements are discussed in the next section.

5.2. REQUIREMENTS FOR THE PLASMA SOURCE

When we add the miniature plasma source to an SEM, it shouldn't affect the normal operation of the SEM i.e., we should be able to use the SEM for inspection. This criterion, in addition to the restrictions mentioned in chapter 2, leads us to several requirements for implementing the add-on miniature plasma source for sputter etching. The requirements are:

1 The sputtering angle of incidence should be 0 degrees to the normal of the

substrate, so we can use it for pattern transfer.

2 The plasma power source shouldn't disturb the electron beam.

3 During plasma operation, the chamber pressure should be kept between 10^{-6} and 10^{-5} mbar.

4 The voltages used for the plasma source should be kept low (preferably < 1 kV) to avoid any flash overs inside the SEM.

5 The plasma source should occupy a minimum floor space in the SEM, as there is little available space in the SEM.

6 All materials used should be non-magnetic.

7 All materials used should be vacuum compatible and have low outgassing.

8 If insulating materials are used, they should be shielded from the direct line of sight of the electron beam.

9 No additional pump should be needed.

5.3. DESIGN OF A MICROPLASMA SOURCE IN A VACUUM SETUP

The plasma source needs to be designed such that the chamber pressure remains within the operating limits. An increase of the chamber pressure beyond $9 * 10^{-5}$ mbar will trigger closing of the valve between the gun area and the optical column and specimen chamber. This can be achieved by having a high pressure miniature chamber where the plasma is ignited and sustained, and an orifice which will limit the gas flow into the chamber which will limit the chamber pressure. The base pressure of the SEM is normally in the range of 10^{-6} mbar. The Knudsen number gives the type of gas flow through the orifice.

$$K_n = \frac{\lambda}{d} \tag{5.1}$$

where λ is the mean free path of the gas in m and d is the diameter of the flow channel in m[11]. The mean free path λ is given by,

$$\lambda = \frac{k.T}{\sqrt{2}.\pi.p.d_m^2} \tag{5.2}$$

where k is the Boltzmann constant, T is the temperature in K, p is the pressure in Pa, d_m is the diameter of the atom or molecule in m[11]. For Argon, with a diameter of 3.4 Å and with a pressure of 5 mbar the mean free path is $1.6.10^{-5}$ m. With an orifice diameter of 50 μm, we obtain a value of 0.3 for the Knudsen number. For $K_n < 1$, the type of flow is in a transition regime. The flow conductance for an orifice in the transition regime can be found empirically using the following equation [12][13],

$$\frac{C_F}{C_0} = \left(\alpha + \frac{0.4733 + 0.907z^{0.5}}{1 + 10.4z + 16.1z^2}\right) \tag{5.3}$$

where C_F is the flow conductance, z is given by,

$$z = K_n.\left(\alpha + 0.125e^{-0.5(12\alpha - 11.2)^2} + 0.18e^{-14.7\alpha} - 0.08\right)^{-1} \tag{5.4}$$

5

and α is given by the following equation,

$$\alpha = \frac{1}{0.996 + .94\left(\frac{L}{d}\right)^{0.94}} \tag{5.5}$$

where L is the length of the orifice in m and d is the diameter in m. C_0 is the conductance of an orifice in the molecular flow regime[11],

$$C_0 = \frac{\nu.\pi.d^2}{4} \tag{5.6}$$

where d is the diameter of the orifice in m and ν is the mean thermal velocity[11],

$$\nu = \sqrt{\frac{8.k.T}{\pi.m}} \tag{5.7}$$

The gas throughput Q_{or} through the orifice can then be found using the following equation[11],

$$Q_{or} = P_{Ar}.C_F \tag{5.8}$$

where P_{Ar} is the Argon pressure. The increase in chamber pressure due to an Argon influx can be calculated from the following equation,

$$P_{increase} = \frac{Q_o + Q_{or}}{S_{eff}} \tag{5.9}$$

where Q_o is the gas throughput without any Argon flow and S_{eff} is the effective pumping speed of the turbomolecular pump connected to the vacuum system.

The base throughput when no Argon flows through the orifice can be calculated as,

$$Q_o = S_{eff} * P_{chamber} \tag{5.10}$$

The high vacuum test setup is connected to a water cooled Pfeiffer TPH/U 180 HM turbomolecular pump (TP). The pump is connected to the vacuum setup by means of a pipe with a 90 degree bend. The effective pumping speed of the pump would be lower than the actual speed of the pump, because we connect the pump to the chamber by means of a pipe with a 90 degree bend. For estimating the rise in pressure due to the introduction of Argon gas into the chamber, we use the effective pumping speed of 70 l/s which is the value for a Nova nanoLab 650[14] as an approximation. With an average thermal velocity of 392 m/s for Ar at room temperature, a base pressure of $1.1 * 10^{-6}$ mbar, and an orifice diameter, d_o of 50 μm we can estimate the expected increase in chamber pressure for an input of Argon pressure. With an input Argon pressure of 5 mbar to 70 mbar, the expected chamber pressure is in the range of $8.3 * 10^{-6}$ to $8.5 * 10^{-5}$ mbar. An orifice diameter of 50 μm satisfies the chamber pressure requirement. If we assume the metal plate containing the orifice to be 100 μm thick, then, for a substrate kept at 1 mm away from the orifice, we should expect Ar atoms in the radius of 550 μm at the substrate assuming no electric fields. So we have a sufficient radius of Ar impingement for the pattern transfer. We are also limited by the space available in the SEM, so the plasma source should be compact. We should choose a DC power based plasma source to operate the plasma source without disturbing the electron beam, even though we won't be operating the electron beam at the same time. The voltages needed to ignite and operate the plasma source should be kept low to avoid unwanted breakdown in the SEM chamber. From the requirements, it is clear that we need to choose a geometry such that the sputtering angle of incidence is 0 degrees. A schematic of the miniature plasma source is shown in figure 5.2.

It consists of a metal tube with an inner diameter of 4 mm, which is used to deliver Ar. The tube ends by making contact with a metal grid. The metal grid is used to create a plasma across the whole diameter of the grid. After, the metal grid we have a small compartment enclosed by the orifice. The small compartment acts as the plasma chamber. The plasma is ignited and sustained between the grid and the orifice disc. The distance between the metal grid and the orifice disc is kept at a distance of 0.5 mm. An insulator is used to electrically isolate the two electrodes. The orifice restricts the gas throughput to the vacuum chamber thereby restricting the rise in chamber pressure. By choosing a diameter of 50 μm for the orifice we would satisfy the requirement of keeping the chamber pressure between 10^{-6} and 10^{-5} mbar. The substrate is kept at a certain distance from the orifice disc. A potential is applied between the metal tube in contact with

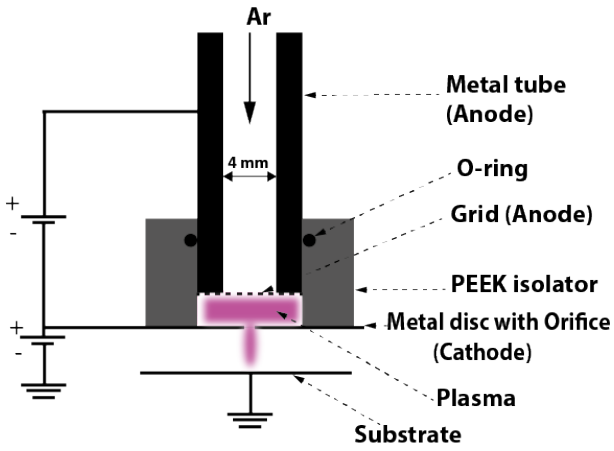

Figure 5.2: Schematic drawing of the miniature plasma source.

the metal grid (anode) and the orifice disc (cathode) to ignite and sustain the plasma. The substrate is kept grounded to avoid biasing the substrate in the final design in the SEM chamber. Also, the orifice disc is raised to a positive potential to accelerate the positive Ar ions created in the plasma chamber. The potential applied to the electrodes is kept below 1 kV keeping in line with the requirement. Figure 5.3 shows the electric circuit used to apply the potentials and also to measure the voltage drops across the electrodes and the current flowing through the plasma chamber. Since the voltage range in a multimeter is limited, we implement a voltage divider using the resistors R_1 and R_M to measure the voltage of the anode. Similarly to measure the voltage of the cathode we use the voltage divider using the resistors R_2 and R_M (R_M is the impedance of the multimeter). A picoammeter (I) was used to measure the plasma current within the plasma chamber. In addition, to keep the substrate grounded, we raised the potential of the orifice disc using a battery with a maximum voltage of 250 V. The battery pack is adjustable from 25 V to 250 V. This is implemented such that Ar ions are directed towards the substrate. To measure the substrate current at the substrate, a picoammeter was connected between the substrate and the ground. The measured plasma current (I_{Ar}) would be a combination of the ion current (I_{ion}) and the electron current ($I_{electron}$).

$$\begin{aligned} I_{Ar} &= I_{ion} + I_{electron} \\ I_{Ar} &= I_{ion} + \alpha.I_{ion} \\ I_{Ar} &= (1+\alpha).I_{ion} \end{aligned} \tag{5.11}$$

where α is the number of electrons being stripped off from the Argon atom. The ion current in the orifice I_b is defined as,

$$I_b = \frac{d_o^2.I_{Ar}}{d_{plate}^2}$$
$$I_b = \beta.I_{Ar} \tag{5.12}$$

where β is a geometric factor depending on the orifice diameter (d_o) and the orifice plate diameter (d_{plate} = 5.5 mm). The substrate current I_{etch} measured at the substrate is defined as,

$$I_{etch} = I_b + I_{Se^-}$$
$$I_{etch} = I_b + \gamma.I_b \tag{5.13}$$
$$I_{etch} = (1+\gamma).I_b$$

where I_{Se^-} is the ion induced secondary electron current and γ is the ion induced secondary electron yield. For a Au film with an Ar ion of energy 250 eV we would have a γ of 0.12 [15].

For such a design, the potentials are shown in figure 5.4. Ar ions created in the plasma chamber will get attracted to the grounded substrate. The field from the plasma chamber extends into the orifice, causing a focusing effect.

A Paschen curve provides the breakdown voltage as a function of the product of the pressure and the electrode distance. By plotting the Paschen curve for the designed microplasma source, we would be able to determine the gas pressure required to sustain the plasma while keeping the electrodes at a low potential.

The sputtering rate of a target material is given by,

$$\frac{z}{t} = \frac{M * S * j_p}{\rho * N_a * e} \tag{5.14}$$

where M the molar weight of the target material in kg/mol (0.197), S is the sputtering yield of the target (0.7 for Au), j_p is the current density of the ions in A/m^2, ρ is the density of the target material in kg/m^3 (19.3 for Au), N_a is the Avogadro number, e is the electron charge and z is the sputtered thickness in time duration t in seconds. For example, if we have an substrate current I_{etch} of 1 nA (I_b = 0.89 nA) with an etch diameter of 25 μm we would have an etch rate of 8 nm/min for a film of Au using equation 5.13.

5.4. FABRICATION AND ASSEMBLY

We chose a design based on a DC microplasma source. A piece of standard 1/4“ stainless tubing (inner diameter of 4 mm) was used as the anode and also to deliver Ar gas. An electrically insulating cylinder made out of PEEK [16] was fitted around the tube. A metal grid (made of tungsten which was easily available) is

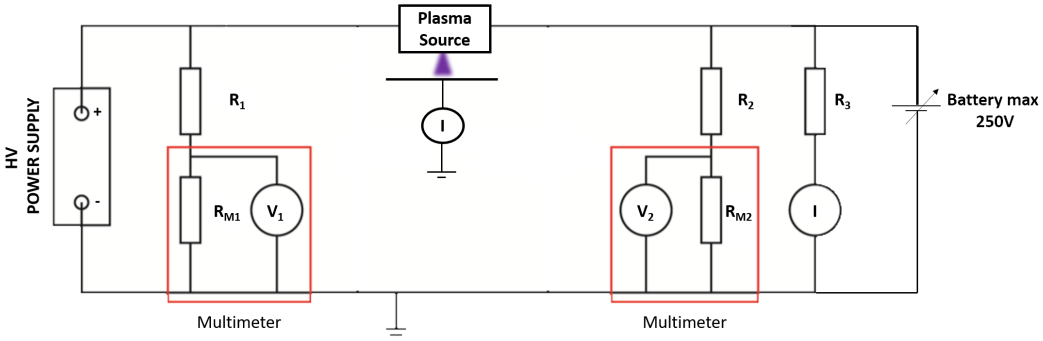

Figure 5.3: Schematic drawing of the electrical circuit used to apply the potential between the electrodes and also to measure the voltage drops and the current.

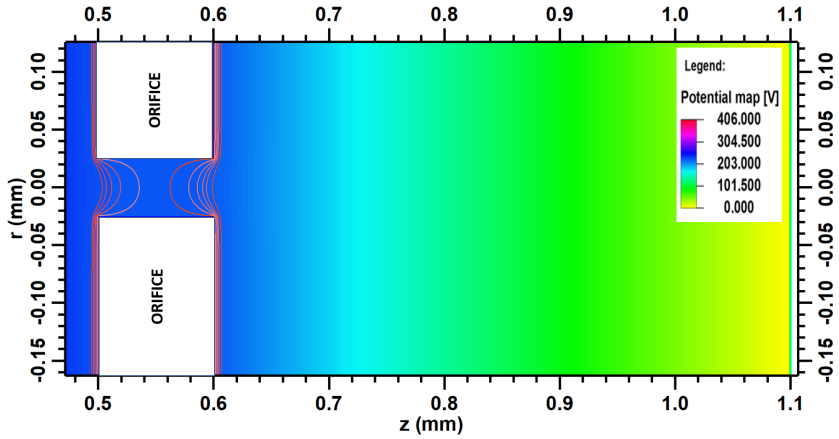

Figure 5.4: EOD simulation showing the electric potentials between the orifice disc (maintained at 225V) and a grounded substrate kept at a distance of 0.5 mm. The grid (maintained at 406V) is not visible as it is positioned 500 μm to the left of the orifice. The potential lines near the orifice are displayed as vertical lines. The potential map values are shown in the legend.

placed inside the PEEK cylinder, making electrical contact to the stainless steel tubing, i.e. the anode. The cathode consists of a 100 μm thick plate made of phosphor bronze with an orifice of 50 μm in diameter in the center. We decided to use phosphor bronze as it is vacuum compatible and non-magnetic. The hole was drilled by using a laser. The orifice disc (cathode) is glued to the end of the PEEK insulator using vacuum compatible double sided Kapton tape from Accu-Glass products[17]. The distance between the tungsten grid and the orifice disc is 500 μm, this is achieved by the PEEK insulator as it has a notch which keeps

the anode from making electrical contact with the cathode. We can control the pressure in the plasma chamber by controlling the line pressure of the gas supply (Ar) delivered through the cathode tube. The metallic components were cleaned ultrasonically in a beaker containing acetone for 2 hours followed by cleaning ultrasonically in a beaker containing ethanol for 2 hours. Finally, the components were blown dry by using Nitrogen gas. The non-metallic parts were cleaned ultrasonically in a beaker containing ethanol followed by blow drying them in Nitrogen gas. The microplasma source was mounted onto a vacuum setup shown in figure 5.5, consisting of a 6-way cross with CF150 flanges. The left flange (in figure 5.5) contains a manipulator with 1 degree of freedom which is used to position the substrate under the plasma source. The bottom flange is connected to a turbomolecular pump and a scroll pump as the pre-pump. On the top flange, a translation manipulator with 4 degrees of freedom is used to position the plasma source in X,Y,Z and rotation around the Z-axis. The top flange also has multiple CF16 flanges, one of which is used as a gas feedthrough to deliver Ar. Two MHV (medium high voltage) feedthroughs are used to supply the voltages to the source. A FUG high voltage power supply is used to deliver the voltage. In figure 5.3, $R1$=$R2$=100 MΩ, and $R3$ = 1 MΩ. V1 and V2 are a Fluke 8840A digital multimeter (R_{M1} = 10 MΩ) and a voltcraft M-4660A multimeter (R_{M2} = 10 MΩ) respectively. The plasma current is measured using another voltcraft M-4660A multimeter, whereas the current at the substrate is measured using a Keithley 6485 picoammeter. Two PEEK coated wires are used to connect the electrodes and the electrical feedthroughs. Ar gas is delivered using a Bronkhorst EL-PRESS pressure controller (1 mbar - 1000 mbar) [18].

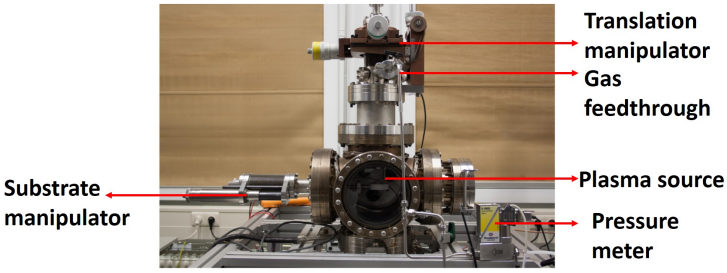

Figure 5.5: Photograph of the vacuum setup used to test the prototype microplasma source.

5.5. PERFORMANCE TESTS IN VACUUM SETUP

The initial test was to determine whether the plasma source can sustain a plasma while keeping the chamber pressure at SEM operating pressure. Initially the Ar

inlet pressure, i.e. the pressure in the plasma chamber between the two electrodes, was kept at 5 mbar resulting in a chamber pressure (P_{Ch}) of $3.6 * 10^{-5}$ mbar, while increasing the voltage between the electrodes until a current between the electrodes is observed. Figure 5.6 shows the measured and the calculated chamber pressure for various input Argon pressures. The observed difference between the calculated and the measured values could be explained by the leaking of Ar gas through the double sided tape. A plasma current of 5 μA was observed at the breakdown voltage. A photograph of the observed plasma is shown in the inset of figure 5.7 (the blue dot in the centre). Subsequently the Paschen curve (breakdown voltage versus product p.d of pressure p and electrode distance d) was measured by varying the inlet pressure from 2 to 200 mbar and recording the voltage at which breakdown was observed. The measured Paschen curve is shown in figure 5.7. From the graph, we can determine the pressure where we can ignite and sustain the plasma while keeping the voltages low. We observe an outlier at a p.d of 4, this could be due to the geometry of the plasma source, a cathode plate to an anode grid instead of two parallel plates. This irregular geometry could lead to higher electric fields. While recording the Paschen curve the chamber pressure was registered. It varied from $9 * 10^{-6}$ mbar to $1 * 10^{-3}$ mbar.

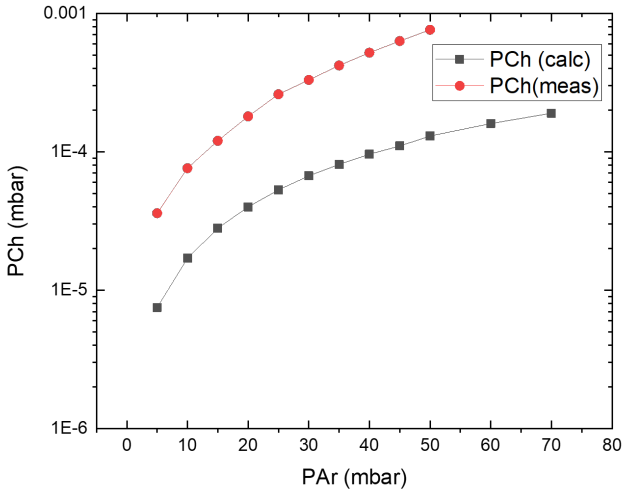

Figure 5.6: Graph showing the measured chamber pressure (PCh(meas)along with the calculated chamber pressure (PCh(calc)) using equation 5.3 for different input Argon pressures (PAr) for the test vacuum setup.

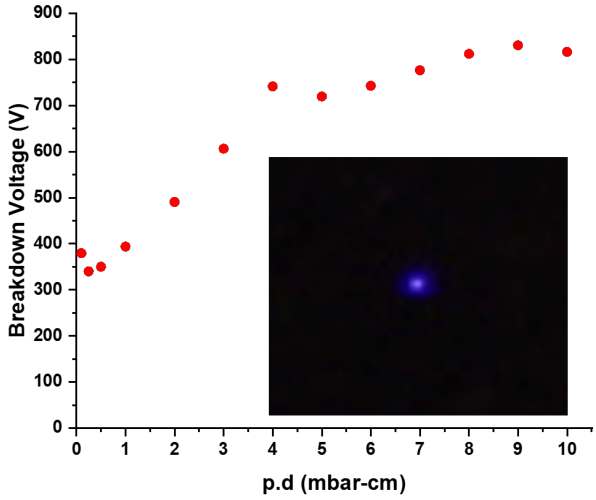

Figure 5.7: Graph showing the measured Paschen curve with a constant electrode spacing of 0.5 mm. Inset photograph showing the observed plasma.

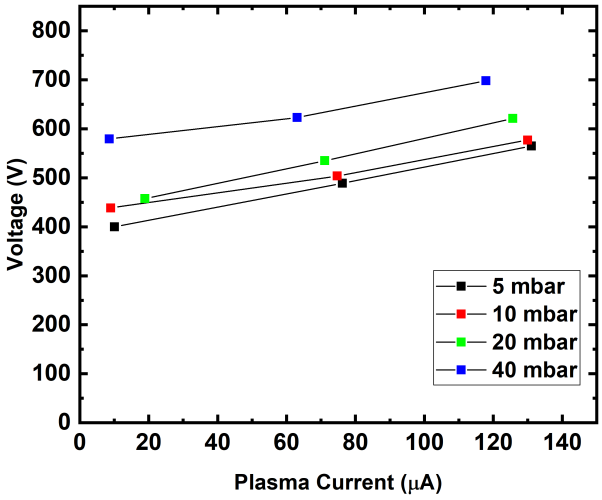

Figure 5.8: Measured IV curves for the miniature plasma source at varying P_{Ar}.

We measured the current-voltage (IV) characteristic of the plasma source. Ar gas with a line pressure P_{Ar} of 5 mbar was let into the chamber, after which we

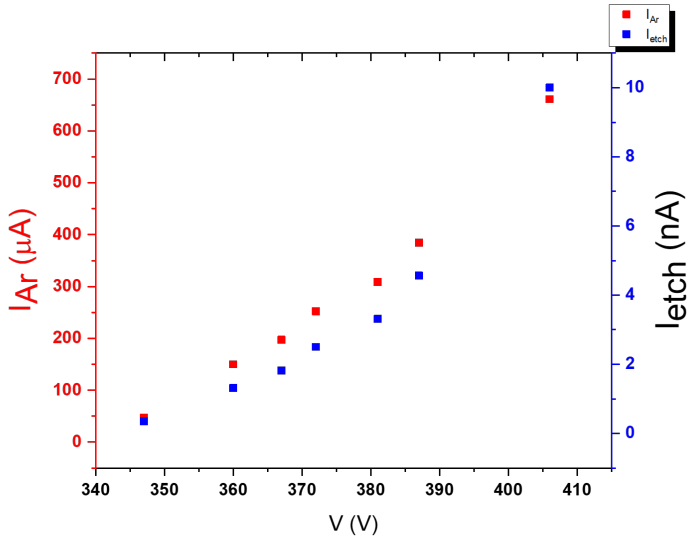

Figure 5.9: Graph showing the plasma current (I_{Ar}) and the substrate current (I_{etch}) as a function of the voltage between anode and cathode of the plasma chamber, while operating the plasma source at a pressure of 5 mbar and a potential of 250 V at the orifice disc.

started to increase the potential between the electrodes of the plasma source. Once we obtained a plasma, we varied the potential between the electrodes and measured the plasma current (I_{Ar}) flowing between the electrodes. The plasma currents are plotted as a function of the measured potential drop between the electrodes, kept at a distance of 0.5 mm, shown in figure 5.8 for different Ar pressures.

Now, we have achieved our goal of sustaining a plasma at SEM operating pressures. In the SEM, the substrate is generally grounded. So, to avoid biasing the substrate, we decided to raise the potential of the orifice plate while keeping the substrate grounded. This should result in the Ar ions being accelerated towards the substrate. Once we obtain a plasma, we applied a potential of 250 V to the orifice disc and measured the current flowing at the substrate. Figure 5.9 shows the IV curve for the plasma source along with the substrate current I_{etch} measured at the substrate for an Ar pressure of 5 mbar. If we compare the plasma current (I_{Ar}) in figures 5.8 and 5.9, we observed a big increase in Iar. This increase could be due to the biasing of the orifice disc (+250 V), as the Ar ions are accelerated towards the orifice disc. Moreover, the sealing of the orifice disc was improved before we biased the orifice disc.

Even though we have a plasma current, I_{Ar} in hundreds of μA range, the sub-

strate current, I_{etch} is in the nA range. The current (I_{etch}) we measure is a combination of the ion current, electron current and current from the ion induced secondary electron emission process as shown in equations 5.11, 5.12 and 5.13. For an I_{Ar} of 385 μA, we measured an I_{etch} of 4.56 nA. The plasma exposed diameter on the orifice plate is about 5.5 mm and the orifice diameter is 50 μm. Using equations 5.11, 5.12 and 5.13 with an α of 1, the estimated substrate current I_{etch} is 17.8 nA. But on the substrate we measured a current of 4.56 nA. So we have an ion current of 4 nA delivered to the substrate, out of the available 17.8 nA. The orifice disc has a thickness of 100 μm with a diameter of 50 μm, there will be additional scattering of the Ar ions along the length of the orifice disc. The reduction of the ion current from the expected value might be due to this scattering in the orifice disc length.

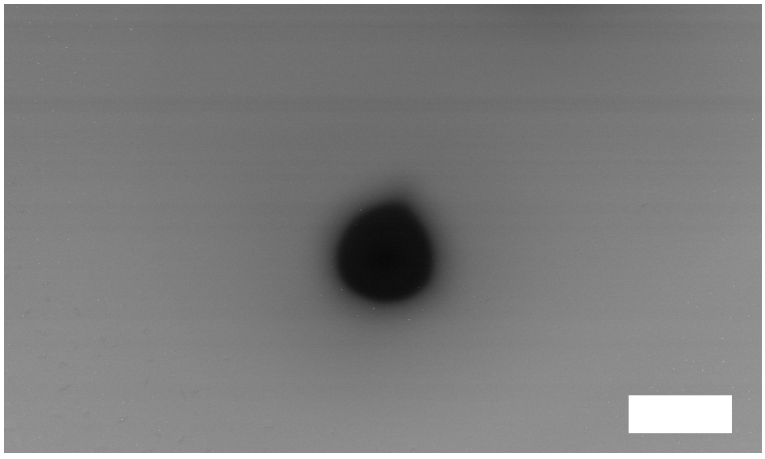

Figure 5.10: SE image of the etch spot (dark area) on a 20 nm Au film on Si. The scale bar is 200 μm.

We replaced the orifice disc with another one which had a diameter of 75 μm and a thickness of 100 μm. This was done, as the original orifice disc had a leak which affected the chamber pressure. Based on the geometry, we can use the triangle proportionality law to determine the expected etch diameter at 1 mm to be 750 μm. This doesn't take into account any fields or scattering. Next, we tested the plasma source as a sputter etching tool. We chose a Si wafer coated with a 20 nm thick Au film as the substrate and placed it at a distance of 1 mm from the plasma source. The substrate was exposed to the plasma for 20 minutes, while keeping the orifice disc at a potential of 225.5 V and at a P_{Ar} of 5 mbar. We measured an I_{Ar} of 399.4 μA at a voltage of 390 V and an I_{etch} of 5.89 nA with a P_{Ch} of $4.5 * 10^{-5}$ mbar. When we observed the exposed area in an SEM, we observed an etch spot (dark area) with a diameter of 200 μm shown in figure 5.10. This etch

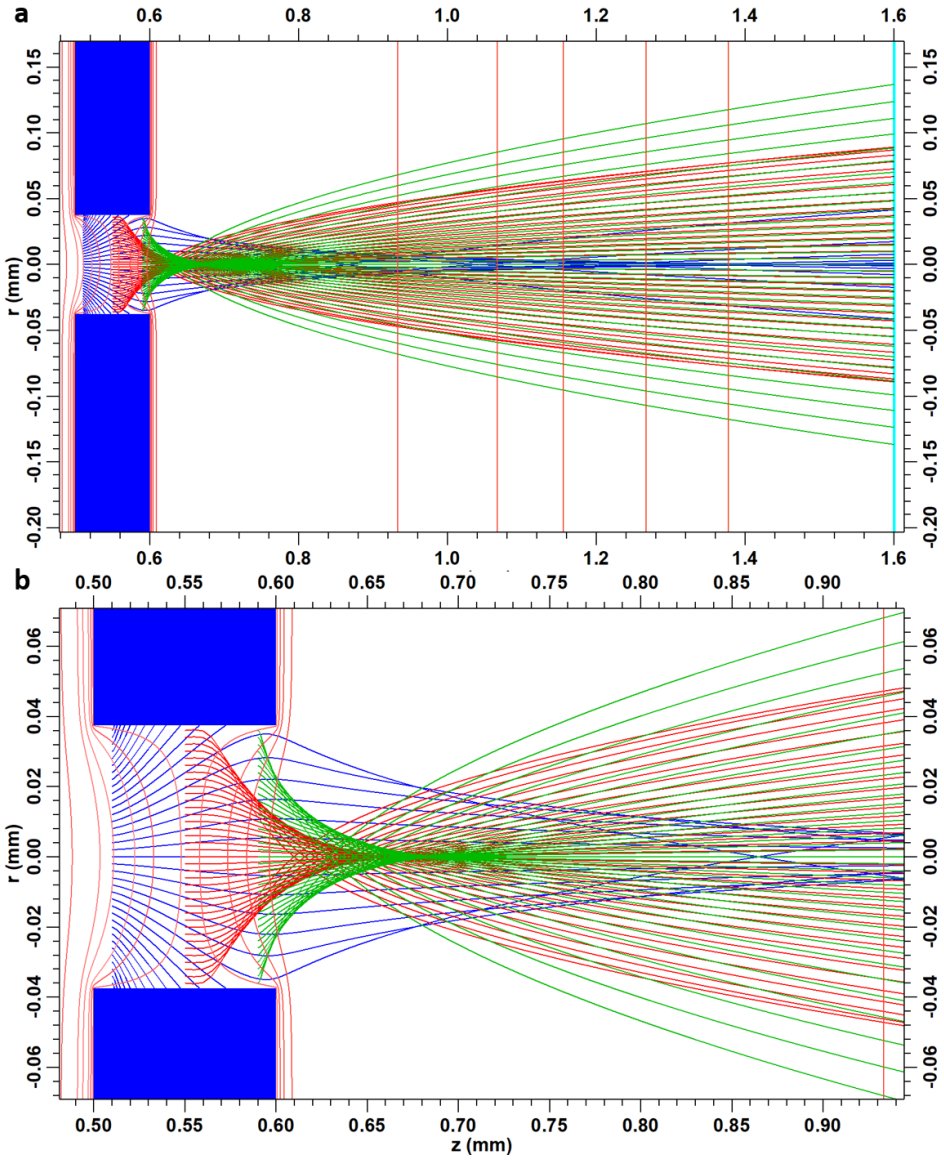

Figure 5.11: a) Ar ion trajectories for the high vacuum setup with an orifice disc diameter of 75 μm and with an initial energy of 25 meV at three different locations: 10 μm from the start of the orifice (0.51 mm, shown in blue colour), at center (0.55 mm, shown in red colour) and at 10 μm from the end of the orifice (0.59 mm, shown in green colour). Ar ions starting closer to the end of the orifice are focussed. b) A close-up image of the Ar ion trajectories in the orifice.

spot of 200 μm is much smaller than our estimate from geometry. This could be

explained by the effect of voltage at the orifice disc. To explain the effect of field created by the orifice disc, we simulated the Ar ions trajectories using a finite element simulation package EOD [19]. For the ray tracing of Ar ions, we kept the energy of Ar ions at 25 meV, as the microplasma source is a non-thermal plasma where temperature of the ions is around room temperature. 19 Ar ions were injected towards the substrate by equally spacing them at three different locations at 10 μm from the start of the orifice (0.51 mm, shown in blue colour), at center (0.55 mm, shown in red colour) and at 10 μm from the end of the orifice (0.59 mm, shown in green colour) as shown in figure 5.11. Due to such low energy, we can assume that there will be no secondary ions generated along the orifice thickness. All Ar ions that make it out of the orifice are focussed with a different focal distance and after that they spread out again. And the Ar ions near the center of the orifice pass through without any deflection. To correctly estimate the diameter of the beam, we would need to inject ions at all possible locations in the orifice and in all directions. Then, calculate the full width 50 %. If we take the outermost ions from figure 5.11, we would arrive at a diameter of 280 μm which is larger than the observed etch diameter. If we take into account only the ion trajectories at 0.51 mm and 0.55 mm, we estimate an etch diameter of 180 μm which is closer to the observed etch diameter. The observed deviation between the simulation and experiment could be due to the interaction of ions with the neutrals which could scatter the ions further from the optical axis resulting in a bigger diameter. Also, the simulation was conducted with certain limitations, including the restriction that trajectories were initiated only in the direction of the substrate, and at predefined positions. Additionally, the FW50% was not determined.

From equation 5.14, with I_{etch} = 5.89 nA we obtain a sputter rate of 1 nm/min. So, we would completely etch a 20 nm film of Au in 20 minutes as shown in figure 5.10. With a measured I_{Ar} of 399.4 μA and assuming an α of 1 using equations 5.11, 5.12 and 5.13, we should have a current I_{etch} of 41.5 nA. We measured a current of 5.89 nA, so the ion current alone would be equal to 5.26 nA, this deviation could be due to the approximate nature of the calculations. It could also be due to the scattering of the Ar ions along the thickness of the orifice disc and could be due to the scattering of Ar ions with neutrals while the ion travels from the orifice to the substrate. In our estimation of the substrate current I_{etch} we assumed a value of 1 for the α. In reality, there could be 2 electrons ejected out of the Ar atoms during ionization. If we assume an α of 2, we would arrive at a I_{etch} value of 27.7 nA. We could have a situation where we have a mix of α at 1 and 2 [20][21]. We do have now demonstrated a miniature plasma source which can be used for sputter etching in a standalone vacuum system. This miniature plasma source now needs to be implemented inside an SEM.

5.6. SUMMARY OF THE PROTOTYPE MICROPLASMA SOURCE IN A VACUUM SETUP

In the prototype microplasma source setup, we were able to demonstrate the operation of a plasma source at SEM operating pressures of 10^{-6} to 10^{-5} mbar. We were also able to keep the voltages required to operate the plasma under 500 V. We demonstrated a microplasma source with an angle of incidence of 0 degrees to the substrate normal. Finally we were able to etch a Au film on top of a Si substrate, utilizing the microplasma source as a sputter tool. The diameter of the plasma chamber for our prototype device is kept at 5.5 mm and the electrodes are separated at a distance of 0.5 mm. We have an etch area with a diameter of 200 μm. Since we didn't carry out a profilometer measurement over the etch spot, we don't know the etch uniformity.

5.7. DESIGN OF A MICROPLASMA SOURCE IN AN SEM

The prototype miniature plasma source in the high vacuum setup cannot be directly placed in the SEM. The plasma source is still large compared to the available space in the SEM. In normal use of the SEM, the sample is kept at a distance of 5 mm from the pole piece. In the high vacuum setup, a 1/4 inch stainless steel tube was used to deliver Ar, and was also used as the anode for the source. We also used a tungsten grid at the end of the tube to act as the anode.

Figure 5.12 shows the interior of the SEM chamber from the view point of the chamber door, the overall picture of the SEM can be found in figure 2.8. We have several GISes present in the SEM, which deliver a precursor gas above the substrate, and with our modified GIS needle described in the previous chapter we can deliver an external gas above the substrate. The angle of incidence of the gas depends on the port used. Also, the distance between the needle and the substrate is in the range of 75 - 200 μm. One of the requirements for the plasma source is that the angle of incidence of the ions should be zero degrees to the normal of the substrate for reliable pattern transfer. Due to the little available space (5 mm between the pole piece and the substrate) and the angle of incidence requirement the possibility of using one of the GIS ports is not possible. The stage of the Nova nanoLab SEM can be positioned in X-Y direction up to ± 75mm with an accuracy of ± 1 μm. By having the plasma source suspended away from the beam axis, we would have an error of approximately ± 1 μm from the translation of the stage. From our test setup, we observe an etch area with a diameter of 200 μm. The translation error of the stage is far less than our etch area and poses no issue for accurate positioning of the etch. The plasma source should be suspended within the range of the stage, so we could position

the substrate under the source. We also should keep the same design (diameter of the source, distance between the electrodes and the orifice) of the prototype microplasma source as these were found to be successful. The orifice disc of the plasma source should be kept in the same plane as the end of the pole piece, so there is no chance of collision with the stage during stage movements. By first moving the stage below the plasma source, we could bring the stage up to a required distance from the plasma source. We have space available on the load lock side of the SEM chamber (right side of photograph shown in figure 5.12) and on the side opposite to the door (behind the pole piece shown in figure 5.12). If we utilise one of the available ports on the side opposite to the door behind the pole piece, we will have difficulty in making adjustments and connections as the pole piece blocks the view. Also it increases the chance of making physical contact with the pole piece leading to damage. This leads us to the port above the loadlock which currently houses the plasma cleaner, if we use this port it will be easier to mount the plasma source and make connections to it as it is easier to access it from the door. Figure 5.13 shows the loadlock side of the SEM chamber with the port of interest indicated by a red circle. We will use this port to suspend the plasma source inside the SEM chamber.

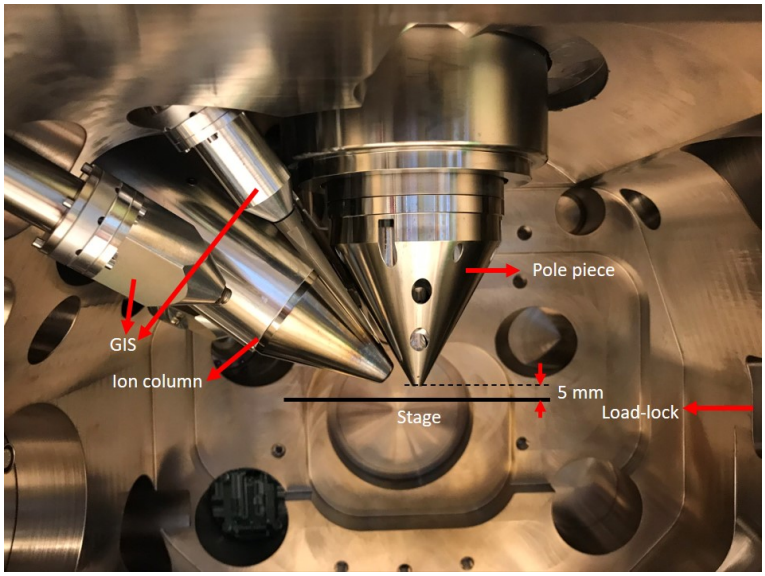

Figure 5.12: Photograph of the interior of the Nova nanoLab SEM from the point of view of the chamber door.

We decided to 3D print the anode connector (shown in figure 5.14) along with the gas feedthrough and the grid. Therefore eliminating the need of a sepa-

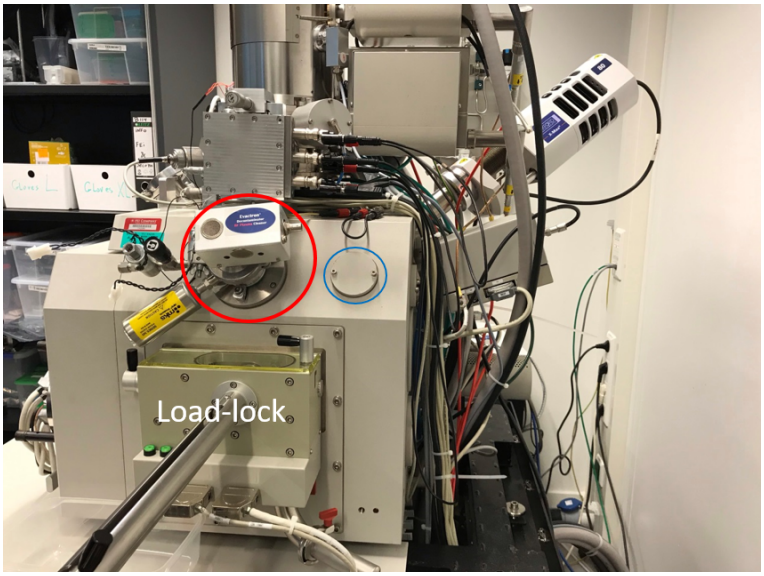

Figure 5.13: Photograph showing the load lock side of the Nova nanoLab SEM with port of interest (red circle, here containing the plasma cleaner) for suspending the microplasma source and the port of interest for the gas feedthrough (blue circle) for the delivery of Ar.

rate grid and the assembly required. The anode connector needs to be conductive to act as the anode, so it was made of 3D printed Aluminum. Figure 5.14 shows the CAD illustration of the anode connector. The outer diameter of the anode tube is 8 mm, while the inner diameter of the tube is 4.5 mm. The gas chamber is connected to a gas feedthrough which has an outer diameter of 2.8 mm. The anode connector needs to be biased, so to avoid soldering a screw hole was made for making the electrical connection to the anode connector. An orifice disc made out of Phosphor bronze was used as the cathode in the high vacuum setup. We used an orifice disc with an orifice diameter of 50 μm and a thickness of 100 μm.

To electrically isolate the anode connector from the orifice disc, we used a PEEK insulator. The PEEK insulator is designed as a push fit to the anode connector. The orifice disc is glued to the PEEK insulator by using a two component epoxy glue (Stycast 1266 [22][23]). The PEEK insulator is also glued to the anode connector using Stycast 1266 to prevent any leaks. The distance between the anode connector and the orifice disc cathode is kept at 0.5 mm. The anode connector with the PEEK insulator and orifice disc is shown in figure 5.15. The height of the anode connector is about 12.5 mm.

The plasma chamber lies between the grid in the anode connector and the orifice plate. A close-up of the plasma chamber is shown in figure 5.16. The

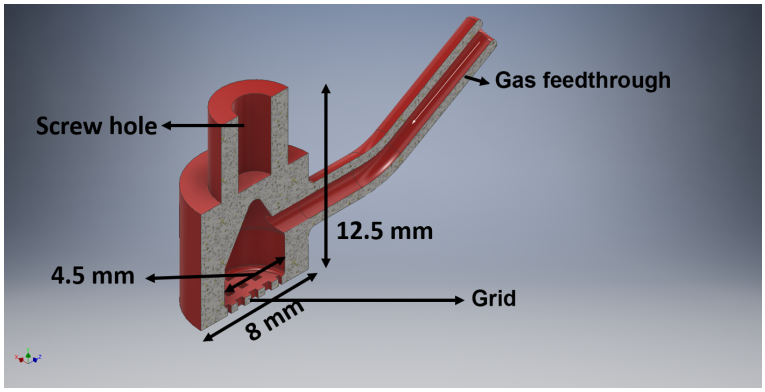

Figure 5.14: CAD illustration of the anode connector with a grid size of 0.5 mm x 0.5mm, the grid size is similar to the one used in the test setup.

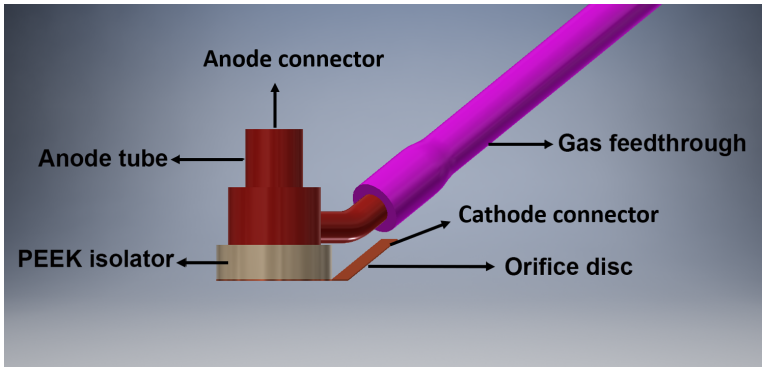

Figure 5.15: CAD illustration of the anode tube with the PEEK insulator and the orifice plate cathode.

height of the plasma chamber is 0.5 mm whereas the diameter of the chamber is 6 mm. The diameter of the plasma chamber is slightly larger than the value used in the high vacuum setup (diameter = 5.5 mm).

The different components of the adapter assembly used to suspend the microplasma source are shown in figure 5.17. The microplasma source is suspended from a device holder shown in 5.17a and it is made of aluminum. The device holder has space for holding two sources, so it could be used to suspend the evaporator (will be discussed in the next chapter) too. The bottom of the plasma source can be positioned by using the screws (shown in figure 5.17a) to lock the source in place. The device holder containing the microplasma source is connected to a fixture (shown in figure 5.17b) which is made of aluminum. The fixture containing the source is connected to the flange (shown in figure 5.17d) by

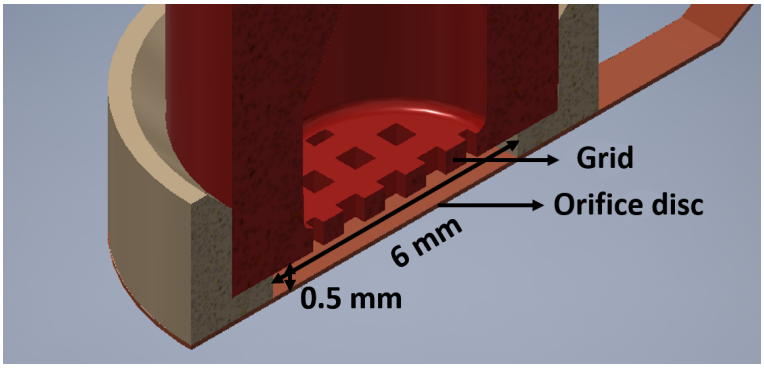

Figure 5.16: CAD illustration of the plasma chamber.

means of three support rods (shown in figure 5.17c). The support rods have a hole on the side to remove any trapped air. The length of the support rods is about 146 mm. This length is chosen such that the plasma source is at a distance of 40 mm from the axis of the pole piece. The support rods and the flange are made of non-magnetic stainless steel (RVS - 316). Also, we need two MHV electrical feedthroughs for the plasma source and a gas feedthrough for the delivery of gas, in our case Ar. The atmosphere end of the flange ends in a KF40 connection, which can be used to attach the required electrical feedthroughs for the source. For the delivery of Ar, we can use the port (blue circle) indicated in 5.13. Figure 5.18 shows the design of the gas feedthrough. On the atmospheric side we have a quarter inch stainless tube, which can be used with swagelok connectors. On the vacuum side, we have a stainless steel tube with a diameter of 2.8 mm. We used a viton tube with inner diameter of 2 mm to connect the anode connector to the gas feedthrough.

The plasma source needs to be suspended by the device holder which will also hold the evaporator. Since the adapter is made out of aluminum, the anode connector should be electrically isolated from the device holder. So, we used a PEEK cylinder which fits on top of the anode tube to make contact with the device holder. The CAD illustration of the complete plasma source is shown in figure 5.19. Figure 5.20 shows the photograph of the adapter along with the 3D printed anode tube.

All the components of the plasma source were thoroughly cleaned before placing them in an SEM. The metallic parts were first cleaned ultrasonically in a beaker containing acetone for 2 hours. Then, they were cleaned in a beaker containing ethanol for 2 hours followed by blow-drying the components with nitrogen. The non-metallic parts were cleaned in a beaker containing ethanol for 2 hours followed by blow-drying with nitrogen. The plasma source was assembled

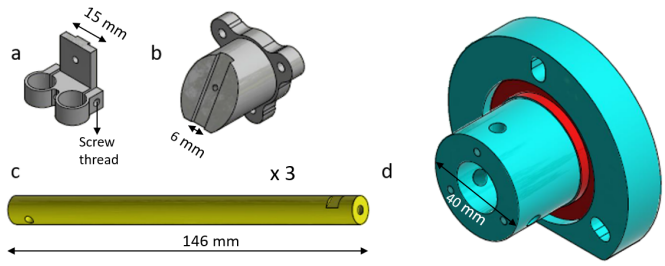

Figure 5.17: CAD illustrations of the different components of the adapter assembly. a) Device holder where the plasma source can be suspended. b) Fixture where the device support structure is attached. c) Support rods to which the fixture (b) is attached. d) the flange assembly in which three support rods are attached.

as shown in the CAD illustration shown in figure 5.19. The electrical connections were delivered by means of two electrical feedthroughs (MHV). The electrical connection to the anode was made by means of a screw and the electrical connection to the orifice plate was made by tin soldering a PEEK coated wire to the plate.

TEST OF THE PLASMA SOURCE

After assembling the miniature plasma source, we placed it in the desired port. The miniature plasma source in the SEM is shown in figure 5.21. Figure 5.22 shows the measured and the calculated chamber pressures as a function of the input Argon pressure. The effective pumping speed for the SEM is 70 l/s which is connected to a turbomolecular pump with a pumping speed of 250 /s [14]. When compared to figure 5.6 for the vacuum setup, we observe that the measured chamber pressure values in the SEM are much lower now. They are also lower than the calculated pressure, which might be due to the empirical equation used to calculate the pressure. In the high vacuum setup we used a double sided Kapton tape to seal the orifice plate, which was leaky and led to pressure values much larger than the calculated pressure. The initial test was to determine whether we were able to obtain a plasma. After reaching a base pressure of $3 * 10^{-6}$ mbar, we let in Ar gas with a line pressure (P_{Ar}) of 12 mbar. This resulted in a chamber pressure of $1.45 * 10^{-5}$ mbar. We gradually increased the supply voltage to the plasma source until we observed an argon current, I_{Ar} of

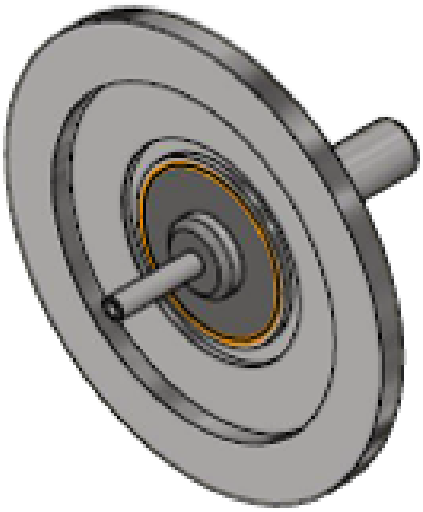

Figure 5.18: CAD illustration of the modified KF40 gas feedthrough to deliver Ar made of RVS 316 stainless steel.

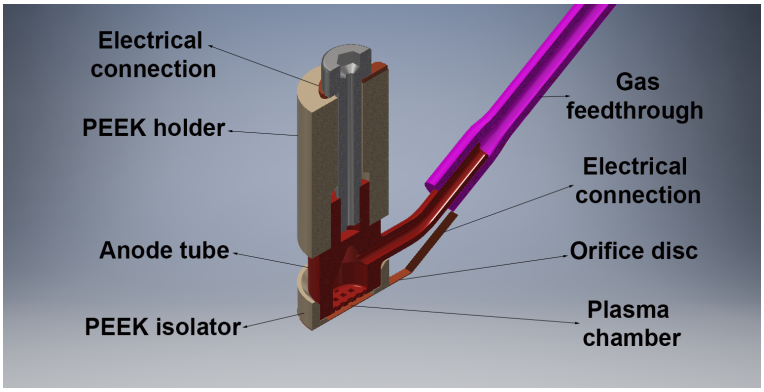

Figure 5.19: CAD drawing of the miniature plasma source for implementation in SEM showing the different components.

5 μA. Figure 5.23a shows the photograph of the plasma source inside the SEM.

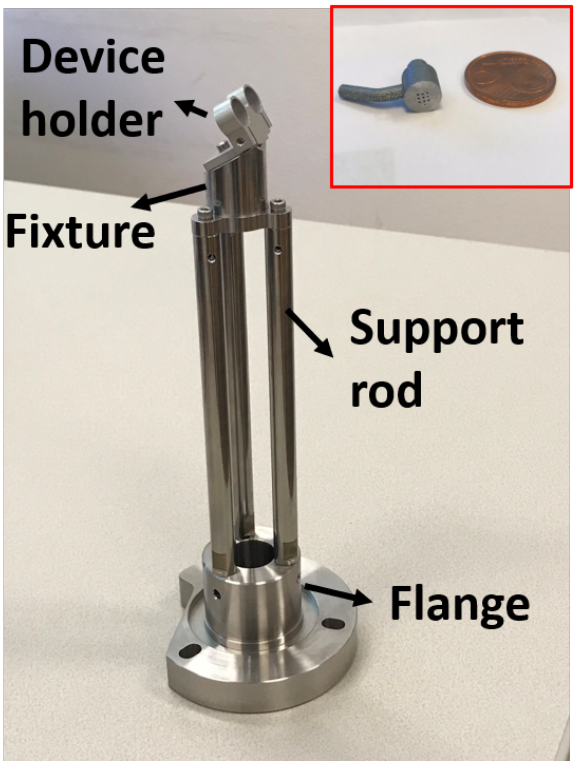

Figure 5.20: Photograph of the adapter. Inset picture showing the 3D printed anode tube as compared to a 5 eurocent coin.

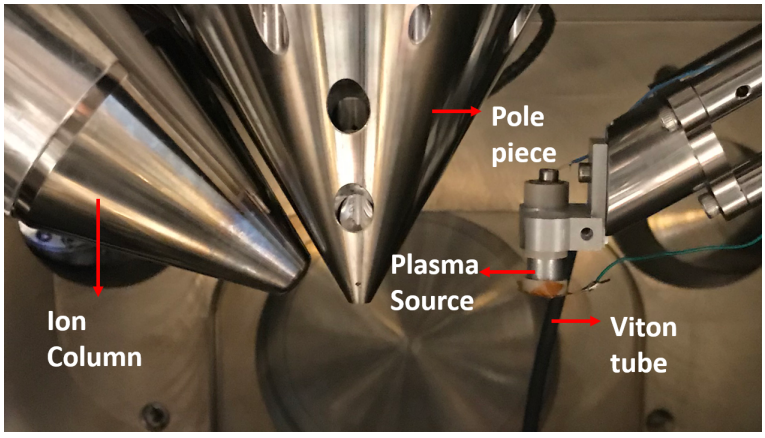

Figure 5.21: Photograph of the miniature plasma source inside the SEM.

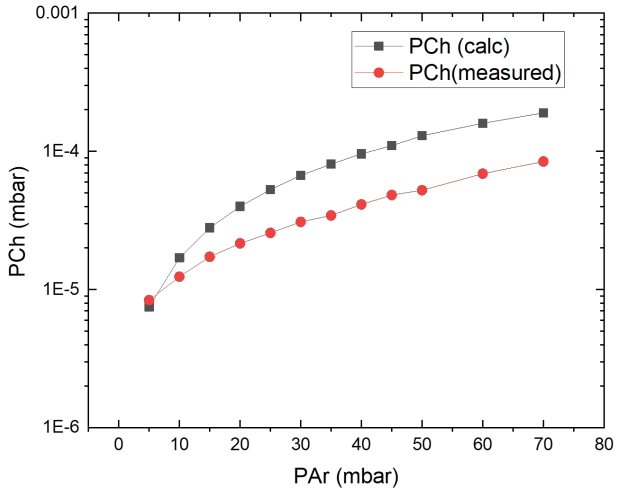

Figure 5.22: Graph showing the measured chamber pressure (PCh(measured)along with the calculated chamber pressure (PCh(calc)) using equation 5.3 for different input Argon pressures (PAr).

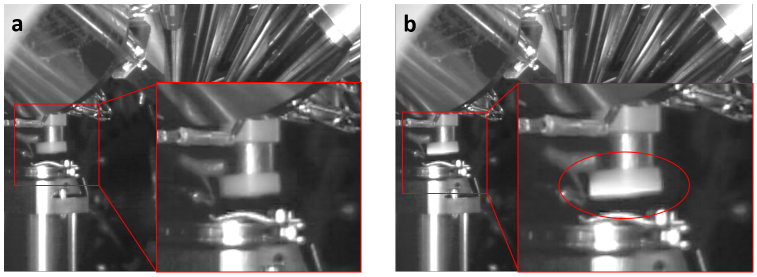

Figure 5.23: a)Photograph of the plasma source from the SEM camera. b) Photograph of the plasma source under operation with an observable glow of the plasma.

Figure 5.23b shows the photograph of the plasma source under operation, where we observe a glow indicating the successful ignition of plasma inside the SEM .

Subsequently, we carried out the test of utilising the plasma source as a sputter etching tool. The substrate was a 20 nm thick Au film on a Si wafer and placed at a distance of 0.5 mm from the plasma source. This was achieved by first moving the stage below the plasma source and then gradually moving the stage up until we reach the required distance. The gas line of the plasma source was flushed 6 times with Ar to remove residual gas in the line. The substrate was

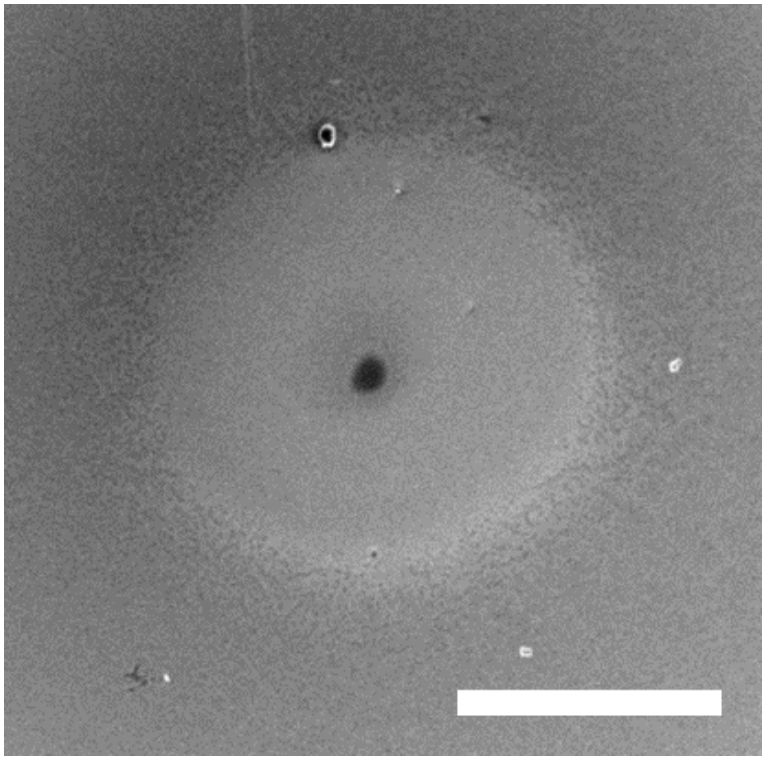

Figure 5.24: SE image of the etch spot on a 20 nm Au film on Si. The scale bar is 200 μm.

exposed to the plasma for 90 minutes, while keeping the orifice plate at a positive potential of 205 V and the applied argon pressure (P_{Ar}) at 12 mbar. The long duration of exposure was to make sure that the Au layer was completely etched. We measured an I_{Ar} of 500 μA at a voltage of 406 V and a substrate current, I_{etch} of 3 nA with a P_{Ch} of $1.32 * 10^{-5}$ mbar. When we observed the exposed area in an SEM, we observed an etch spot with a diameter of 35 μm, as shown in figure 5.24. In the high vacuum setup, we observed an etch spot of 200 μm with an orifice diameter of 75 μm and the substrate placed at a distance of 1 mm. The EOD simulation for the geometry of the setup in the SEM is shown in figure 5.25. The parameters for the ray-tracing simulation were similar to the previous case of the high vacuum setup. Here also we observe bending of the Ar ion trajectories closer to the orifice wall, due to the electrostatic field. Assuming similar conditions as in the high vacuum setup, a crude estimate of the beam diameter can be obtained by taking the full width of the ions arriving at the sample. This results in a diameter of 140 μm for Ar ions starting with an energy of 25 meV.

From equation 5.14, with an I_b of 2.7 nA we obtain a sputter rate of 3 nm/min.

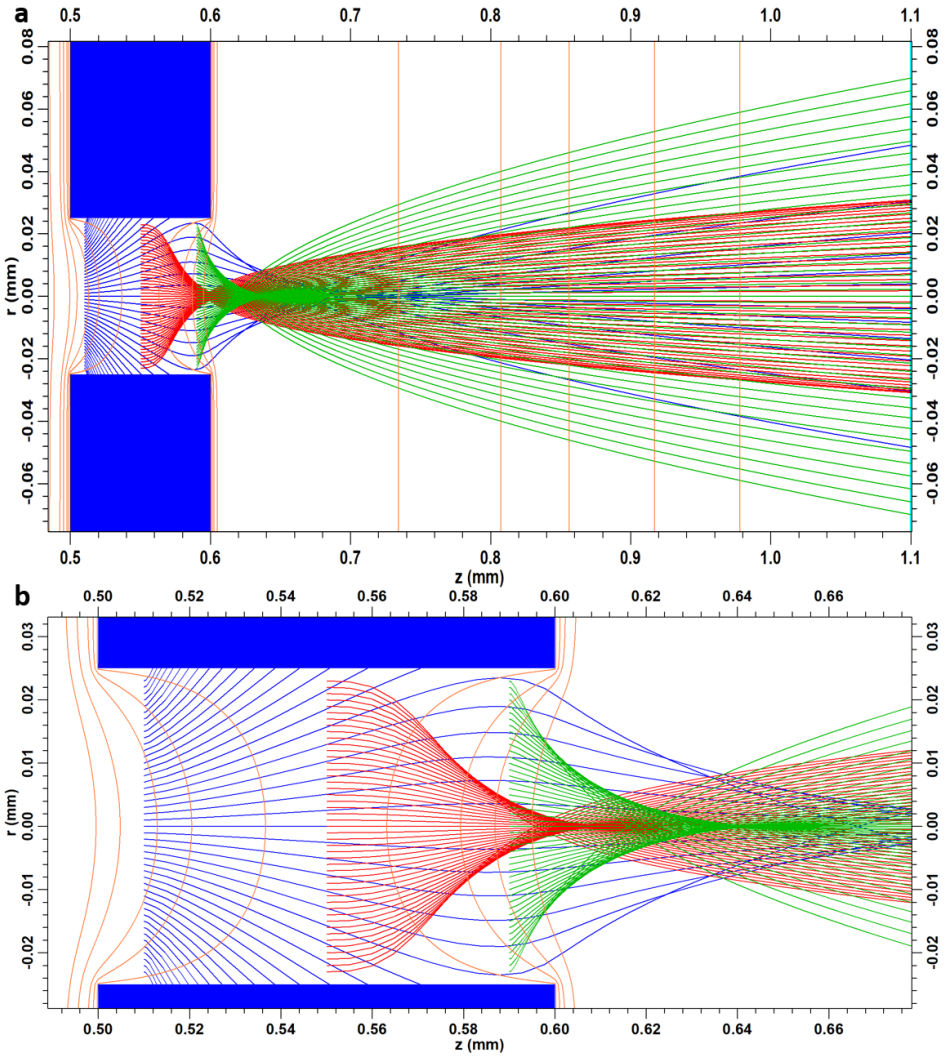

Figure 5.25: a) Ar ion trajectories (blue, red and green) for the SEM setup with an orifice diameter of 50 μm and with an initial energy of 25 meV at three different locations: 10 μm from the start of the orifice (0.51 mm, shown in blue colour), at center (0.55 mm, shown in red colour) and at 10 μm from the end of the orifice (0.59 mm, shown in green colour). Ar ions starting closer to the orifice are focussed. b) A close-up image of the Ar ion trajectories in the orifice.

So, we would completely etch a 20 nm film of Au in 7 minutes. The 90 minutes of etching time was more than enough to remove the Au film. Also, surrounding the etch spot in figure 5.24, we observe a halo with a diameter of 350 μm. This halo might be caused either by re-deposition of Au or due to direct sputtering of the

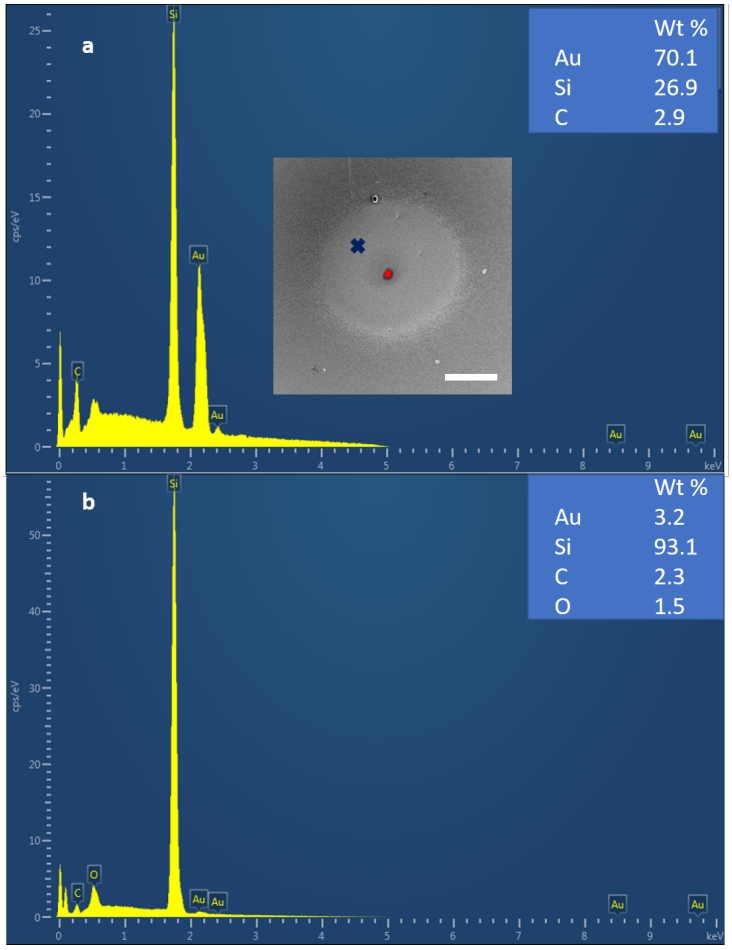

Figure 5.26: a)EDX spectrum of a spot (blue cross in inset image) outside the etch spot and the atomic percentages of the detected elements. Inset image : SE image of the etch spot showing the location of the EDX spectrum. The scale bar is 200 μm. b) EDX spectrum of the etch spot (red spot in inset image) and the atomic percentages of the detected elements.

Au film. With an I_{Ar} of 500 μA, we would expect a substrate current I_{etch} of 23.1 nA based on equations 5.11, 5.12 and 5.13, deviating from the observed value.

We carried out an EDX analysis on the etch spot to determine whether there was any Au present in the etched spot. The result of the EDX analysis is shown in figure 5.26. It can be observed from figure 5.26 that the presence of Au atoms in the etch spot area is extremely low, whereas we find a clear presence of Au outside the etch spot (a strong Au peak). This confirms that we have completely etched through the Au film. We also carried out a profilometer measurement to

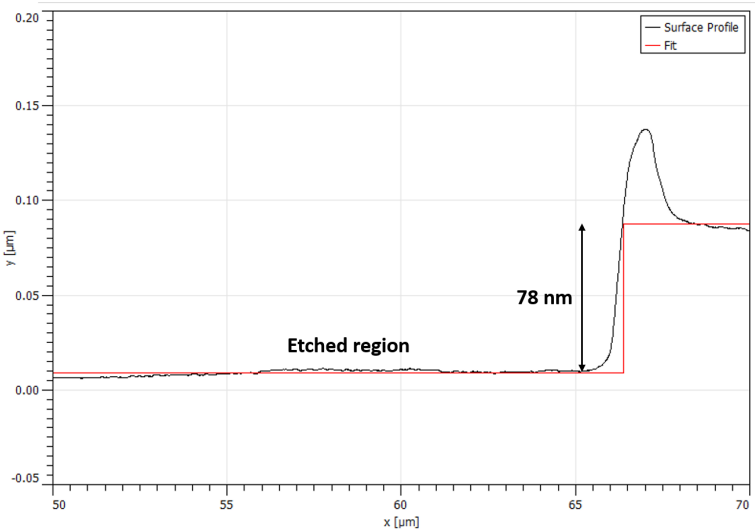

Figure 5.27: Graph showing the surface profile of the etch spot as measured by a profilometer. The fit gives an etched height of 78 nm.

measure the etch depth. The result of the profilometer measurement is shown in figure 5.27. An etch depth is observed of 78 nm, completely etching through the Au film into the Si substrate. The 90 minute etching time has removed 58 nm of Si from the substrate, so for Si we have an etch rate of 0.7 nm/min. Etch rates of 25 – 80 nm/min for Au are obtainable in an argon ion mill tool (eg., SCIA MILL 150) [24]. In an Argon ion mill tool found in a cleanroom, typically the energy and the current density of Ar ions are tunable over a wide range, hence the etch rates in a cleanroom tool are high compared to our miniature tool. The etched region shows a height variation of 5 nm, so the etching is quite uniform. We also observe re-deposition, shown in figure 5.27. From figure 5.24, we observe a wide area with a brighter contrast. This could be due to re-deposition of Si on top of the Au leading to a brighter contrast.

5.8. CONCLUSION

To summarize, in this chapter we listed the various requirements for implementing a miniature plasma source in an SEM. We designed and built a prototype miniature plasma source, and we were able to obtain a plasma at SEM operating pressures and keeping the potential applied between the electrodes below 500 volts. We measured the Paschen curve and the IV curve for the plasma source in a high vacuum test setup. We observed an etch diameter of 200 μm, in the high vacuum setup with a voltage of 390 V and measured I_{Ar} of 399.4 μA and ion cur-

rent I_b of 5.26 nA. The observed ion current deviates from the calculated values, which could be due to the approximate nature of the calculations resulting in an estimate for the ion current. The substrate is kept at a distance of 1 mm from the orifice disc. To implement the miniature plasma source in an SEM, a new version was designed and fabricated. This miniature plasma source was tested in an SEM, using Ar gas and igniting the plasma. Utilizing this Ar plasma, we were able to etch a 20 nm thick layer of Au on Si with an etch diameter of 35 μm at an etch rate of 3 nm/min. The substrate is kept at a distance of 0.5 mm with a voltage of 406 V, an I_{Ar} of 500 μA and ion current I_b of 2.7 nA . The total height of the plasma source (between the PEEK holder and the orifice disc) is 25 mm, even though the actual plasma chamber has a diameter of 6 mm with electrode separation of 500 μm. One important factor which is required for utilizing the plasma source as a sputter tool, is to keep the gas line clean by flushing the line several times before starting experiments to remove residual air, residual water vapor present and other contaminants trapped in the viton tube and the external gas connections to the Ar cylinder. For future experiments it is advised to attach a heater to the gas delivery line outside the SEM to remove contaminants (residual water vapour, etc.) in the gas line. By replacing the gas by dry air, we can utilize an oxygen plasma to clean substrates and to improve the quality of FEBID deposits.

REFERENCES

[1] K. Matra, Y. Mizobuchi, H. Furuta, and A. Hatta, *Local sputter etching by micro plasma jet in sem,* Vacuum **87**, 132 (2013).

[2] F. Iza, G. J. Kim, S. M. Lee, J. K. Lee, J. L. Walsh, Y. T. Zhang, and M. G. Kong, *Microplasmas: Sources, particle kinetics, and biomedical applications,* Plasma Processes and Polymers **5**, 322 (2008).

[3] K. Matra, H. Furuta, and A. Hatta, *Current-voltage characteristics of DC discharge in micro gas jet injected into vacuum environment,* Journal of Physics: Conference Series **441**, 012021 (2013).

[4] H. Miyazoe, I. Utke, H. Kikuchi, S. Kiriu, V. Friedli, J. Michler, and K. Terashima, *Improving the metallic content of focused electron beam-induced deposits by a scanning electron microscope integrated hydrogen-argon microplasma generator,* Journal of Vacuum Science & Technology B **28**, 744 (2010).

[5] H. Miyazoe, M. Sai, S. Stauss, and K. Terashima, *Ultrahigh-frequency*

microplasma jet as a low-power, high-density, and localized ions/radicals source, Journal of Vacuum Science & Technology A **27**, 9 (2009).

[6] J. Mulders and P. Trompenaars, *An in-situ low energy argon ion source for local surface modification,* in *European Microscopy Congress 2016: Proceedings* (2016) pp. 453–454.

[7] G. D. Prima, R. Sachser, P. Trompenaars, H. Mulders, and M. Huth, *Direct-write single electron transistors by focused electron beam induced deposition,* Nano Futures **3**, 025001 (2019).

[8] M. Perez-Roldan, J. Mulders, and P. Trompenaars, *C-FEBID etching mask and C-FEBID in-situ removal; enabling a new micro- and nano fabrication route,* Microelectronic Engineering **201**, 22 (2018).

[9] A. Prokhodtseva, J. Mulders, and T. Vystavel, *Applications of an in-situ low energy argon ion source for improvement of tem and sem sample quality,* Applications of an in-situ Low Energy Argon Ion Source for Improvement of TEM and SEM Sample Quality **23**, 298–299 (2017).

[10] M. Dutka, R. Isaacs, A. Prokhodtseva, and T. Vystavěl, *In-situ low energy argon ion source for artifact free high resolution stem imaging,* Microscopy and Microanalysis **25**, 548–549 (2019).

[11] J. O'Hanlon, *A User's Guide to Vacuum Technology* (John Wiley and Sons, Ltd, New York, N.Y. 10158-0012, 1989).

[12] T. Fujimoto and M. Usami, *Rarefied gas flow through a circular orifice and short tubes,* Journal of Fluids Engineering **106**, 367 (1984).

[13] L. van Kouwen, *The Nano-aperture Ion Source,* Ph.D. thesis, Delft University of Technology (2017).

[14] S. Hari, *High resolution resist-free lithography in the SEM,* Ph.D. thesis, Delft University of Technology (2017).

[15] I. Figueiredo, N. Bundaleski, O. Teodoro, K. Jousten, and C. Illgen, *Influence of ion induced secondary electron emission on the stability of ionisation vacuum gauges,* Vacuum , 109907 (2020).

[16] *https://omnexus.specialchem.com/selection-guide/polyetheretherketone-peek-thermoplastic,* (Accessed on 14-03-2021).

[17] *https://www.accuglassproducts.com/double-sided-kapton-tape-silicone-14,* (Accessed on 14-03-2021).

[18] *https://www.bronkhorst.com/int/products/pressure/el-press/p-502c/,* (Accessed on 14-03-2021).

[19] B. Lencova and J. Zlamal, *Electron Optical Design program package (EOD),* (E5.004).

[20] R. Rejoub, B. G. Lindsay, and R. F. Stebbings, *Determination of the absolute partial and total cross sections for electron-impact ionization of the rare gases,* Phys. Rev. A **65**, 042713 (2002).

[21] A. Bogaerts and R. Gijbels, *Role of Ar2+ and Ar2+ ions in a direct current argon glow discharge: A numerical description,* Journal of Applied Physics **86**, 4124 (1999).

[22] *"Henkel Loctite Stycast 1266 Epoxy Part A clear 1 LB 9 oz can, https://www.ellsworth.com/products/by-manufacturer/henkel-loctite/encapsulants/epoxy/henkel-loctite-stycast-1266-epoxy-part-a-clear-1-lb-9-oz-can/ ",* (Accessed on 10-01-2022).

[23] *"Henkel Loctite Stycast 1266 Epoxy Part B clear 7 9 oz bottle, https://www.ellsworth.com/products/by-manufacturer/henkel-loctite/encapsulants/epoxy/henkel-loctite-stycast-1266-epoxy-part-b-yellow-7-oz-bottle/ ",* (Accessed on 10-01-2022).

[24] *http://pta-grenoble.com/fr/facilities/ibe-etcher-mil150-from-scia,* (Accessed on on 14-03-2021).

6

IN-SITU THERMAL EVAPORATOR

6.1. INTRODUCTION

In the previous chapters, we have demonstrated an in-situ substrate heater, in-situ area selective ALD and an in-situ sputter etch tool in SEM for *Cleanroom in an SEM*. The next step is to implement a miniature evaporation source inside the SEM to be able to deposit material to complement the already existing techniques in the SEM. An e-beam evaporator in an SEM was demonstrated by Titze based on a commercially available e-beam evaporator [1][2]. The disadvantage of the evaporator of Titze is that it is a bulky source which is mounted at an angle and is mainly used for coating applications over a large area. In our application, we require an evaporator that is small and has a smaller deposition area. As discussed in chapter 1, thermal evaporation operates at pressures of 10^{-6} to 10^{-8} mbar. An SEM operates between 10^{-6} and 10^{-5} mbar, we have an overlap in the pressure region 10^{-6} mbar.

6.2. REQUIREMENTS FOR THE THERMAL EVAPORATOR

When we add the in-situ thermal evaporator to the SEM, it shouldn't affect the operation of the SEM. We should be able to use the SEM for imaging the substrate. This leads to several requirements for the design of the thermal evaporator. The requirements are:

1 The deposition angle of incidence is normal to the substrate, to obtain a uniform thickness of the deposit in a local area (around 100 μm).

2 The evaporator shouldn't disturb the electron beam nor should it heat the surroundings.

3 The chamber should be kept at high vacuum condition ($< 10^{-5}$ mbar) during the operation of the evaporator.

4 The evaporator should occupy a minimum floor space in the SEM, as there is little space available in the SEM.

5 All materials used should be non-magnetic.

6 All materials used should be vacuum compatible and have a low outgassing rate.

7 No additional pump should be needed.

8 The deposit material should be easy to replace.

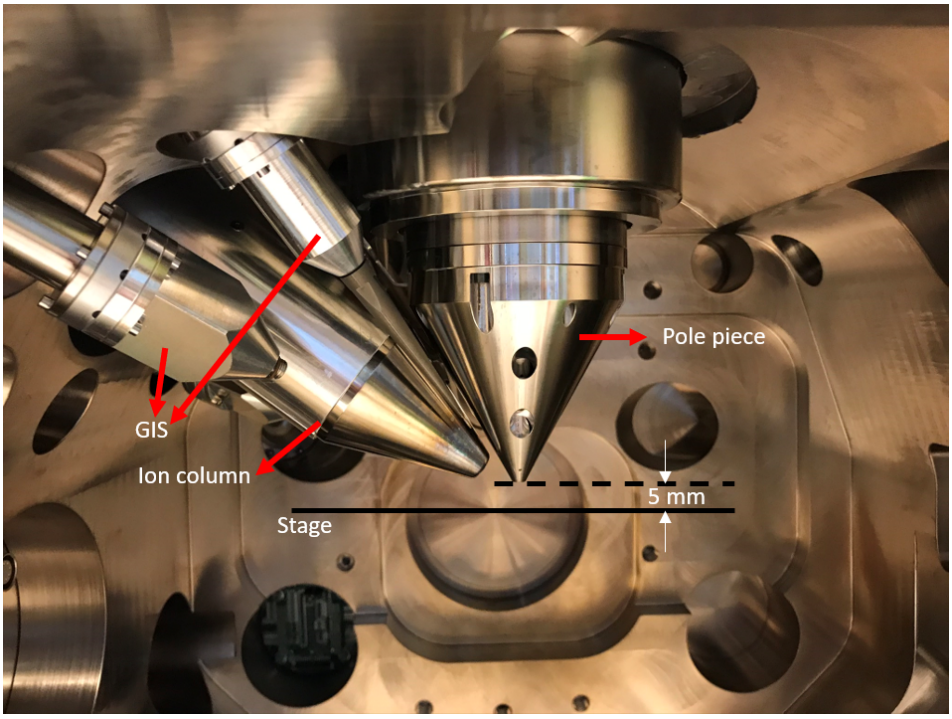

Figure 6.1: Photograph of the interior of the Nova nano SEM from the point of view of the chamber door.

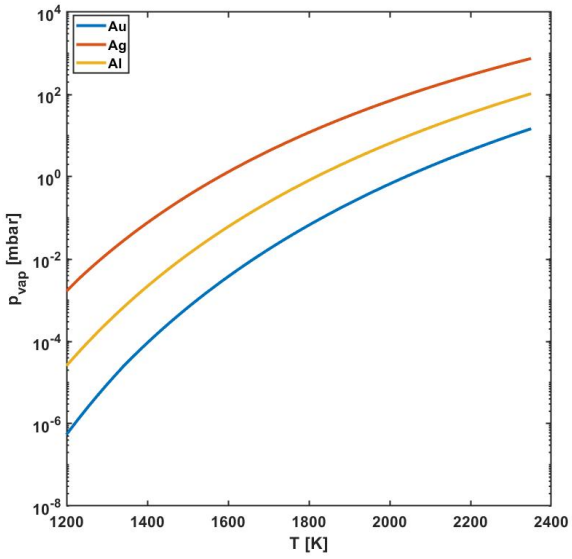

Figure 6.2: Plot of the vapor pressure for Au, Al and Ag [3].

6.3. DESIGN OF THERMAL EVAPORATOR IN VACUUM SETUP

The evaporant (material to be deposited) material needs to have a high vapor pressure at low temperatures while the material of the evaporator (which contains the evaporant) must have a low vapor pressure at high temperatures. So that only the evaporant is deposited on the substrate. Since, we will be heating the evaporator to a high temperature we need to make sure not to heat the surrounding materials. The interior of the SEM is shown in figure 6.1. We need to choose an evaporator that can heat up the evaporant to a high temperature. The temperature depends on the material and the vapor pressure of the evaporant. The vapor pressure of Au, Al and Ag as a function of temperature is shown in figure 6.2. So, for Au evaporation we need to heat the evaporator to about 1700 K, to have a vapor pressure of 10^{-2} mbar [4]. At this vapor pressure 10^{-2} mbar, it is possible to deposit material at a usable rate [4]. We decided to use a Philips I-cathode source (used in cathode ray tubes) as the evaporator. The cathode source is designed to operate at around 1000 - 1500 K [5]. The Philips I-cathode can be used upto 1800 K, but it reduces the lifetime of the source [6][7]. The cathode source consists of a tungsten pill box in a molybdenum tray which is placed over a molybdenum cylinder. The heating element consists of a tungsten

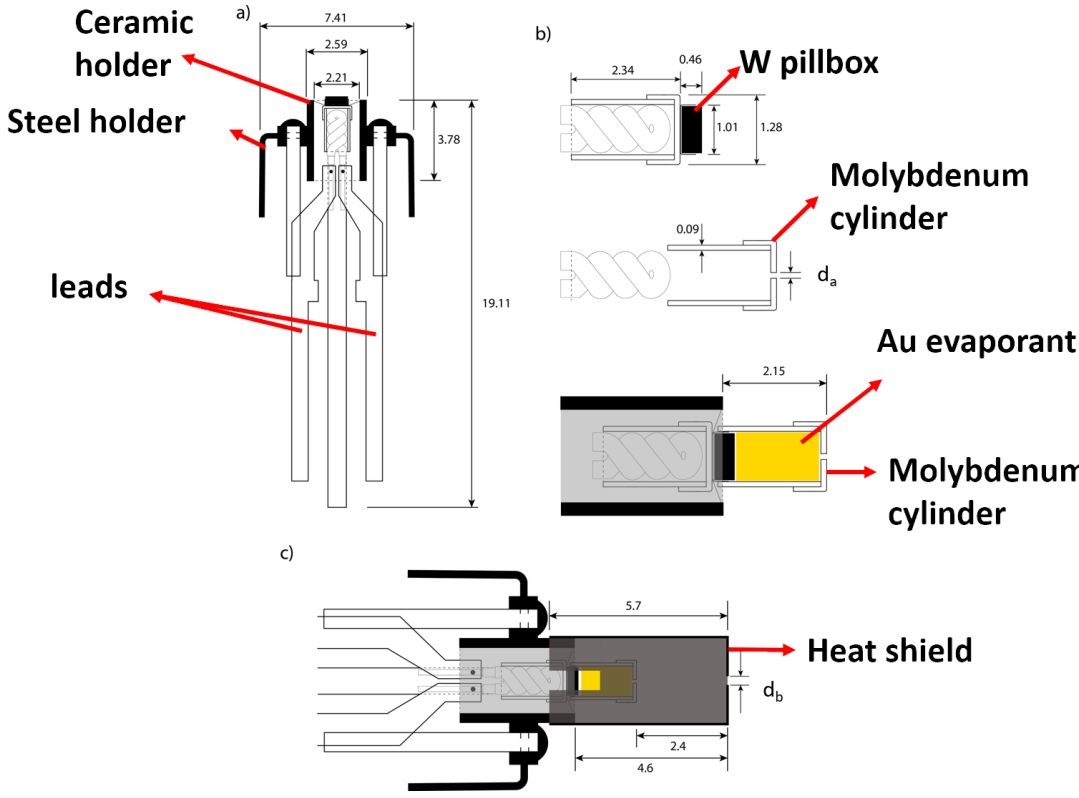

Figure 6.3: a) Sketch of the Philips I-cathode source with various dimensions in mm. b) Close up of the W pillbox, the molybdenum cylinder with a hole d_a with a diameter of 0.2mm and the molybdenum cap placed over another W pillbox with dimensions in mm. c) Sketch of the evaporator assembly with a stainless steel heat shield with a hole d_b with a diameter of 0.4 mm

wire coated with an isolating ceramic in a spiral configuration and is placed inside the molybdenum cylinder. The molybdenum cylinder with the W pillbox is held in place by three wires (made of tungsten-rhenium) attached to the ceramic holder. The sketch of the Philips I-cathode source is shown in figure 6.3a, along with it's dimensions in mm. The evaporant now needs to be mounted on top of the W pillbox, so the W pillbox heats up the evaporant. W has a vapor pressure of 10^{-11} mbar at 2073 K, and doesn't impact the evaporant material [4]. Also, the Philips I-cathode source should be mounted such that the W pillbox containing the evaporant faces the substrate. The source is now placed face down to the substrate. Hence, we need a cap which can be placed over the W pillbox and can hold the evaporant in place. The cap when placed over the W pillbox will be at a high temperature of 1700 K, hence the material of the cap should withstand the

high temperature. So, we decided to take a spare Philips I-cathode and removed the W pillbox and the molybdenum cylinder. In the molybdenum cylinder we drilled a hole d_a with a diameter of 0.2 mm. The molybdenum cylinder acts as the cap and can withstand the high temperature. The hole is required to have the evaporant escape from the cap to the substrate. The molybdenum cylinder with its dimensions is shown in figure 6.3b. The size of the hole was based on the evaporant flux on the substrate and described elsewhere [5]. We can determine the area of uniform coating by using the cosine law of emission [8] using the hole (d_a) in the molybdenum cap as the source.

In addition, we decided to add a stainless steel (non-magnetic, RVS316L) cap over the evaporator, which acts as a heat shield. Since the molybdenum cap is also at high temperature, we have a big surface area (11.95 mm) which is at 1700 K and radiates heat. We can estimate the radiated power by using equation [link to eqn from heater chap] from chapter 2, resulting in 0.96 W of power radiated. Based on the heat shield ANSYS simulation in chapter 2, each heat shield reduces the temperature by 1/3. So, the heat shield should be at approximately 860 ^{o}C. Also, the stainless steel cap needs to have a hole d_b (0.4 mm)to direct the deposition spot onto the substrate and cut off the cosine distribution. The stainless steel heat shield is mounted by a push fit on to the steel holder as shown in figure 6.3c. A Teflon adapter with electrical pins was used to connect the I-cathode to the power supply.

6.4. FABRICATION AND ASSEMBLY

For the evaporator assembly we need to fabricate the heat shield made of stainless steel whereas the rest of the components are taken from the Philips I-cathode sources. We took two Philips I-cathode sources, and from one of them we carefully removed the W pillbox by means of a tweezer. The molybdenum cylinder is gently removed from the heating element using a tweezer. A hole with diameter d_a of 0.2 mm was drilled onto the molybdenum cap. Similarly a hole was drilled into the stainless steel heat shield with a diameter d_b of 0.4 mm.

The metallic components (connecting leads, heat shield, molybdenum cap and heat shield) were placed in a beaker containing acetone and kept in an ultrasonicator for 2 hours followed by cleaning them in a beaker containing ethanol for 2 hours. Finally the components were blown dry with Nitrogen gas. The non-metallic components (connecting wires, the Philips I-cathode and Teflon adapter) were placed in a beaker containing ethanol and kept in an ultrasonicator for 2 hours and the components were blown dry with Nitrogen gas. For the evaporant, we chose Au as the deposit material, as it has a sufficiently high vapor pressure at the operating temperature of the I-cathode. The evaporator was

assembled and mounted in the vacuum setup described in chapter 4. Two electrical feedthrough's were used to supply the current to the evaporator. A Delta Elektronika ES030 – 5 power supply was used to supply the power to the evaporator [9]. The supply leads of the I-cathode with the heat shield is connected to two electrodes made of copper. The copper electrodes are attached to a Teflon adapter which is connected to the 3 DOF (degrees of freedom) manipulator in the high vacuum setup. The Teflon adapter is used to thermally isolate the copper electrodes from the manipulator.

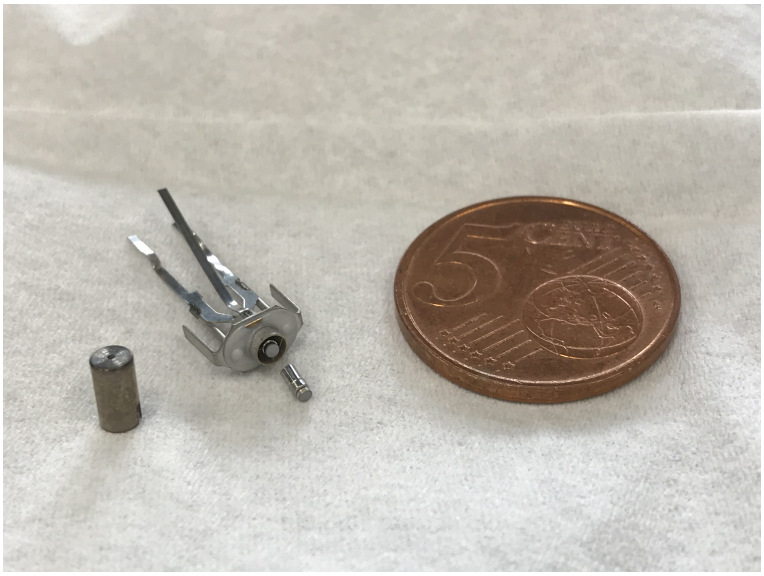

Figure 6.4: Photograph of the evaporator assembly consisting of Philips I-cathode, molybdenum cap and the heat shield with a 5 euro cent coin as a reference.

6.5. PERFORMANCE TESTS IN A VACUUM SETUP

The initial test was to heat up the evaporator. The evaporator was first heated by applying a voltage of 10 V for 60 seconds, to remove any contaminant left over from the evaporator. After that, the potential was increased to 14 V resulting in a current of 0.16 A and a power of 2.24 W. Figure 6.5 shows the evaporator in operation in the high vacuum setup. A glow can be observed on the evaporator, due to the high temperature (approx. 1700 K).

Now that we can successfully heat up the evaporator to a high temperature, we need to demonstrate its evaporation capabilities. We used a Si substrate and placed it at a distance of 1 mm from the evaporator. As before, we applied a voltage of 10 V to the evaporator for 60 s and then increased the voltage to 14 V. The

evaporator was kept on for about 300 seconds. The voltage was then gradually reduced to zero. During the operation of the evaporator, the chamber pressure was $1.3.10^{-6}$ mbar, satisfying the pressure requirement. After the evaporation, we took out the sample and inspected it under the SEM, shown in figure 6.6. We observe a hazy profile on the edge of the deposition, which could be due to vibration of the evaporator assembly as it is suspended. Next, to measure the deposition rate and the deposited thickness we used a tweezer to scratch the deposited spot. The measured height of the deposition spot is determined with a Dektak profilometer to be about 87 nm as shown in figure 6.7. This results in an evaporation rate of 0.29 nm/s. The size of the deposit is approximately 1 mm. The roughness of the deposit is 10 nm (ignoring the scratch) between 100 to 400 μm over the scanned area shown in 6.7.

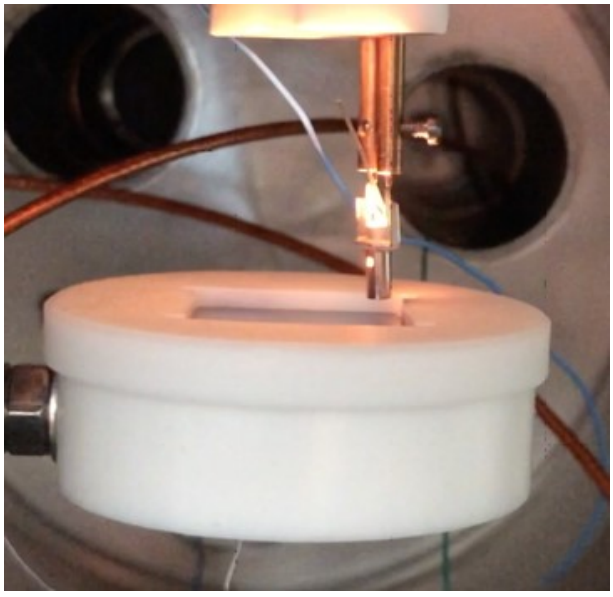

Figure 6.5: Photograph of the thermal evaporator in operation in the vacuum setup. The glow observed is due to the high temperature(1700 K) of the Philips I cathode.

We also carried out a test to check the increase of temperature of a metal (sheet metal), when the sheet metal is kept at a distance of 4 mm next to the evaporator. The sheet metal is a replacement for the SEM pole piece. We observed an increase of temperature upto 34.3 ^{o}C.

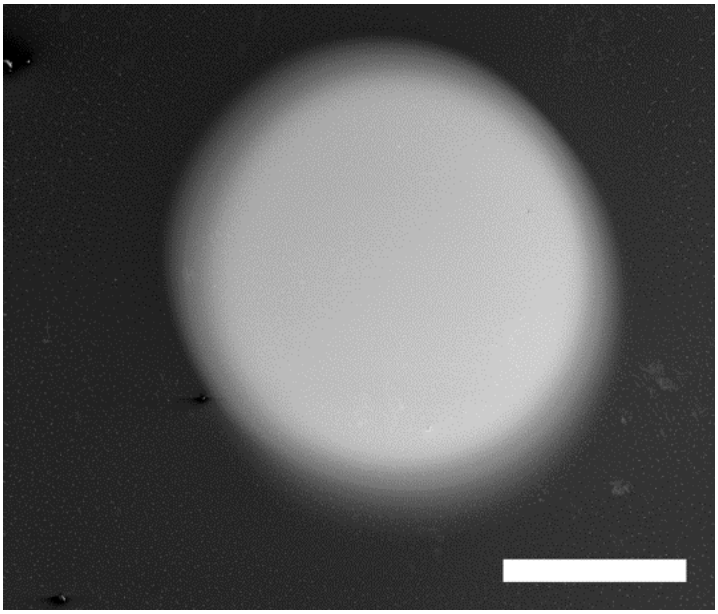

Figure 6.6: Secondary electron image of the deposited spot. Scale bar is 0.5 mm

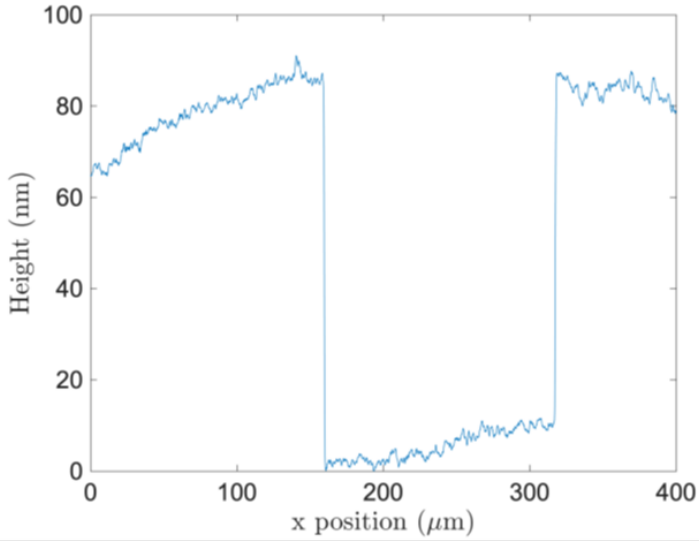

Figure 6.7: Measured height of the Au deposit using a profilometer. We used a tweezer to gently scratch the center of the deposited spot to accurately measure the height.

6.6. DESIGN OF THE THERMAL EVAPORATOR IN SEM

The prototype thermal evaporator cannot be directly placed into the SEM. We will use the adapter which was used previously for the plasma source to mount our evaporator. By using the adapter we will place the evaporator at a distance of 40 mm from the optical axis of the SEM column. The details of the adapter have been discussed in section 4.7 of chapter 4. The CAD illustration of the Philips I-cathode with its heat shield is shown in Figure 6.8. To electrically connect the supply leads of the Philips I cathode, we laser welded two stainless steel (RVS 316L) leads with a rod diameter of 1.5 mm. Two insulator tubes are then push fitted over the supply leads as shown in figure 6.9, the insulator tubes are made of aluminum oxide. The supply leads are connected to an external power supply through an electrical feedthrough. Since the Philips I cathode is heated to a high temperature of 1700 K, we can't directly mount the evaporator assembly to the device holder of the adapter. The support leads are laser welded to a thermal bridge 1. The thermal bridge 1 has a length of 20.15 mm and it has a staggered design (shown in the inset picture of figure 6.10) to reduce the heat transfer due to conduction.

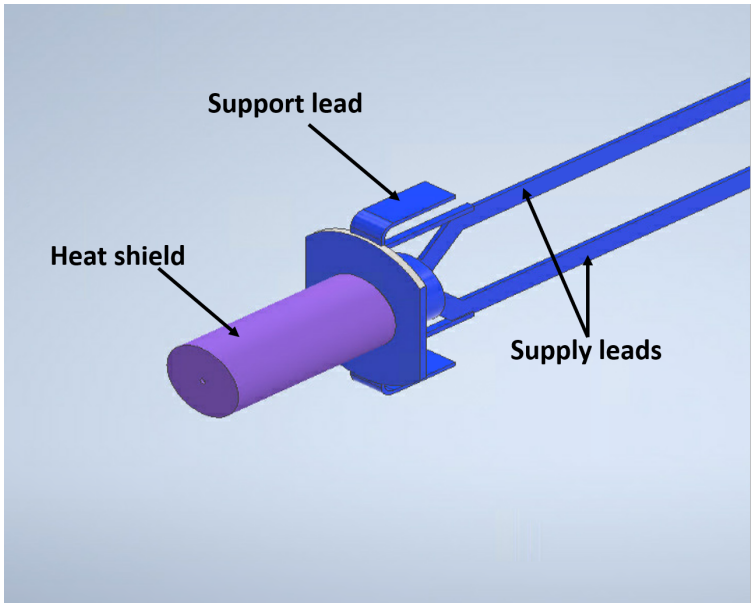

Figure 6.8: CAD illustration of the Philips I cathode with its heat shield.

A second thermal bridge 2 is 13 mm in length and has a similar staggered design to reduce the heat transfer further. Figure 6.11 shows the thermal bridge 2. And the connection between the thermal bridge 1 and 2 is shown in figure

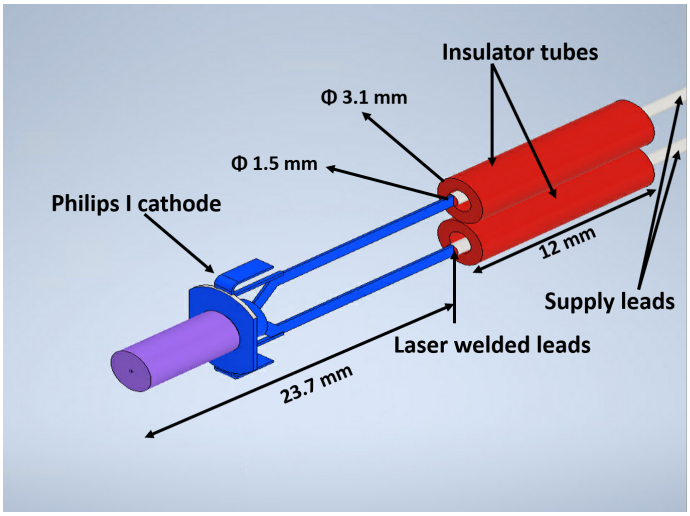

Figure 6.9: CAD illustration of evaporator connected to the supply leads through insulator tubes.

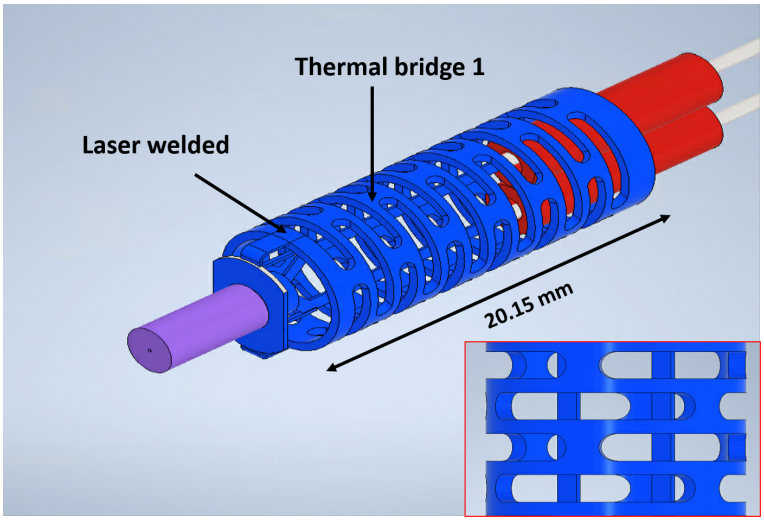

Figure 6.10: CAD illustration of the thermal bridge 1. Inset picture showing a close-up of the thermal bridge.

6.12. The thermal bridges 1 and 2 are connected (push fit) by a thermal cap which is used to fix the insulator tubes of the Philips I cathode. The insulator tubes are used to provide electrical isolation between the supply leads and the device holder which is grounded. The evaporator assembly with the two thermal bridges is shown in figure 6.13.

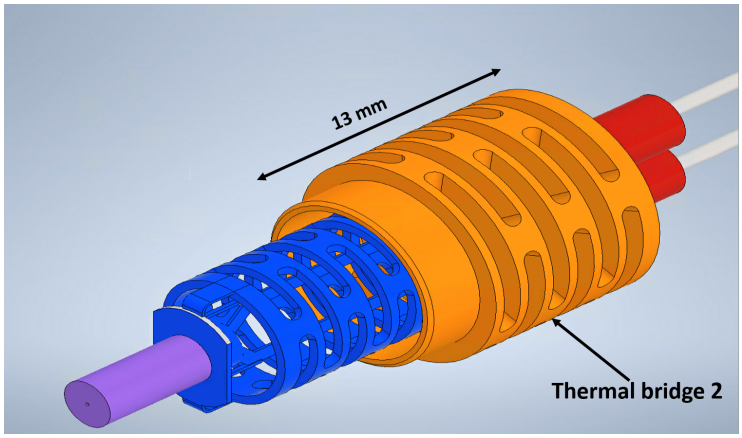

Figure 6.11: CAD illustration of the thermal bridge 2.

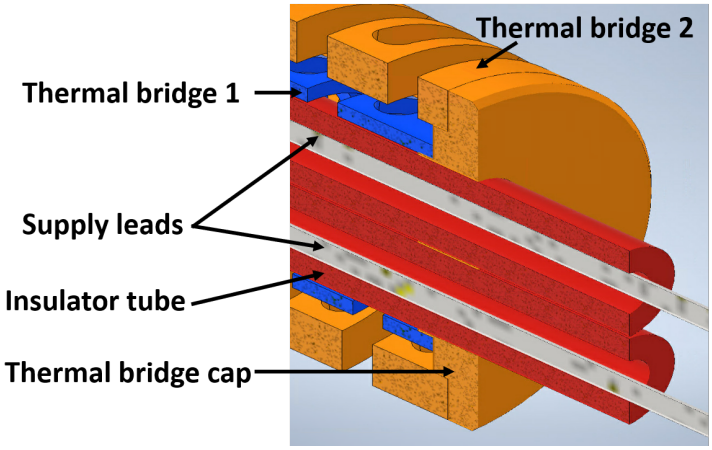

Figure 6.12: CAD illustration of the thermal bridge 2.

Since the heat shield of the evaporator is estimated to be at around 860^o C, we need to have an additional heat shield to reduce the heat transfer by radiation and to protect the pole piece of the SEM objective lens, detectors and other components present in the SEM chamber. The heat shield is hanged on the thermal bridge 1 as shown in figure 6.14. If we use the same estimation of heat reduction of 1/3 by using a heat shield, the temperature of the heat shield 2 is around 482^o C. Hence, we need another heat shield to further reduce the heat transfer. This heat shield will result in a temperature of 230^o C. The heat shield 3 is laser welded to two stainless steel rods, which are used to hang the heat shield on the thermal bridge 2. The CAD illustration of the heat shield 3 is shown in figure 6.15. The

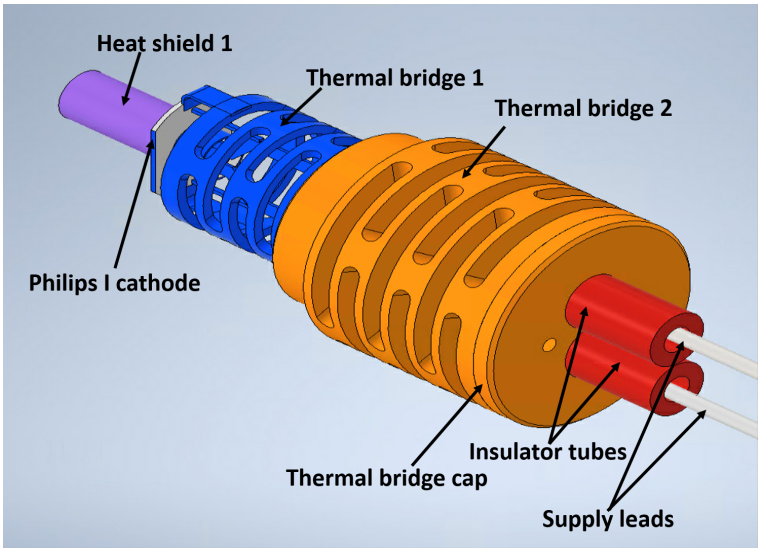

Figure 6.13: CAD illustration of the thermal bridge cap connecting the thermal bridge 1 and 2.

evaporator assembly is now placed in the device holder of the adaptor assembly as shown in figure 6.16. The thermal bridge 1, thermal bridge 2, thermal cap, heat shield 2, and 3 and the supply leads are all made of stainless steel (RVS 316L).

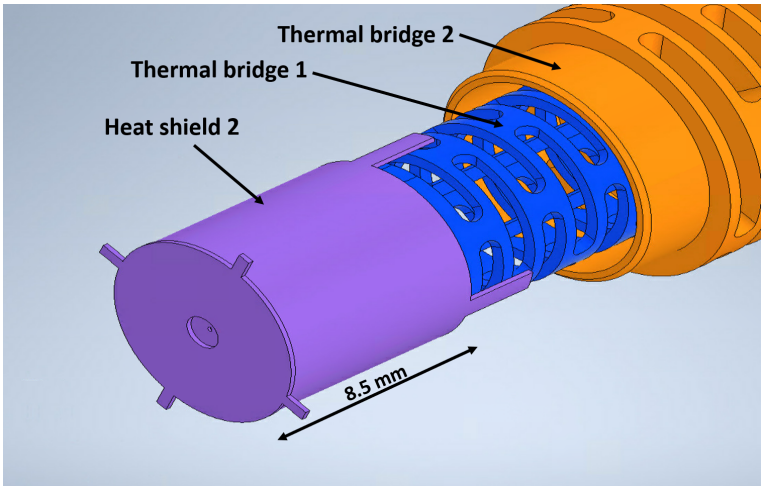

Figure 6.14: CAD illustration of the heat shield 2.

All components of the evaporator assembly were thoroughly cleaned before placing them in an SEM. The metallic components were first cleaned ultrason-

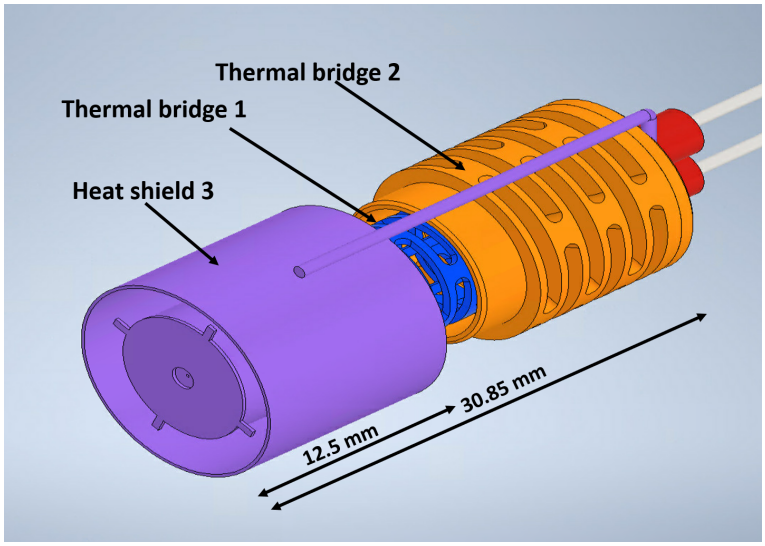

Figure 6.15: CAD illustration of the heat shield 3.

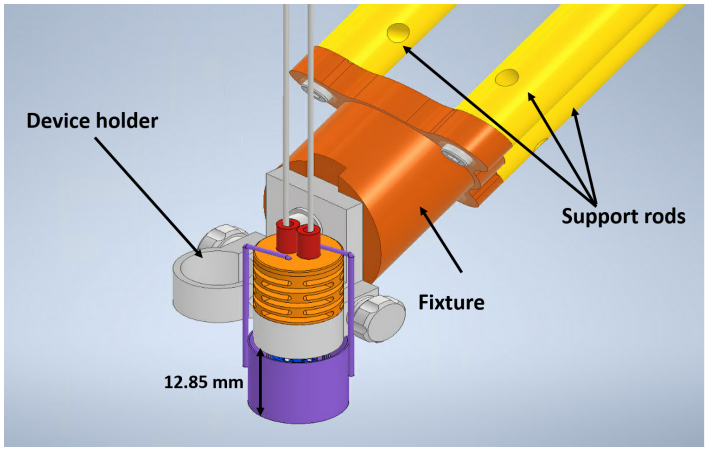

Figure 6.16: CAD illustration of the evaporator assembly mounted on the device holder which has been described in chapter 4.

ically in a beaker containing acetone for 2 hours. Then, they were cleaned in a beaker containing ethanol for 2 hours followed by blow-drying the components with nitrogen. The non-metallic components (the insulator tubes) were cleaned in a beaker containing ethanol for 2 hours followed by blow-drying with nitrogen. Before we install the molybdenum cap in the W pill box, we fill the cap with Au foils (0.5 mm thickness). The molybdenum cap filled with Au is gently placed over the W pill box with a steady hand, any unnecessary movement re-

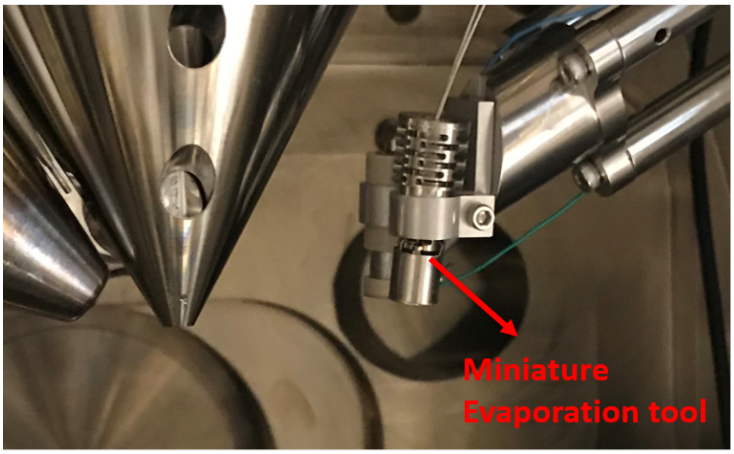

Figure 6.17: Photograph of the evaporator mounted in the device holder of the adaptor assembly in the SEM chamber.

sults in damage (the W pill box being disconnected from the steel holder) to the Philips I-cathode. The evaporator was assembled as shown in the CAD illustration shown in figure 6.16. The electrical connection was delivered by means of an electrical feedthrough. A Delta Elektronika ES030 – 5 was used to supply the power to the evaporator.

6.7. PRELIMINARY EXPERIMENTS AND SUGGESTIONS FOR IMPROVEMENT

The evaporator assembly was placed in the device holder of the adaptor assembly and mounted on to the SEM. The evaporator assembly in the SEM chamber is shown in figure 6.17. The initial test was to heat up the evaporator. Unfortunately, the test failed because of a disconnection of the Philips I-cathode's supply lead from the heating element. This was likely due to stresses applied during the entire mounting procedure and the lack of tensile relief structure in the supply leads. This could have been avoided if we had a stress relief structure as in the case of our substrate heater. Unfortunately, due to time constraints, we were not able to modify the existing evaporator assembly. One possible location to have the tensile relief would be at the support rod of the adaptor. We could attach an insulator that encloses one of the support rods (shown in figure 6.16), through which we could attach the supply leads through this structure resulting in stress release of the supply leads. Even though, we were not able to successfully demonstrate the working of an evaporator inside the SEM we have achieved

several requirements. With our evaporator, we have successfully made a miniature evaporation source that could be suspended inside the SEM. The evaporator deposition angle is normal to the substrate. Based on our choice of material and the design of several heat shields, we were able to minimize the impact of the evaporator on the electron beam and the surroundings. In future, when the evaporator is redesigned to have a tensile relief structure. Al, Cr, Ag and Sn which have a vapor pressure of 10^{-2} mbar could be evaporated in the operating regime of the Philips I-cathode [4]. The materials to be evaporated need to loaded into the molybdenum cap before mounting the evaporator in the SEM. The material has to be in thin foils or in wire form, or flakes (0.5 mm thickness), to make it easier for the material to be pushed into the molybdenum cap.

6.8. CONCLUSIONS

To summarize, in this chapter we listed the various requirements for implementing an in-situ thermal evaporator in the SEM. An initial prototype thermal evaporator was developed based on a Philips I-cathode source. With this evaporator we were able to deposit Au with a spot size of 1 mm in a separate test setup. We measured an evaporation rate of 2.9 Å/s when the substrate is kept at a distance of 1 mm. Also, the chamber pressure was kept at $1.3.10^{-6}$ mbar during the operation of the evaporator satisfying the pressure requirements. Also, it satisfies the requirement of the angle of incidence of the deposit material. And we observed no measurable outgassing during the operation of the evaporator. No additional pumps were required to keep the chamber pressure at 10^{-6} mbar. Based on the prototype, we designed and fabricated the evaporation assembly for use inside an SEM. Unfortunately, due to the lack of a tensile relief for the supply leads it resulted in the failure of operation of the evaporator. Hence, we couldn't demonstrate the operation and implementation of the evaporator in an SEM. A tensile relief structure should be added in a future design.

REFERENCES

[1] B. Titze and W. Denk, *Automated in-chamber specimen coating for serial block-face electron microscopy,* Journal of Microscopy **250** (2013).

[2] *e-flux evaporator,* (Accessed on 16-09-2021), https://tectra.de/deposition-progress/e-beam-evaporator/.

[3] C. B. Alcock, V. P. Itkin, and M. K. Horrigan, *Vapour Pressure Equations for the Metallic Elements: 298–2500K,* Canadian Metallurgical Quarterly **23**, 309 (1984), https://doi.org/10.1179/cmq.1984.23.3.309 .

[4] D. M. Mattox, *Chapter 6 - vacuum evaporation and vacuum deposition,* in *Handbook of Physical Vapor Deposition (PVD) Processing (Second Edition)*, edited by D. M. Mattox (William Andrew Publishing, Boston, 2010) second edition ed., pp. 195–235.

[5] V. van der Meijden, *Cleanroom in a scanning electron microscope*, Master thesis, Delft University of Technology (2014).

[6] N. D.S. Barratt and I.Bakker, *Cermet cathodes: A new technology for CRT applications,* Journal of SID **12**, 23 (2004).

[7] D. Barratt and G. Gaertner, *Recent developments in oxide cathode research for CRT applications,* Applied Surface Science **215**, 65 (2003), iVESC 2002.

[8] H. Frey, *Vacuum evaporation,* in *Handbook of Thin-Film Technology*, edited by H. Frey and H. R. Khan (Springer Berlin Heidelberg, Berlin, Heidelberg, 2015) pp. 13–71.

[9] *"DELTAELEKTR0NIKA ES150 SERIES",* (Accessed on 02-08-2022), https://www.delta-elektronika.nl/en/products/dc-power-supplies-150w-es150-series.html.

7

CONCLUSION

The goal of this thesis was to develop miniaturized microfabrication tools as an add-on to an existing SEM. By utilizing the add-ons, we could reduce the cost and time for rapid prototyping of proof of concept devices in a single tool.

Initially we selected a few techniques that could be miniaturized as add-on's to the SEM. A miniature sputter tool, a miniature thermal evaporator tool and a in-situ substrate heater were chosen as the add-on tools inside the SEM. The add-on tools were chosen based on the criteria that it shouldn't affect the normal working of the SEM.

We demonstrated two substrate heaters, V1 (designed for 150 ^{o}C) and V2 (capable of heating up to 300 ^{o}C). Heater V1 was designed and developed to meet the requirements for partial cleaning of the substrate, removal of adsorbed water and purification of FEBID structures. It was designed to keep thermal drift at a minimum while temperature ramp-up. We utilized the venting of the SEM chamber as a mechanism for cooling the substrate back to room temperature. Heater V2 was designed and developed to carry out an in-situ thermal ALD process. We gave up the requirement of thermal drift as our goal here was to reach higher temperatures (around 300 ^{o}C) for ALD processes. We were able to successfully heat the substrate up to 300 ^{o}C and keep the SEM stage at room temperature. In future, both heaters V1 and V2 can be used as substrate heaters for the development of novel FEBID precursors.

Next, we successfully demonstrated an in-situ thermal atomic layer deposition (ALD) process by carefully selecting the precursor and co-reactant timing from literature and pump-down experiments. However, a single cycle of the ALD process required a long time, approximately 3 minutes. We identified the root cause of the long precursor dosing and precursor purge time as the design of the

existing GIS needle assembly. We solved this issue, by the design, fabrication, and development of a novel GIS needle assembly that could be easily attached to the existing GIS assembly. By utilizing the new GIS needle assembly, we successfully reduced the precursor dosing and precursor purge times. Further by using the heater V2, we successfully carried out an in-situ thermal ALD process inside the SEM and reduce the cycle time to less than a minute. By incorporating computer controlled valves, the cycle time could be further reduced, potentially reaching cycle times as observed in a standard ALD tool. In future, the existing GIS needle assembly can be replaced by our new GIS needle assembly for improved FEBID processing in the SEM.

A miniature plasma source operating as a sputtering tool was successfully demonstrated inside the SEM. To mount the novel miniature plasma source in the SEM, we designed and fabricated a housing assembly that was able to accommodate both the plasma source and thermal evaporator. We were successfully able to sputter a similar thin film of Au (20 nm) inside the SEM utilizing the miniature plasma source. Looking ahead, the gas source could be replaced with dry air, resulting in the use of an oxygen plasma for substrate cleaning and enhancing the purity of FEBID deposits. Next, we mounted an in-situ thermal evaporator on to the mounting assembly. Unfortunately, during the initial test of the thermal evaporator the supply leads to the Philips I-cathode became disconnected as a result of the stress applied during the mounting of the evaporator. Due to time constraints, further improvements were not possible on the thermal evaporator. This highlights an important consideration while designing moving components inside the SEM, that is to provide stress relief structures.

In conclusion, in this work we have developed prototype add-on tools for the SEM, but due to time constraints the prototypes were not extensively tested or characterized, nor were they used in combination to fabricate an actual in-situ device. Moving forward, the next step would be to utilize the different miniaturized tools together in fabricating a device completely inside the SEM. As illustrated in figure 2.10, we can begin with a clean substrate and deposit a thin layer of Au utilizing the thermal evaporator, once it is fixed with stress relief structures. Then, we can direct-write bow-tie antennas using the FEBID process (for instance using carbon). This FEBID structure acts as a hard mask. Finally, we can use the miniature sputter tool to transfer the pattern from the FEBID hard mask into the underlying Au film. Any leftover material from the FEBID mask, can be removed by using FEBIE.

Further in future, with the fabrication and characterization of an actual in-situ device, the concept of *Cleanroom in an SEM* can perhaps be commercialized. We believe that the integration of the substrate heater, in-situ thermal ALD, sputtering tool, and evaporator inside the SEM will enable the faster realization

of proof-of-concept devices with significant reductions in time and cost. Such a versatile tool will serve researchers in academia and research institutes in rapidly fabricating prototype devices in a single tool, eliminating the need for a cleanroom. The *Cleanroom in an SEM* tool will be invaluable for universities and research institutes to carry out research.

ACKNOWLEDGEMENTS

First and foremost, I would like to express my heartfelt gratitude to my promoters, Kees and Pieter, for their unwavering support, invaluable knowledge, and insightful guidance. I am truly grateful for their mentorship and for welcoming me into the Charged Particle Optics (CPO) group. Jacob, I extend my heartfelt thanks to you for making me feel at home in the group and for your warm welcome.

I will forever cherish the memorable weekly meetings with Kees, where we delved into a wide range of topics and his contagious enthusiasm for various subjects. I am especially grateful for his ingenious suggestion of snake security to safeguard my backpack after it was stolen on my train journey back from India. Additionally, I would like to thank him for his last-minute review of my conference abstracts. It was an absolute pleasure to show Kees my hometown of Chennai during the scorching summer heat, and I will never forget his adventurous idea of jogging at noon on the beach when the temperature soared to 35°C.

I would like to express my sincere gratitude to the backbone of the group, the technicians, without whom this thesis, and any other project, would not have been possible. I extend my heartfelt thanks to Jan de Loff for his invaluable assistance in setting up the vacuum setup during my initial months. Han, your expertise in all things electronics, computer setup, and remote logins, especially during the challenging times of the COVID-19 pandemic, has been truly invaluable. Carel, thank you for your support in the fabrication process and for sharing your amusing coffee corner stories about the Soviet Union and East Germany. A tremendous thanks to Ruud for his assistance in mechanical design, ANSYS simulations, and for the engaging conversations we shared over coffee. I would also like to thank Youp for his contributions to the mechanical design and simulations. Dustin, without your invaluable help in resolving issues with the microscope, this thesis would not have come to fruition. Many thanks to Martin for your invaluable assistance in the fabrication process. Johan, your expertise in all things vacuum-related, particularly in troubleshooting leak issues in the vacuum setup, has been truly indispensable. Many thanks to the workshop team in DEMO and at reactor institute for their help in machining the different components for the project.

I would also like to express my gratitude to the super seniors: Sangeetha, Marijke, Shammi, Gerward, Robert, Jayson, Yan, Leon, and Thomas, for embracing me as part of the group. A big thanks to Sangeetha and Naren for the de-

lightful Indian dinners at their place. To my fellow nerd and force buddy, Marijke, thank you for taking the time to show me around Moderna and Bologna. Shammi, I am truly grateful for your invaluable assistance in helping me settle down in Delft, from your expert advice on securing a quick appointment with a GP to sharing your amazing cooking recipes. Gerward, thank you for our thought-provoking discussions and for the enjoyable drinks at Tee Pee Kafee. Robert, your passion for photography, unwavering support, and engaging discussions have meant a great deal to me. Anjella a big thanks to you for helping me in moving to Delft. Aditi, Wilco, Dusan, Kerim, and Maurice, we embarked on this journey together, and your companionship has made it a truly memorable experience. Aditi, a special thanks to you for our delightful chit-chats, enjoyable dinners, and engaging discussions that spanned topics from TV soaps and movies to politics in India and the realm of science. A big thanks to Vidya, Nicolo, Wouter, Conny, Anne-Marie, Mathijs, Yoram, Aya, Luc, Lixin, Ryan, Xin, Laura, Marco, Huma, Diederik, Leoni, Dan, Elizabeth and Yuri. I would also like to thank Kavitha, Gokul and Durga for their support and food over the years. A huge thanks to my family (appa and amma) for their support. Aurelie, Sandeep and Sreetama,a big thanks to you guys for pushing me in Leuven to finish the thesis. Finally, a big thanks to you Pappu in feeding and supporting me while I spent Sundays writing the thesis.

To each and every individual who has played a role, big or small, in my journey, I express my deepest gratitude. Your support, guidance, and camaraderie have made this experience unforgettable, and I am truly honoured to have had the opportunity to work alongside such remarkable individuals.

CURRICULUM VITÆ

09-02-1988	Born in Chinglepet, India.

EDUCATION

2005 - 2009	B.E. in Electrical and Electronics Engineering Anna University, India
2011 - 2014	M.Sc. (Honors) Advanced Optical Technologies FAU Erlangen-Nurnberg, Germany
2015 - 2020	PhD. Applied Physics Delft University of Technology, Delft

WORK EXPERIENCE

2009 - 2011	Research assistant Indian Institute of Technology, Bombay
2020 - 2021	Electron beam lithography engineer Microsoft Quantum Lab, Delft
2021 - Present	R & D Engineer imec, Leuven

List of Publications

1. **G. Jeevanandam** V.van der Meijden, L.D.Birnie, P.Kruit, C.W.Hagen, *'Cleanroom' in SEM*, Microelectronic Engineering **18**, 224 (2020).